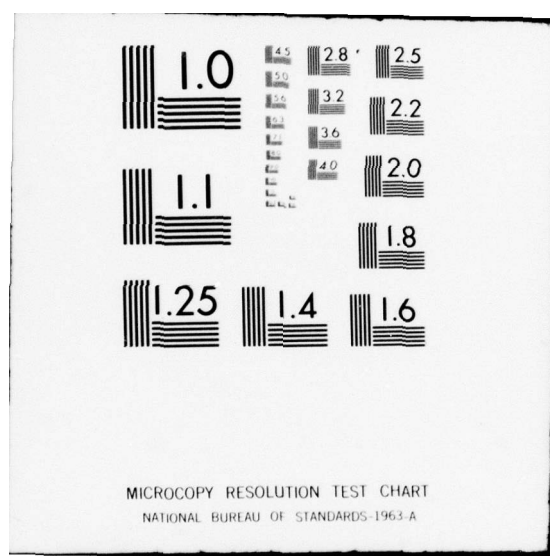


AD-A067 319 HUGHES AIRCRAFT CO TORRANCE CALIF ELECTRON DYNAMICS DIV F/G 9/1  
PERMANENT MAGNET STUDY FOR HIGH AVERAGE POWER TWTS. (U)  
FEB 79 W A HARMAN, R S HOLLISTER, J O TILLERY F30602-77-C-0109  
UNCLASSIFIED EDD-W-07407-F RADC-TR-78-288 NL

1 OF 2  
AD  
AD 67319





*E*

**LEVEL** *(12)*

RADC-TR-78-288  
Final Technical Report  
February 1979



## **PERMANENT MAGNET STUDY FOR HIGH AVERAGE POWER TWTs**

**Hughes Aircraft Company**

W. A. Harman  
R. S. Hollister  
J. O. Tillery



**AD A0 67319**

**APPROVED FOR PUBLIC RELEASE; DISTRIBUTION UNLIMITED**

**ROME AIR DEVELOPMENT CENTER  
Air Force Systems Command  
Griffiss Air Force Base, New York 13441**

**79 04 09 008**

This report has been reviewed by the RADC Information Office (OI) and is releasable to the National Technical Information Service (NTIS). At NTIS it will be releasable to the general public, including foreign nations.

RADC-TR-78-288 has been reviewed and is approved for publication.

APPROVED:

*Kenneth Merrithew*

KENNETH MERRITHEW  
Project Engineer

APPROVED:

*Joseph L. Ryerson*

JOSEPH L. RYERSON  
Technical Director  
Surveillance Division

FOR THE COMMANDER:

*John P. Huss*

JOHN P. HUSS  
Acting Chief, Plans Office

If your address has changed or if you wish to be removed from the RADC mailing list, or if the addressee is no longer employed by your organization, please notify RADC (OCTP) Griffiss AFB NY 13441. This will assist us in maintaining a current mailing list.

Do not return this copy. Retain or destroy.

UNCLASSIFIED

SECURITY CLASSIFICATION OF THIS PAGE (When Data Entered)

**DD FORM 1 JAN 73 1473 EDITION OF 1 NOV 65 IS OBSOLETE**

UNCLASSIFIED

SECURITY CLASSIFICATION OF THIS PAGE (When Data Entered)

UNCLASSIFIED

SECURITY CLASSIFICATION OF THIS PAGE(When Data Entered)

Item 20 (Cont'd)

to find ways for increasing the average power handling capability of tubes with permanent magnet configurations. In instances where lower perveance beams continue to interact at acceptable RF levels, substantial improvements in beam defocusing are indicated, but at the penalty of higher operating voltages for similar power levels. A detailed thermal analysis of a typical high power traveling wave tube (TWT) indicates areas where additional thermal capability might be achieved. A system life cycle analysis on a solenoid focused tube indicates a small percentage of failures due to focusing problems, however, failure rates associated with the tube alone would be higher. A design is presented for a high average power S-Band TWT using concepts developed during the study.



UNCLASSIFIED

SECURITY CLASSIFICATION OF THIS PAGE(When Data Entered)

TABLE OF CONTENTS

<u>Section</u>		<u>Page</u>
1.0	INTRODUCTION AND SUMMARY	1
2.0	APPROACH	3
3.0	TECHNICAL DISCUSSION	5
3.1	General Beam Focusing Discussion	5
3.2	Analysis of Confined PPM Beams	9
3.3	Focusing Studies for Increased Beam Stiffness	18
3.4	Tube and Focusing Parameter Relationships	35
3.5	RF Defocusing with Drive	48
3.6	Perveance as a Design Parameter	64
3.7	Traveling Wave Tube Thermal Model	67
3.7.1	Introduction	67
3.7.2	Modeling Technique	67
3.7.3	Computer Programs	75
3.7.4	Fluid Flow Cooling	81
3.7.5	Analytical Results	83
3.7.6	Conclusions	84
3.8	Tube Design for High Average Power	107
3.9	Hybrid Focusing Structures	118
3.10	System Life Cycle Analysis	120
4.0	CONCLUSIONS	129
 <u>Appendices</u>		
A	LAMINAR BEAM MODEL INCLUDING AXIAL FORCES	131
B	BASELINE EXAMPLES OF HIGH POWER TUBE DESIGNS	137
C	FORCED CONVECTIVE HEAT TRANSFER COEFFICIENTS FOR POLE PIECE COOLANT CHANNELS	151
D	INITIAL TEMPERATURE ESTIMATES AND MATERIALS DATA	163
REFERENCES		169

LIST OF ILLUSTRATIONS

<u>Figure</u>		<u>Page</u>
1	PPM focusing parameter relationships along with theoretical beam ripple for $\gamma = 0$ .	11
2	Theoretical beam ripple amplitude as a function of PPM focusing parameters for $\gamma = 0$ .	12
3	Plot of expression related to axial velocity variation for the case $B/B_{Br} = \sqrt{2}$ .	15
4	Single period focusing with $B/B_{Br} = 1.0$ .	20
5	Single period focusing with $B/B_{BR} = 1.25$ .	21
6	Double period focusing with $B/B_{BR} = 1.0$ .	22
7	Beam scalloping for injection of beam at other than equilibrium balance condition.	24
8	$B_{rms}$ on axis as a function of magnetic parameters.	26
9	$B_{rms}$ on axis as a function of magnetic parameters.	27
10	Example of hi-perveance confined beam flow employing short period magnetic fields.	29
11	Edge electron calculations for confined PPM beam flow, $L = 1.5$ .	31
12	Edge electron calculations for confined PPM beam flow, $L = 2.0$ .	32
13	Normalized phase displacement from average phase due to $\dot{z}/u_0$ variation shown in Figure 11.	33
14	Calculated cavity diameters for various design voltages and $g/l_c$ ratios.	41
15	PPM design parameter curve.	43
16	$B_{rms}$ vs L/D for $H_m = 6000$ .	44
17	$B_{rms}$ vs L/D for $H_m = 5500$ .	45
18	Sampling of calculated beam trajectories through last 12 R-F circuit gaps in 559H TWT at saturation.	50

LIST OF ILLUSTRATIONS (CONTINUED)

<u>Figure</u>		<u>Page</u>
19	Sampling of calculated beam trajectories through last 12 R-F circuit gaps in 559H TWT at saturation.	51
20	Sampling of calculated beam trajectories through last 12 R-F circuit gaps in 559H TWT at saturation.	52
21	Sampling of calculated beam trajectories through last 12 R-F circuit gaps in 559H TWT at saturation.	53
22	Sampling of calculated beam trajectories through last 12 R-F circuit gaps in 559H TWT at saturation.	54
23	Sampling of calculated beam trajectories through last 12 R-F circuit gaps in 559H TWT for saturation level R-F gap voltages.	57
24	Sampling of calculated beam trajectories through last 12 R-F circuit gaps in 559H TWT for saturation level R-F gap voltages.	58
25	Sampling of calculated beam trajectories through last 12 R-F circuit gaps in 559H TWT for saturation level R-F gap voltages.	59
26	Sampling of calculated beam trajectories through last 12 R-F circuit gaps in 559H TWT for saturation level R-F gap voltages.	60
27	Radial and axial gap fields in the 559H coupled cavity circuit at $b/a = 0.5$ .	62
28	Traveling wave tube thermal model block schematic.	68
29	Typical sectioning of pole pieces for thermal model.	69
30	Typical nodal designation for pole pieces (node numbers shown in each block section).	70
31	Typical nodal designation for pole pieces (node numbers shown in each block section).	71
32	Typical nodal designation for pole pieces (nodal numbers shown in each block section).	72
33	Typical nodal designation for pole pieces (node numbers shown in each block section).	73

LIST OF ILLUSTRATIONS (CONTINUED)

<u>Figure</u>		<u>Page</u>
34	Typical nodal designation for pole pieces (node numbers shown in each block section).	74
35	CINDA execution block diagram.	82
36	Thermal data spacer 1 (temperatures in degrees celsius).	85
37	Thermal data pole piece 1 (temperatures in degrees celsius).	86
38	Thermal data spacer 2 (temperatures in degrees celsius).	87
39	Thermal data pole piece 2 (temperatures in degrees celsius).	88
40	Thermal data spacer 3 (temperatures in degrees celsius).	89
41	Thermal data pole piece 3 (temperatures in degrees celsius).	90
42	Thermal data spacer 4 (temperatures in degrees celsius).	91
43	Thermal data pole piece 4 (temperatures in degrees celsius).	92
44	Thermal data spacer 5 (temperatures in degrees celsius).	93
45	Thermal data pole piece 5 (temperatures in degrees celsius).	94
46	Thermal data spacer 6 (temperatures in degrees celsius).	95
47	Thermal data pole piece 6 (temperatures in degrees celsius).	96
48	Thermal data spacer 7 (temperatures in degrees celsius).	97
49	Thermal data pole piece 7 (temperatures in degrees celsius).	98
50	Thermal data spacer 8 (temperatures in degrees celsius).	99
51	Thermal data pole piece 8 (temperatures in degrees celsius).	100

LIST OF ILLUSTRATIONS (CONTINUED)

<u>Figure</u>		<u>Page</u>
52	Thermal data spacer 9 (temperatures in degrees celsius).	101
53	Thermal profiles pole piece 9 (temperatures in degrees celsius).	102
54	Pole piece 1 ferrule isotherms for 4 GPM flowrate (temperatures in degrees celsius).	103
55	Thermal data pole piece 1, 8 GPM coolant flow (temperatures in degrees celsius).	104
56	Power absorbed into fluid nodes -- 559H model power dissipation vs length.	105
57	Phase characteristic of the 559H coupled cavity TWT circuit.	110
58	Calculated PPM magnetic field shapes for two different magnetic gaps.	113
59	Calculated beam ripple and axial velocity variation for the assumed focusing design.	114
60	Calculated small signal gain of design tube.	116
61	Calculated large signal performance of design tube.	117
62	Profile of funding for life cycle cost analysis.	123
63	Hughes' life cycle cost model relationships.	124
64	559H traveling wave tube.	138
65	Gain and power output of 559H, Serial No. 6 at a cathode voltage of -43 kV and beam current of 17 amperes.	140
66	584H traveling wave tube.	142
67	Saturated power output of the 584H TWT.	143
68	8716H traveling wave tube.	145
69	Output power of the 8716H for 100 mW constant drive.	146

LIST OF ILLUSTRATIONS (CONTINUED)

<u>Figure</u>		<u>Page</u>
70	635H solenoid focused traveling wave tube.	148
71	Typical output power characteristic of the 635H.	149
72	Effect of noncircular flow cross section on heat transfer.	157
73	Effect of tube curvature on the peripheral variation of the heat transfer factor.	159
74	Effect of entrance region on heat transfer.	160
75	Relative effect of roughness on skin friction and heat transfer.	162
76	Thermal conductivity vs temperature.	164
77	Initial temperature estimates for determining thermal conductances between nodes.	165
78	Initial temperature estimates for determining thermal conductance between nodes.	166
79	Initial temperature estimates for determining thermal conductance between nodes.	167
80	Initial temperature estimates for determining thermal conductances between nodes.	168

## EVALUATION

The high power transmitters used in radars currently employ linear beam microwave amplifiers that require external electromagnetics that are costly, inefficient, heavy and add to system complexity. Rare earth magnets such as Samarium Cobalt (S<sub>5</sub> CO<sub>17</sub>) when used in high power linear beam amplifiers can reduce cost, decrease power consumption by several kilowatts and decrease weight by about 200 pounds.

This effort is included in the Thermionics area of Surveillance ECCM, RADC TP04B. These reductions in power consumption and weight will make a significant impact in tactical radar systems where mobility is a high priority. The results derived herein will serve as a basis for improving linear beam high power microwave tubes used in Air Force radars.

*Kenneth Merrithew*

KENNETH MERRITHEW  
Proj Engr/OCTP

## 1.0 INTRODUCTION AND SUMMARY

This report covers work accomplished on a study program sponsored by Rome Air Development Center to advance the state of microwave tubes by investigating the use of permanent magnets for providing electron beam focusing in high power linear beam tubes. The long range objective of this effort is to reduce the size, weight, cost, and system complexity and to increase the overall efficiency of linear beam microwave tubes operating above 100 kilowatts peak power. The study was directed mainly towards the elimination of heavy electromagnets and their accompanying power supplies in tubes operating between 100 kilowatts and 1.0 megawatt of peak power in the frequency range of 3 and 10 GHz. While the results obtained here apply specifically to coupled cavity structures, many of the concepts developed are of a more general nature.

During the course of the investigation the characteristics of several state-of-the-art tubes in the frequency and power range of interest were studied. A system life cycle analysis was conducted from failure analyses reports on a typical solenoid focused production tube to determine the possible impact of replacing electromagnetic focusing with permanent magnet focusing. A detailed thermal analysis of a typical high average power coupled cavity circuit was made to determine limiting factors with respect to obtaining high average power operation with present tube designs. A complete review of the problem of electron beam focusing in high power tubes by means of periodic permanent magnet focusing was conducted to determine how beam focusing under large signal conditions could best be improved. Design parameters were determined for a high average power S-band 150-170 kilowatt tube applying information learned as a result of the study.

## 2.0 APPROACH

Linear beam tubes can be built to operate at very high RF peak powers by going to high beam voltage and high beam powers. The average power of such a device is generally limited by various thermal considerations, not the least of which is beam interception by the RF interaction circuit under high level operation. In a solenoid focused tube the beam can be controlled to a high degree provided the magnetic focusing field is kept substantially above the Brillouin<sup>1</sup> value. At high magnetic fields the electrons can be confined to essentially following flux lines such that they are effectively prevented from impacting the circuit under all conditions of operation.

Direct replacement of a solenoid focusing field with a straight permanent magnet field is sometimes possible, but will usually result in undesirably large and heavy magnet structures. However, weight and size can be dramatically reduced when magnet structures are used that employ periodic reversals of field, primarily because of the large reduction in the resultant leakage fields. Since the principal focusing force in a magnetic focusing system depends upon  $B^2$  the direction of  $B$  is immaterial. Thus, beam focusing is achieved independent of field reversal regions and the rms value of the  $B$ -field becomes the effective focusing field. However, this is only true if there is no substantial loss of axial electron velocity due to rotational energies, and if the period of the focusing force is not such that it excites instabilities in the beam. These restrictions will be discussed further in later sections.

The quality of focusing achieved with solenoid focused tubes operating above the Brillouin field allows high average powers to be attained in addition to high peak powers. The principle limitation in either solenoid or periodic permanent magnet (PPM) focused tubes at Brillouin levels of field is that of thermal dissipation of beam power intercepted

by the circuit as the result of high level RF defocusing of the beam. Due to the numerous problems associated with confining PPM beams, nearly all PPM focused tubes are designed to operate under Brillouin focusing conditions.

The alternatives for increasing the average power capability in PPM focused tubes is, therefore, to either improve the thermal dissipation capability of the circuit or to reduce the beam interception under drive. Since the source of the problem really lies in the focusing, the approach during this study was to concentrate on ways to improve the focusing characteristics of the beam. Detailed thermal analyses were also conducted on typical high average power circuits to determine their thermal capabilities and to pinpoint areas of weakness in the circuit thermal design.

In an attempt to achieve performance approaching that of solenoid tubes the possibility of confining a PPM beam with focusing fields greater than the Brillouin field (through the introduction of magnetic flux linkages at the cathode) was investigated. Due to the nature of magnetic field reversals in confined electron flow (principally the problem of rotational energies) the degree of confinement achievable in PPM focused beams is severely limited by the beam perveance. However, the demonstrated effectiveness of confinement upon beam defocusing offers the real possibility of dramatically increasing the average power capability in PPM focused tubes by reducing the intercepted beam power under saturated drive levels.

A number of existing Hughes' high power tubes were used as baseline state-of-the-art examples of 100 kW and higher designs. Specific data on these tubes is presented in Appendix B. All of these tubes (559H, 584H, 8716H, 635H) have microperveances greater than 1.5. They offered a general range of design parameters around which the various focusing studies and thermal analyses were performed.

### 3.0 TECHNICAL DISCUSSION

The greatest impact from the use of permanent magnet focusing is to eliminate the need for a solenoid power supply. Periodic permanent magnets can also have considerable impact upon size and weight, especially with high energy product materials such as the rare earth magnet materials.

The usefulness of permanent magnets to replace electromagnet focusing in high power linear beam tubes is dependent upon achieving comparable tube performance. Since the present primary factor limiting the average power capability of PPM focused high power TWT's is beam interception by the circuit, a large portion of the effort during this study was directed toward reducing the RF defocusing of the beam under large signal drive conditions. This can only be accomplished with an understanding of the physical principles of beam focusing. Therefore, it would seem to be in order to review briefly some of the fundamental concepts of magnetic field focusing as they relate to the present investigation.

#### 3.1 GENERAL BEAM FOCUSING DISCUSSION

Using a non-thermal laminar flow model, focusing can be analyzed in terms of a radial force balance between outward space charge defocusing forces in the beam and net inward or focusing forces provided by some particular focusing mechanism. In axially symmetric magnetic focusing systems a focusing force (Lorentz force) occurs when an electron possesses an angular component of velocity in the presence of an axially directed B-field. Angular velocities result whenever the flux linkages of the electrons differ from their initial linkages at the time they leave the cathode surface. Any change in flux linkage imparts angular

momentum to the electron in accordance with Busch's Theorem (see Appendix A). Net inward focusing forces only result when flux linkages exceed the initial values at the cathode.

To first order, a force balance is maintained equally well with a time averaged focusing force as with a constant value of the balancing force, provided the force averaging takes place over periods small compared with the natural oscillating or scalloping period of the beam. This may be accomplished by providing an rms value of field equal to the required focusing field and by keeping all periodicities associated with force averaged regions small compared to the normal beam scallop wavelength.

In addition to a force balance it is important to have some degree of "stiffness" in the beam (i.e., resistance to perturbations from the normal balanced condition) in order that RF defocusing will be minimized in the presence of high levels of beam modulation. In an analogous manner to mechanical structures, the stiffness of an electron beam is directly related to its natural oscillation frequency, that is, the frequency with which the disturbed beam oscillates about its equilibrium or force balance radius. A natural normalization of this frequency is with respect to the plasma frequency of the beam. A Brillouin focused solid beam has a scalloping frequency equal to the plasma frequency of the beam (calculated on the basis of its equilibrium diameter) whereas a confined beam scallops at a frequency approaching the magnetic cyclotron frequency, depending upon the degree of actual confinement. The relationship can be expressed by

$$\left(\frac{\omega_{sc}}{\omega_p}\right)^2 = \left(\frac{\omega_c}{\omega_p}\right)^2 - 1 \quad (1)$$

which may also be written as

$$\left(\frac{\omega_{sc}}{\omega_p}\right)^2 = 2 \left(\frac{B_{rms}}{B_{Br}}\right)^2 - 1 \quad (2)$$

where  $\omega_{sc}$ ,  $\omega_p$ , and  $\omega_c$  are respectively the scalloping, plasma, and cyclotron frequencies and where  $B_{rms}$  and  $B_{Br}$  represent the actual and the Brillouin values of magnetic field for a balanced or focused beam flow. Since the Brillouin condition represents the least value of B-field possible for focusing a beam it also presents the least resistance to focusing perturbations by having the lowest natural oscillation frequency.

To a first order accuracy the average net force available for the inward focusing of an electron is proportional to  $(\psi_{rms}^2 - \psi_c^2)$ , that is, the difference between the squares of the rms focusing flux linkages and the initial flux linkages upon leaving the cathode. Consequently, achieving balanced flow with a higher than Brillouin degree of beam stiffness (i.e., value of  $B_{rms}/B_{Br}$  greater than unity) requires that a prescribed amount of initial cathode flux linkage be provided. Most high power solenoid focused linear beam tubes utilize cathode flux to provide a greater degree of confinement than is achieved with Brillouin focusing alone for maintaining beam control under high level RF conditions.

In cases where a uniform magnetic focusing field is replaced by an equivalent rms value of focusing field a number of potential problems arise. To the extent that the beam does not slow down appreciably as the result of any additional rotational energy that might be acquired as the result of the form of the rms field, and to the extent that the same average of the square of the field is maintained over lengths

short compared to the natural beam scalloping wavelength, a stable focused flow will result that has essentially the same characteristics as the original uniform focusing field case. However, if the period length over which the force averaging takes place approaches the natural scalloping wavelength of the beam the focusing will generally become unstable with distance. Actually, a beam ripple amplitude associated with the focusing period increases without bound as the focusing period approaches the unstable condition. In general, the quality of a PPM focused flow only approaches that of the uniform field case when the focusing period is kept small. Unfortunately, the shorter one makes the period of a magnetic focusing structure, the more difficult it becomes to generate peak or rms field on the axis of the structure. In addition, the stiffer the beam, the shorter the scalloping wavelength and, therefore, the shorter the focusing period that must be used to properly focus the beam.

An additional problem arises whenever field reversals are employed, as with normal PPM focusing structures. Under these conditions appreciable cathode flux for purposes of beam stiffness can cause excessive amounts of rotation of the beam in those regions where the flux linkages are opposite in sign from the original cathode linkages. This rotational energy results from the large total change in flux linkages that takes place in the reversed field regions. From simple energy considerations it is clear that this rotational energy is always at the expense of longitudinal velocity in the beam. The problem compounds itself by virtue of the fact that the slowing down of the beam not only creates a greater space charge density in the beam (higher effective perveance) but causes the effective focusing period (actually, only the half-periods containing the field reversals) to appear longer in terms of the scallop period of the beam. As a result, increasing the degree of confinement in focusing schemes employing magnetic field reversals severely limits the magnitude of the beam perveance that can be effectively focused. High degrees of confinement are generally limited to

microperveances of a few tenths or less, whereas some degree of confinement can be achieved with microperveances of unity and above.

### 3.2 ANALYSIS OF CONFINED PPM BEAMS

Since nearly all standard published treatments of PPM focusing omit the effects of axial forces by assuming a constant axial beam velocity, they could not be used to determine the extent of this effect as it applies to the confining of PPM focused beams. The present study made use of a Hughes' digital computer program in which axial forces are taken into account. The program is based on a simple paraxial laminar flow model and as such only calculates the outer envelope of the beam. The mathematical analysis upon which this program is based is presented in Appendix A. In this simplified model it is assumed that the entire beam slows down by the amount of the outermost electrons. This simplifying assumption is justified on the basis that very little of the total space charge is represented by portions of the beam near the axis where rotational energies remain small. The assumption would be valid for thin hollow beams, and tends to calculate a worst case or upper bound performance for the case of solid beams.

A set of normalized parameters characterizes various PPM focusing cases. They are  $\alpha$ ,  $\beta$ ,  $\gamma$ , and  $K$  (defined in Appendix A).  $\alpha$  characterizes the magnetic lens strength. Consequently, it plays a dominant role in determining the amplitude of the beam ripple that results from having a set of periodically spaced lenses. It is also the factor generally associated with any focusing instabilities.  $\beta$  is a measure of the space charge in the beam that is being contained by the magnetic lens system.  $K$  measures the degree of beam confinement in terms of the ratio of the initial cathode flux linkages to the rms value of flux linked by the focused beam.  $\gamma$  is the additional parameter introduced that measures the relative magnitude of the axial force terms and is essentially a normalized beam diameter. A zero diameter beam experiences no axial velocity changes from either rotational energy

changes or from axial potential changes associated with space charge depression of potential. For  $\gamma = 0$  the analysis reduces to most standard published treatments.

The Brillouin condition which balances radial forces within the beam is

$$\omega_L^2 = \frac{\omega_p^2}{2} \quad (3)$$

For periodic focusing, using the notation of this report (see Appendix A),  $\omega_L$  becomes an rms Larmor frequency and Equation (3) is the condition for an average force balance. In terms of the normalized parameters, this is equivalent to setting  $\alpha$  equal to  $\beta$ . Likewise, if there is flux threading the cathode, the force balance relationship becomes

$$\alpha = \beta/(1 - K) \quad (4)$$

with

$$\frac{B}{B_{Br}} = \sqrt{\alpha/\beta} = \frac{1}{\sqrt{(1 - K)}} \quad (5)$$

The beam ripple resulting from the periodic lens system is primarily a function of  $\alpha$  and does not directly depend upon the beam parameters. Figures 1 and 2 show the relationships between  $\alpha$ ,  $\beta$ ,  $K$ , and the beam ripple generated by the periodic lens system. These curves are for  $\gamma = 0$  and for pure sinusoidal focusing fields. They are equivalent to Harker's<sup>2</sup> data except for being normalized with respect to the average beam radius rather than the peak radius. Renormalizing to the final average radius also makes the curves slightly different from Equation (4) where the implied normalization is with respect to an equivalent solenoid focused Brillouin beam. However, for finite values of

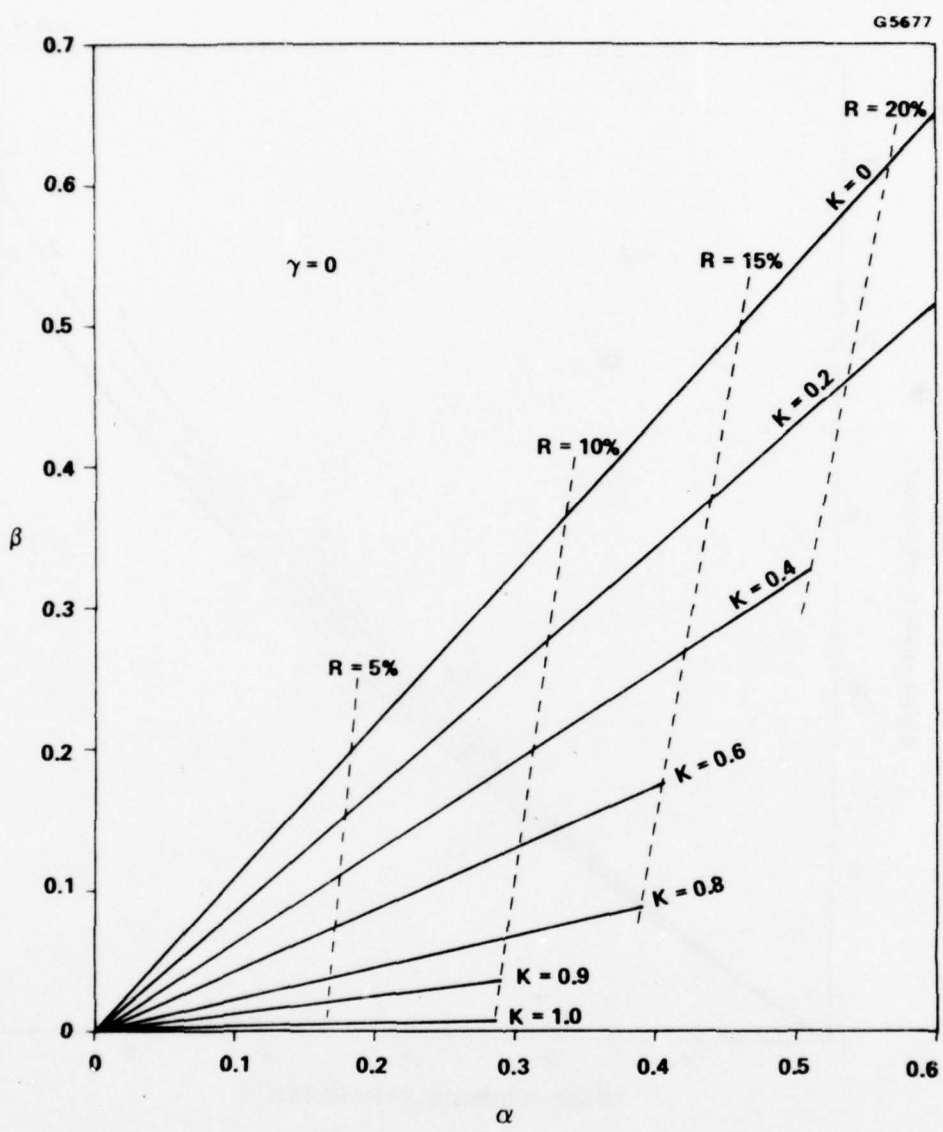


Figure 1 PPM focusing parameter relationships along with theoretical beam ripple for  $\gamma = 0$ .

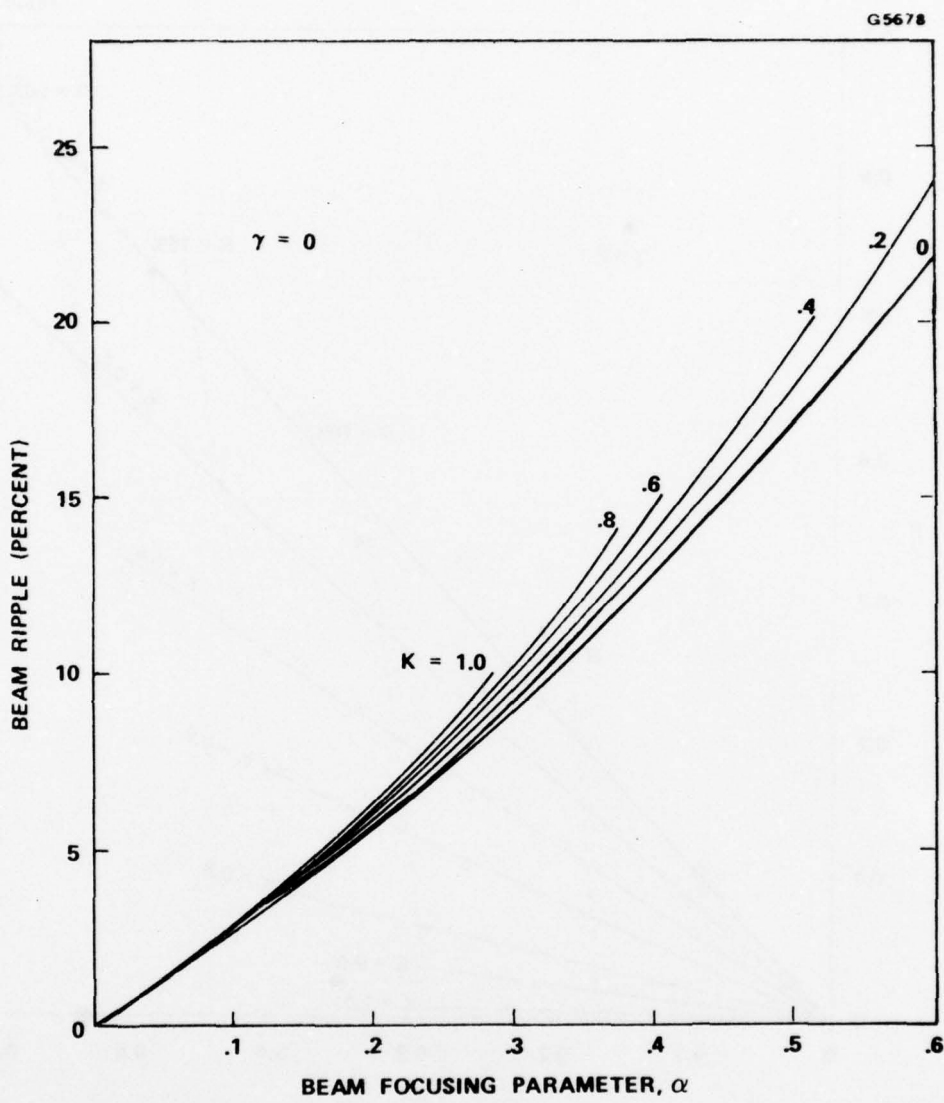


Figure 2 Theoretical beam ripple amplitude as a function of PPM focusing parameters for  $\gamma = 0$ .

$\gamma$  and for non-sinusoidal fields the average velocity and radius of the beam are not readily definable, and then a normalization based on a uniform field equivalent Brillouin beam becomes advantageous for avoiding ambiguities. Even this does not completely remove the problem for finite values of  $\gamma$  since the integration of the beam equations requires an initial velocity condition which ultimately determines the level of the velocities in the calculation. Calculations presented in this report have generally been started with  $\dot{z}/u_0 = 1.0$  which does not necessarily reference the beam to an equivalent uniform Brillouin case. One could easily develop more consistent criteria for the initial velocity value in cases where the results might be significantly altered. The method of calculation used here has been to fix the initial velocity parameter and then to adjust the initial beam radius until a focused solution is obtained that repeats with each magnetic period. A significantly different normalized entrance velocity would have the effect of altering the average space charge in the beam which would result in obtaining a different focusing radius for the final solution. In such cases one must interpret the meaning of the normalizing parameters  $r_0$  and  $u_0$  which, in the analysis, are free to have arbitrarily fixed values. They are most meaningful when they can be related to the equivalent solenoid focused beam radius and velocity.

The axial velocity effect of the focusing parameter  $\gamma$  can be approximated by integrating Equation (40) (Appendix A) with the assumptions of negligible ripple ( $y = 1.0$ ), negligible variations in  $\dot{z}$  ( $x = \omega t$ ), sinusoidal focusing fields and negligible axial electric fields. When this is done one gets the following expression for  $\dot{z}/u_0$ :

$$\frac{\dot{z}}{u_0} = x = \alpha\gamma(\sin^2 x + \sqrt{2K} \cos x) + \text{constant} \quad (6)$$

This is simplified even further for the case of  $B/B_{Br} = 1.414 \dots$ , which corresponds to  $K = 1/2$ . For this degree of confinement we find, approximately, that

$$\frac{\dot{z}}{u_0} = \alpha\gamma (\sin^2 x + \cos x) + \text{constant} \quad (7)$$

where the constant term is of the order of unity for values of  $u_0$  equal to the physical beam velocity.

The expression enclosed in parentheses is plotted in Figure 3. As later examples will show, this curve depicts the general character of the axial velocity variations that are obtained from more complete computer solutions. Also shown in the figure is the average value of the function along with a value approximating what would correspond to a reference velocity at the center of the beam. In regions where the beam envelope has little or no rotation the velocity becomes greater than that of the beam center due to the space charge potential depression in the beam. On the other hand, beam rotation produced by the peak fields in the magnetic gaps results in axial velocities somewhat lower than this value, the actual amount depending upon the sign of the gap field and upon the degree of confinement (cathode immersion). The maximum velocity reduction occurs in the magnetic gap where the field is opposite in sign to the field at the cathode surface.

Estimates of appropriate design values for  $\gamma$  can be obtained from the above expressions. Actual designs should be checked in greater detail by using the complete computer solution. Using the example of Figure 3 it is seen that the beam envelope on the average would be about  $0.6\alpha\gamma$  slower than the average velocity at the center of the beam. (The difference between the beam reference and the average envelope velocity

G5679

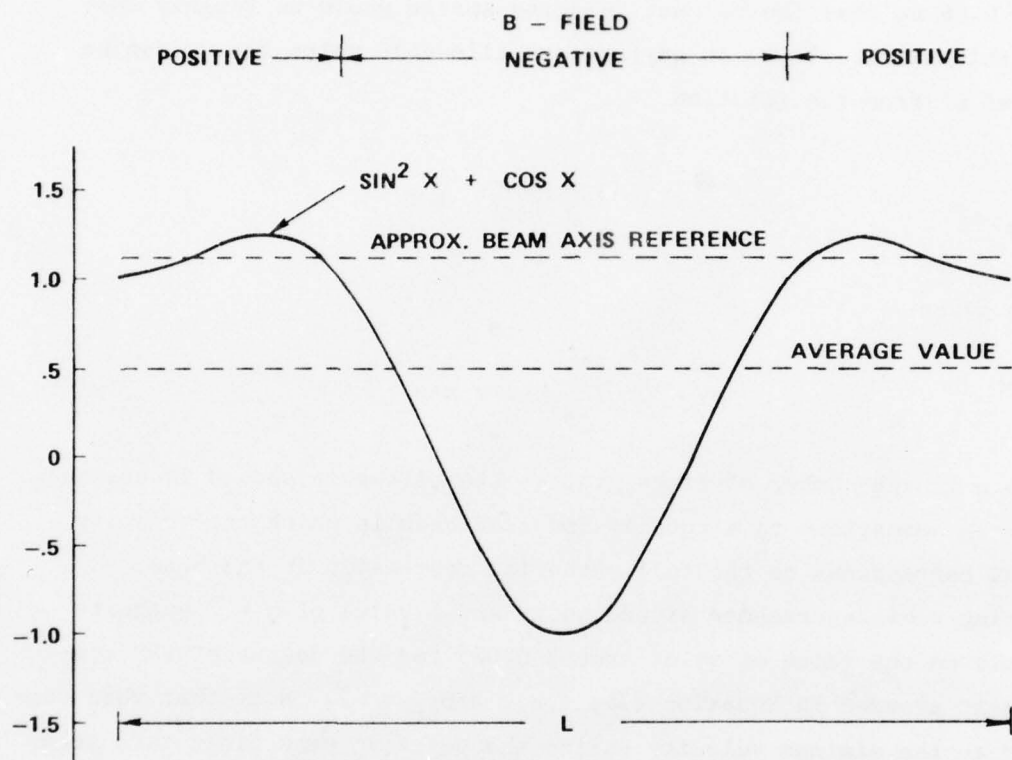


Figure 3 Plot of expression related to axial velocity variation for the case  $B/B_{Br} = \sqrt{2}$ . (The vertical scale actually becomes units of  $\alpha\gamma$ .)

is approximately 0.6 and the coefficient of the expression in Equation (7) is  $\alpha\gamma$ .) As a guide to how much velocity variation across the beam would be acceptable one can arbitrarily choose a factor like one or two times the velocity spread associated with the space charge potential depression in a uniform beam. The percent potential depression is like  $\mu\text{Perv}/0.66$  so that the percent velocity spread would be roughly one-half this value. Thus, an approximate allowable value for  $\alpha\gamma$  can be arrived at from the relation

$$0.6 \alpha\gamma = \frac{1}{2} \frac{\mu\text{Perv}}{66} \times n \quad (8)$$

which gives

$$\alpha\gamma \approx 0.0125 \mu\text{Perv} \times n \quad (9)$$

where  $n$  is the number of times greater the allowable spread is assumed to be in comparison to a totally immersed beam in which the velocity spread corresponds to the full potential depression in the beam. Assuming a microperveance around unity and a value of  $n = 2$  suggests a limit on the value of  $\alpha\gamma$  of around 0.025 for the degree of PPM confinement assumed in Equation (7), i.e.,  $B/B_{Br} = \sqrt{2}$ . Note that when compared to the minimum velocity during the positive peak field this actually produces a velocity slow-down during the negative peak field of  $2\alpha\gamma$ , or approximately 5%. This corresponds to approximately 10% in terms of equivalent voltage.

Since, in general, the magnitude of the axial velocity variation is proportional to  $\alpha\gamma$ , where

$$\alpha\gamma = \left( \frac{n B_{rms} r_o}{2 u_o} \right)^2, \quad (10)$$

it is of interest to determine how this factor can be minimized. In non-relativistic terms

$$u_o^2 = 2\eta v_o \quad (11)$$

and

$$B_{Br}^2 = \frac{\sqrt{2} \text{ (Perveance)} (v_o)}{\pi \epsilon \eta^{3/2} r_o^2} \quad (12)$$

which makes

$$\alpha_y = 0.015 \left( \frac{B_{rms}}{B_{Br}} \right)^2 \cdot \mu \text{Perveance} \quad (13)$$

Thus, to the approximations involved, the coefficient of the velocity variation term is only lowered by either lowering the perveance of the beam or by reducing the degree of confinement.

In addition to the  $\alpha_y$  coefficient, the confinement parameter  $K = 1 - (B_{Br}/B)^2$  also influences the extremes of the velocity variation, as seen from Equation (6). However, for any given degree of beam confinement, the adverse effect of velocity variation is only controlled by means of perveance.

Equation (10) also indicates that the focusing period does not directly influence the magnitude of the velocity variations. This is a result of the fact that the rotational energy depends upon the total change in flux linkages. Changes in flux linkages are only dependent on the magnitude of the B-field reversals and upon the beam diameter. Changes in period mainly only effect the time span over which the velocity changes take place. An example of this will be noted later in connection with Figures 11 and 12.

### 3.3 FOCUSING STUDIES FOR INCREASED BEAM STIFFNESS

A considerable portion of the present program was devoted to studying ways to improve the defocusing characteristics of the beam by means of greater beam stiffness which would offer greater resistance to focusing perturbations such as those that accompany high level RF modulation in the beam. Much of this was carried out by computer analysis of confined PPM beam flow using the paraxial model described earlier, the analysis of which is found in Appendix A.

Both integral pole piece focusing (RF circuit and magnetic structure common to each other) and external focusing (magnetic structure entirely external to the RF circuit) were considered.

Examples of computer calculations for some representative high power PPM focused beams are presented in Figures 4 to 7 and also in Figures 10 to 12. These beams are typical of the power and voltages employed to achieve 100 kW or more RF power in a coupled cavity TWT configuration. The initial examples actually pertain to the 559H tube assuming a beam filling factor of 0.5 (the voltages correspond to the axial velocity rather than to the actual circuit voltage).

It should be explained that in these computer examples the ratio of  $\alpha/\beta$  does not necessarily agree with Equation (5) in terms of the degree of confinement used. This is because the actual Brillouin field was calculated from a non-relativistic formula

$$B_{Br} = \frac{653.7}{\text{dia}} \sqrt{\frac{I_0}{(V_{axis})^{1/2}}} \text{ (gauss, amps, inches, volts)} \quad (14)$$

which is based on voltages rather than velocities.

While this value (used along with  $B/B_{Br}$  in calculating  $B_{rms}$  and  $\alpha$ ) is closer to being relativistically correct, it is not consistent with calculating the space charge term,  $\beta$ , from the beam velocity,  $u_0$ . The ratios of  $B/B_{Br}$  are consistent with the values of flux assumed in the cathode, and slight discrepancies between the  $\alpha$  and  $\beta$  parameters are readily absorbed in the computer process for finding the  $r/r_0$  balancing condition of the focused beam. Since  $\beta$  depends on  $r_0$ , different balancing radii can be interpreted in terms of different  $\beta$  with different normalizing radii than the one used in the actual calculation.

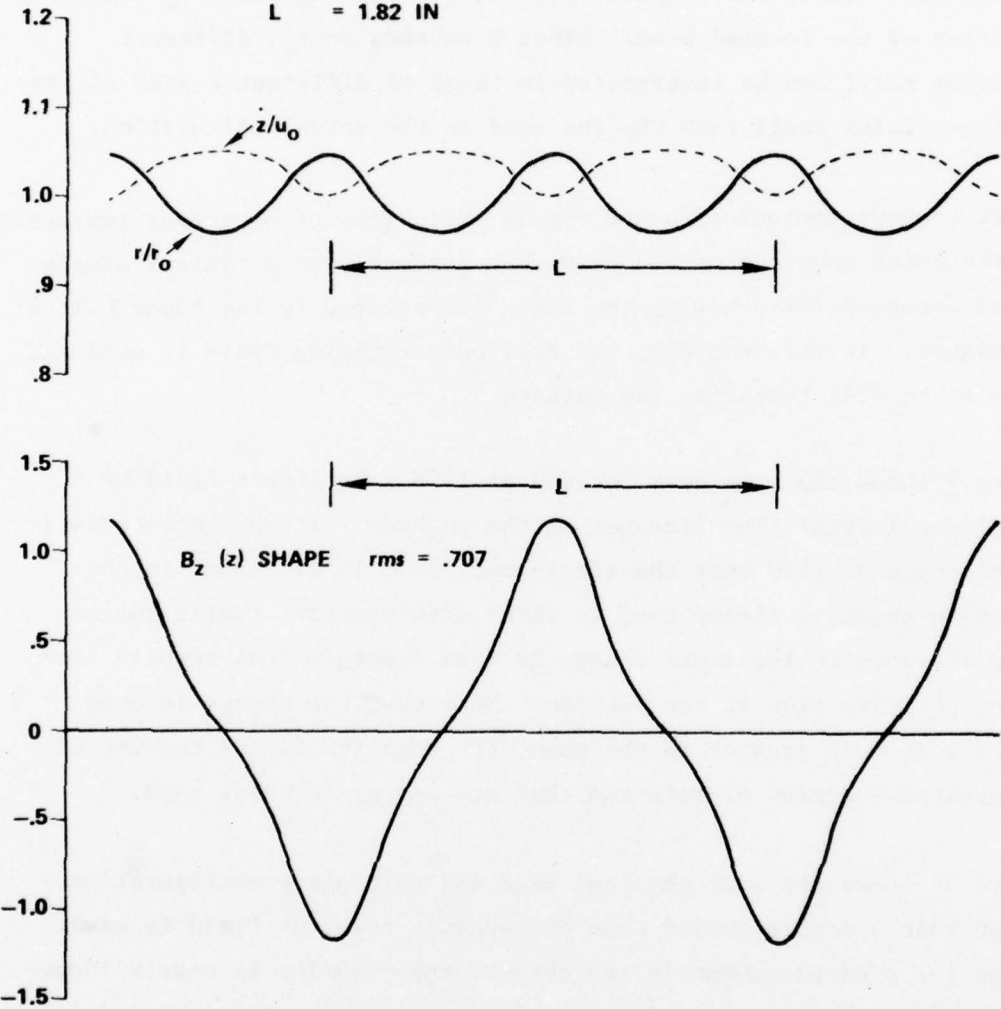
Figure 4 shows the velocity and ripple variations of electrons representing the outer envelope of the beam when focused with a typical single period focusing field having the shape illustrated in the lower half of the figure. In this example, the Brillouin focusing field is used and there is no flux threading the cathode.

Figure 5 shows the same beam focused at 1.25 x Brillouin field by permitting initial flux linkages in the cathode. It is characteristic of this type of flow that the ripple amplitude is different in the gaps with negative fields than in those with positive fields due to the difference in the total change in flux linkages that results from having positive flux at the cathode. Note that the change in beam velocity is much greater in the gaps with negative fields because of the greater energies of rotation that are set up in these gaps.

Figure 6 shows the same physical beam and pole piece configuration except that a double period type of magnetic focusing field is used. Except for a displacement in the curves, the focusing is nearly identical to that of Figure 4. This displacement results from the initial values of  $\dot{z}/u_0$  that were used in starting each of the calculations. In both cases this parameter was set equal to unity, but due to the

G5680

$V_o$	= 42000 VOLTS	$\alpha$	= .127
$I_o$	= 17.0 AMPS	$\beta$	= .135
$r_o$	= 0.149 IN	$\gamma$	= .265
$u_o$	= 4.512 IN/NSEC	$\alpha\gamma$	= .034
$B/B_{BR}$	= 1.0	$K$	= 0
$B_{rms}$	= 631.8 GAUSS		
$L$	= 1.82 IN		

Figure 4 Single period focusing with  $B/B_{Br} = 1.0$ .

Q5681

$V_0$	= 42000 VOLTS	$\alpha$	= .190
$I_0$	= 17.0 AMPS	$\beta$	= .135
$r_0$	= 0.149 IN.	$\gamma$	= .205
$u_0$	= 4.512 IN./NSEC	$\alpha\gamma$	= .063
$B/B_{BR}$	= 1.25	$K$	= .36
$B_{rms}$	= 789.7 GAUSS		
$L$	= 1.82 IN		

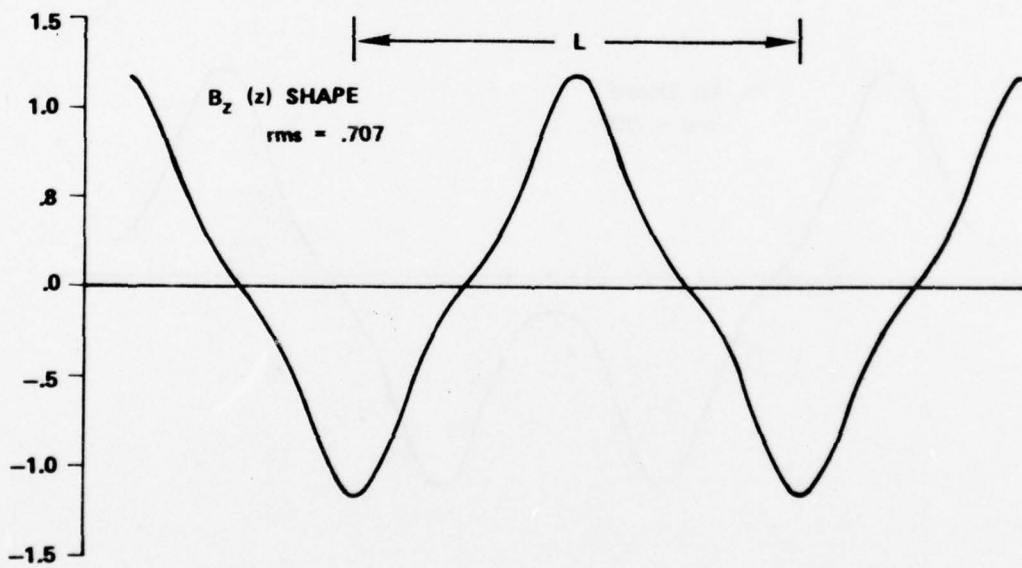
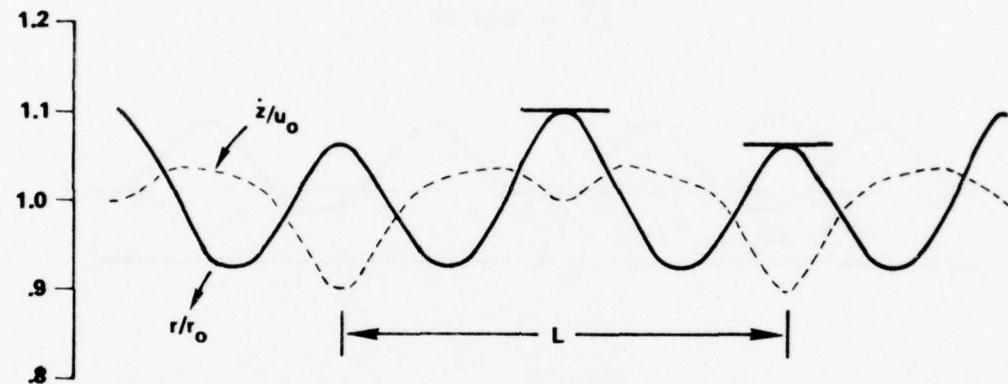


Figure 5 Single period focusing with  $B/B_{BR} = 1.25$ .

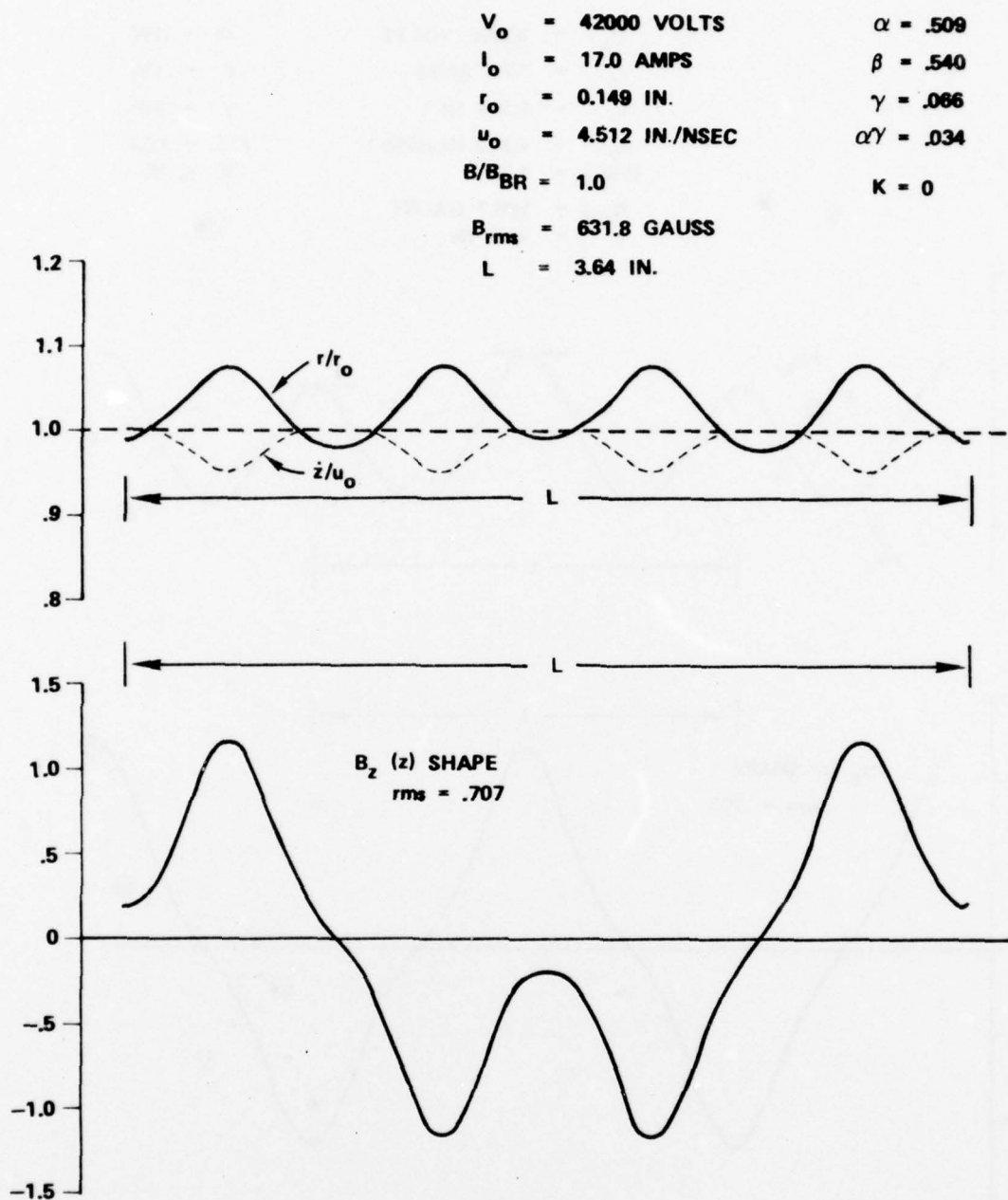


Figure 6 Double period focusing with  $B/B_{BR} = 1.0$ .

different starting points in the focusing cycle the average values for  $\dot{z}/u_0$  are slightly different for the two cases. As a result, the slower beam focuses at a slightly larger beam radius.

Figure 7 shows the scalloping that is produced over ten magnetic periods when the beam of Figure 4 is deliberately injected away from the minimum ripple or equilibrium focusing condition. In this case,  $\lambda_{sc}/L$  is approximately 1.95.

A number of alternatives were considered for improving the performance of permanent magnet focused tubes. Among these was the possibility of using external magnetic focusing structures in order that the magnetic period could be independent of the RF circuit structure. This would permit shorter focusing periods than is obtained with integral focusing, which could improve focusing characteristics in designs where additional field was to be used for improving beam stiffness by means of confinement.

The principle reason for considering partially confined PPM focusing with flux in the cathode is to obtain a focused beam that will be more resistant to defocusing under RF drive. Solenoid focused tubes often use between 2 and 2-1/2 times the Brillouin field. In PPM focusing, however, since  $\alpha$  is proportional to  $B^2 L^2 / u_0^2$ , for any given beam one cannot increase  $B$  without decreasing the magnetic period  $L$  if the same quality of focusing is to be maintained. Unfortunately, in the high power coupled-cavity TWT examples studied this would generally mean using a focusing period shorter than the actual RF circuit period. This could only be achieved with a focusing structure external to the circuit, which creates a real problem with regard to generating the required field on the axis. Even with the large coercive force of rare earth

G5683

$V_0$	= 42000 VOLTS	$\alpha$	= .127
$I_0$	= 17.0 AMPS	$\beta$	= .135
$r_0$	= 0.149 IN.	$\gamma$	= .265
$u_0$	= 4.512 IN./NSEC	$\alpha\gamma$	= .034
$B/B_{BR}$	= 1.0	$K$	= 0
$B_{rms}$	= 631.8 GAUSS		
$L$	= 1.82 IN.		

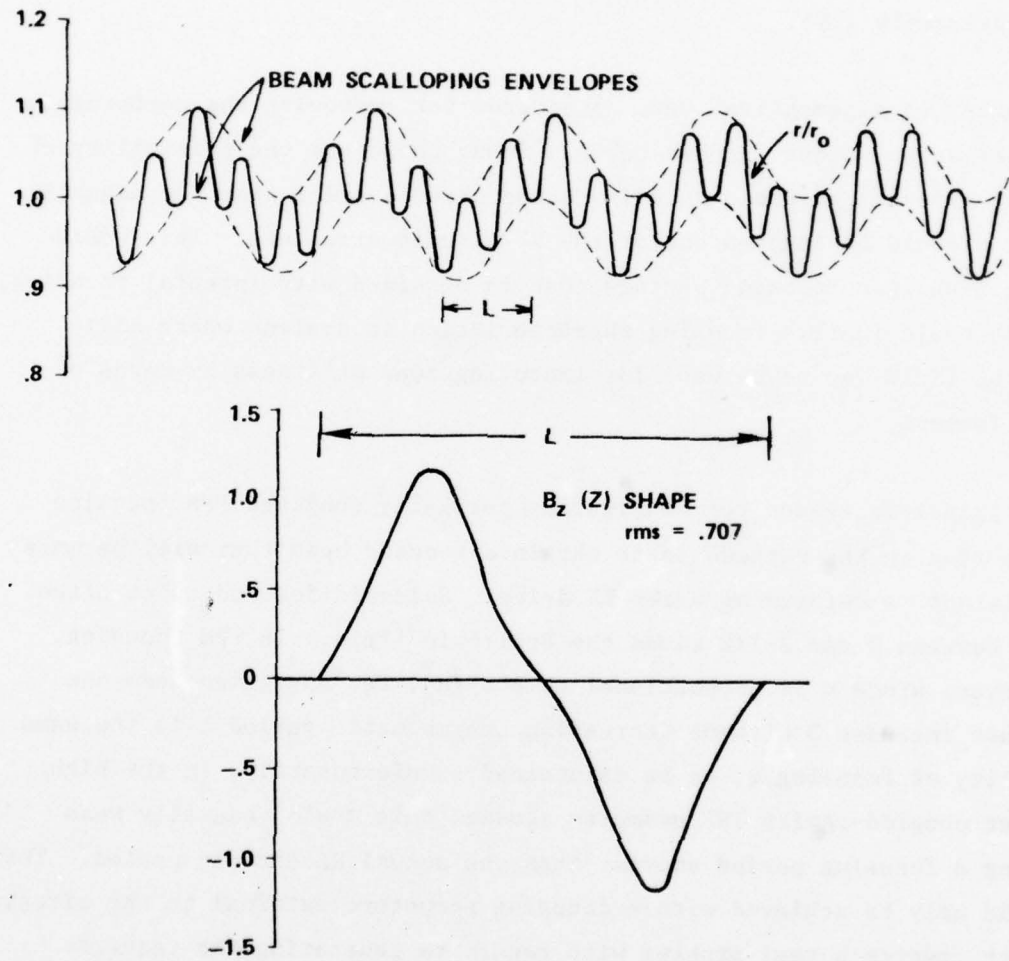


Figure 7 Beam scalloping for injection of beam at other than equilibrium balance condition.

magnets it becomes marginal if not impractical to produce short period, high axial fields with magnetic pole piece structures entirely external to the RF circuits.

Since a magnetic circuit exactly scales dimensionally to give the same field strengths and pole piece densities a general set of curves was calculated for PPM pole piece configurations. These are similar to curves found in Sterrett and Heffner<sup>3</sup> except that the rms rather than peak field on the axis has been plotted, and instead of using the usual assumptions at the ferrule dimension of either a rectangular gap field (constant with distance) or of the pole piece ferrules being knife edge (infinitesimal in thickness), the coefficients of the harmonic field components have been taken as the average of the values calculated for each of these limiting cases. Experience has shown that this procedure produces fields quite representative of the actual field shapes associated with typical pole piece geometries.

The curves are shown plotted in Figures 8 and 9 both as a function of L/D and as a function of D/L. Figure 8 clearly demonstrates the functional behavior of the field on the axis with respect to shortening the magnetic period length. A typical high power S-Band coupled cavity tube with a magnetic circuit outside the RF cavity structure would have an L/D ratio of around unity assuming the same periodicity as the RF circuit and not allowing for any extra diameter due to the presence of loss button configurations for controlling circuit instabilities. As can be seen from Figure 8, at this value of L/D any further reduction in period would rapidly reduce the field available on the axis for focusing the beam. The direct effect of this is to limit the beam perveance that can be focused (particularly if confinement is being considered) which in turn leads to higher voltage, lower beam current designs in order to obtain the same DC power in the beam.

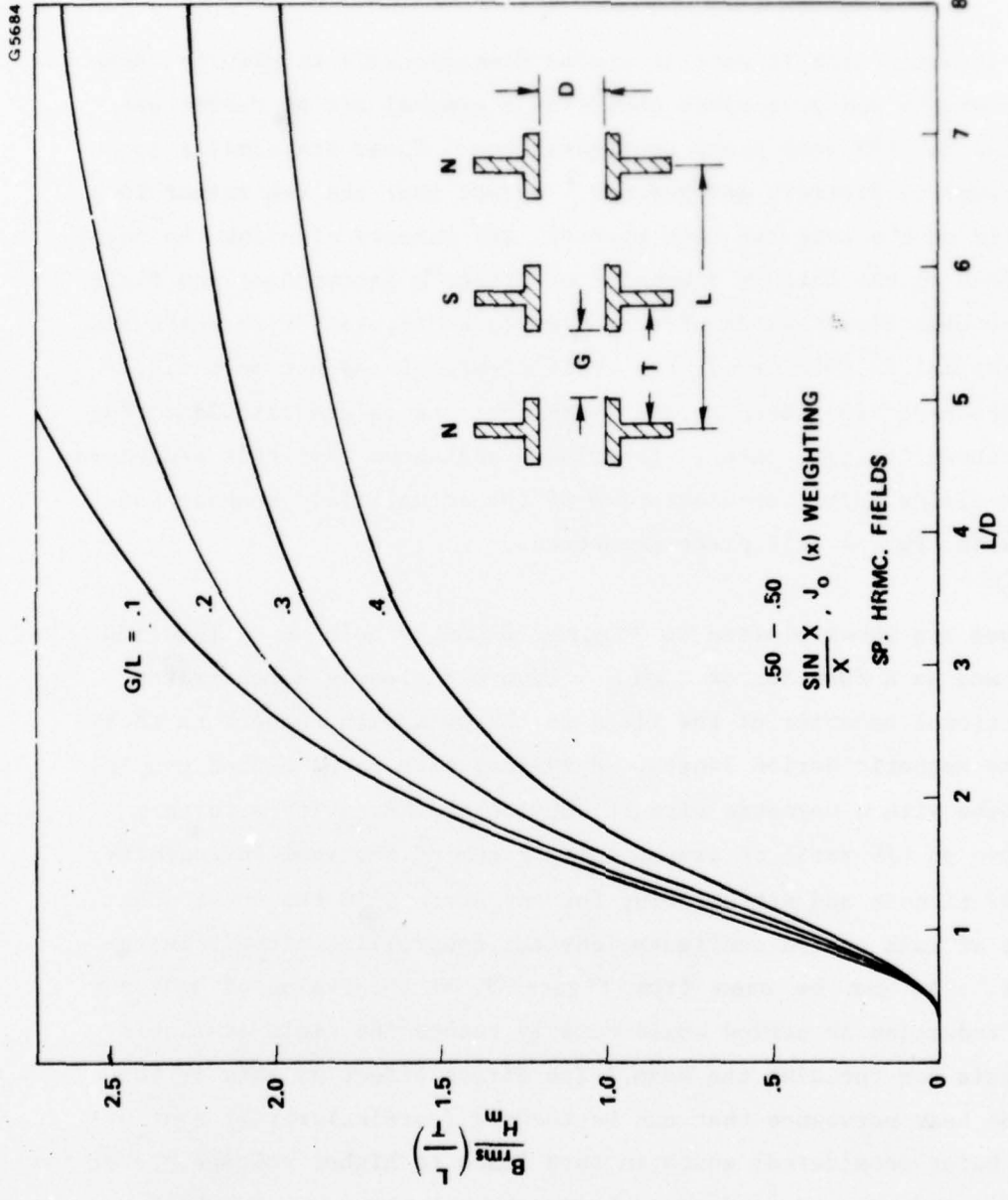


Figure 8  $B_{rms}$  on axis as a function of magnetic parameters.

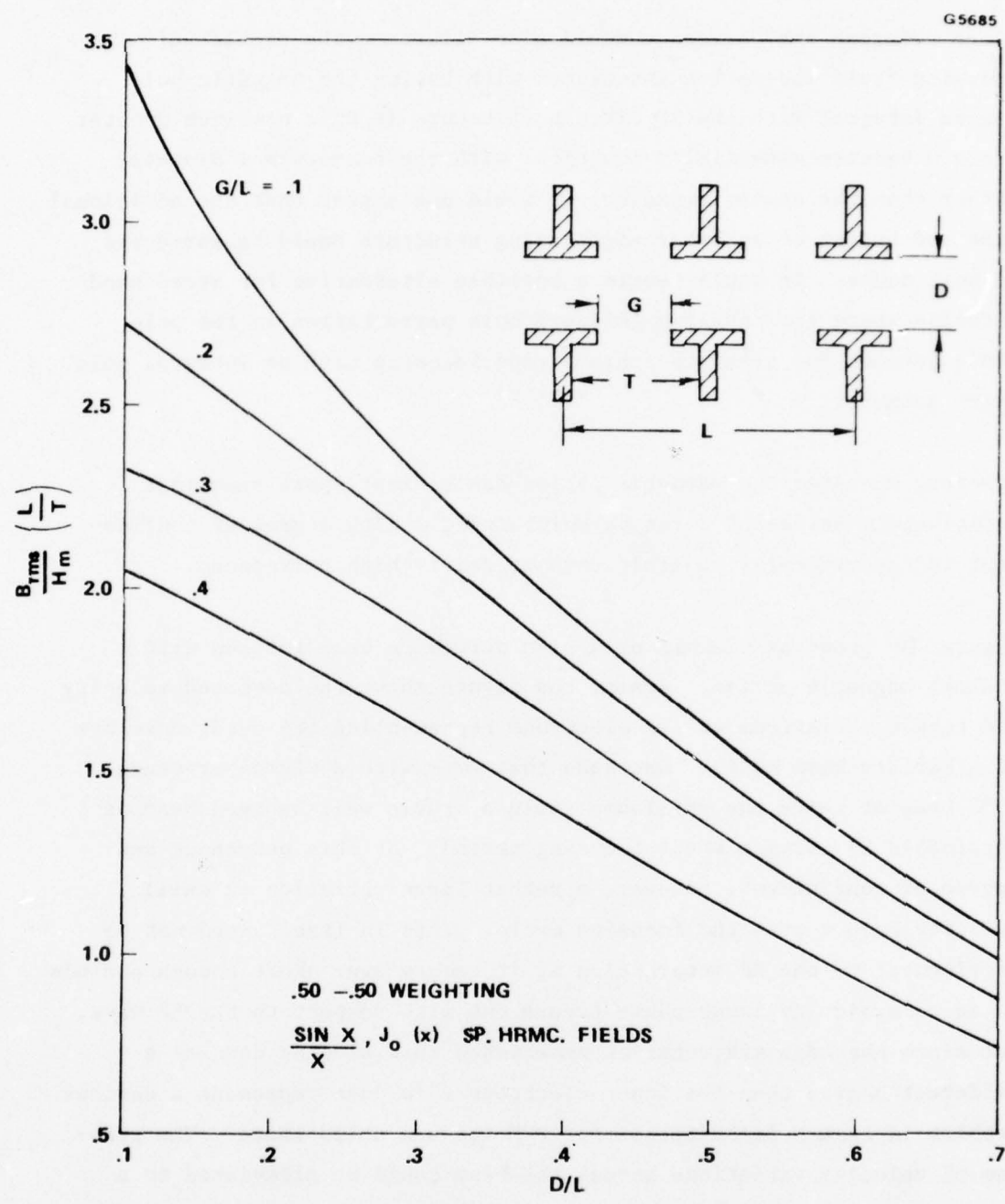


Figure 9  $B_{rms}$  on axis as a function of magnetic parameters.

Since reducing the permeance would also alleviate the problem of focusing field and period associated with having the magnetic pole pieces integral with the RF circuit structure (L/D is now much greater since D becomes essentially identical with the beam tunnel diameter rather than the cavity diameter) it would not appear that the additional size and weight of an external focusing structure would be warranted in most cases. It would remain a possible alternative for broad band circuits where the coupling (kidney) hole perturbation in the pole piece becomes too great to achieve good focusing with an integral pole piece geometry.

However, whenever the magnetic period can be kept short such that satisfactory values of  $\alpha$  can be maintained, a high degree of confinement is theoretically possible even at fairly high permeances.

Figure 10 shows an example of a high permeance beam focused with a short magnetic period. Again, the figure shows the computed velocity and ripple variations of the electrons representing the outer envelope of a laminar beam model. One sees that even with a micro-permeance 1.98 beam at twice the Brillouin field a stable well behaved beam is obtainable by using a short focusing period. At this permeance and degree of confinement, however, a rather large variation in axial velocity occurs over the focusing cycle. This in itself need not be detrimental to the RF interaction if it occurs over short enough periods so as to avoid any large phase excursions with respect to the RF wave, but since the edge trajectories experience this slowing down to a different degree than the inner electrons this does represent a serious problem in beam synchronization for PPM focused solid beams. The problem of velocity variations across the beam could be alleviated to a large degree by using hollow beams. In particular, in the case of Brillouin hollow beams (i.e., all electrons initially linking the same

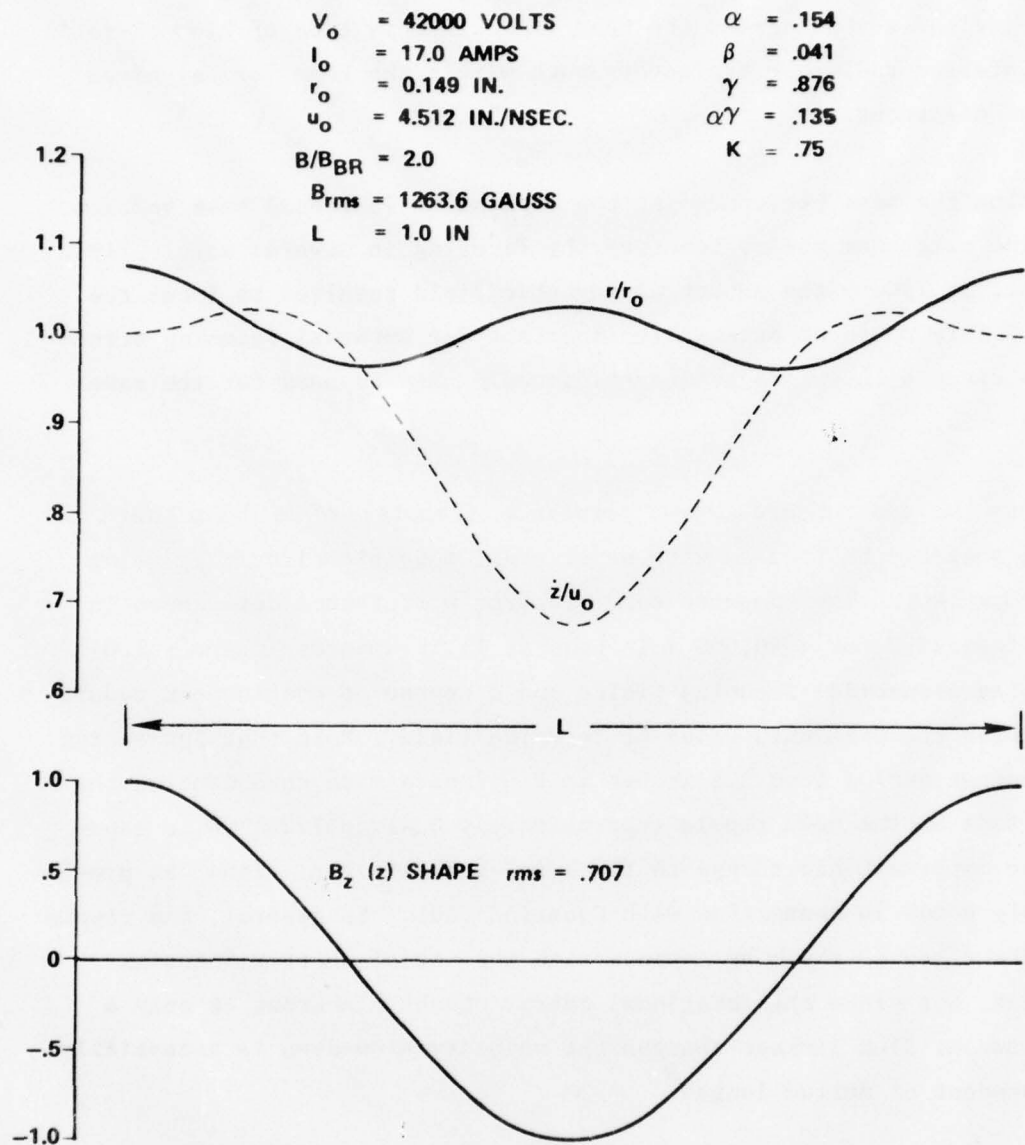


Figure 10 Example of hi-perveance confined beam flow employing short period magnetic fields.

amount of flux) there would be a tendency to average out most of the velocity variations across the beam since in this type of flow there is no preferred radius or trajectory path within the beam for any given set of electrons.

Reducing the beam permeance (at the expense of increased beam voltage for the same beam power) benefits the focusing in several ways. First of all, it lowers the amount of magnetic field required to focus the beam. This could be especially important for external focusing structures since a larger magnetic period could then be used for the same value of  $\alpha$ .

Figures 11 and 12 are lower permeance examples of a beam that could possibly be focused with an external magnetic circuit by using SmCo magnets. The computed edge electron performance data shown in the figures is for a 50,000 volt beam at 11.18 amperes ( $\mu\text{Perv} = 1.0$ ) assuming sinusoidal focusing fields and a degree of confinement requiring twice the Brillouin value of focusing field. Note that increasing the magnet period from 1.5 inches to 2.0 inches more than doubles the amplitude of the beam ripple (approximately 3.4% to 7.2%) while causing an imperceptible change in the axial velocity variations, as previously noted in connection with Equation (10). In general, the ripple and stability of the beam improve with the use of shorter focusing periods, but since the rotational energy of the electrons is only a function of flux linkage changes the velocity slow-down is essentially independent of period length.

In order to determine the magnitude of the effect of the axial velocity variation upon phase displacement with respect to a constant phase velocity the  $z/u_0$  data of Figure 11 was integrated to obtain the curve shown in Figure 13. In this figure the electron phase

G5687

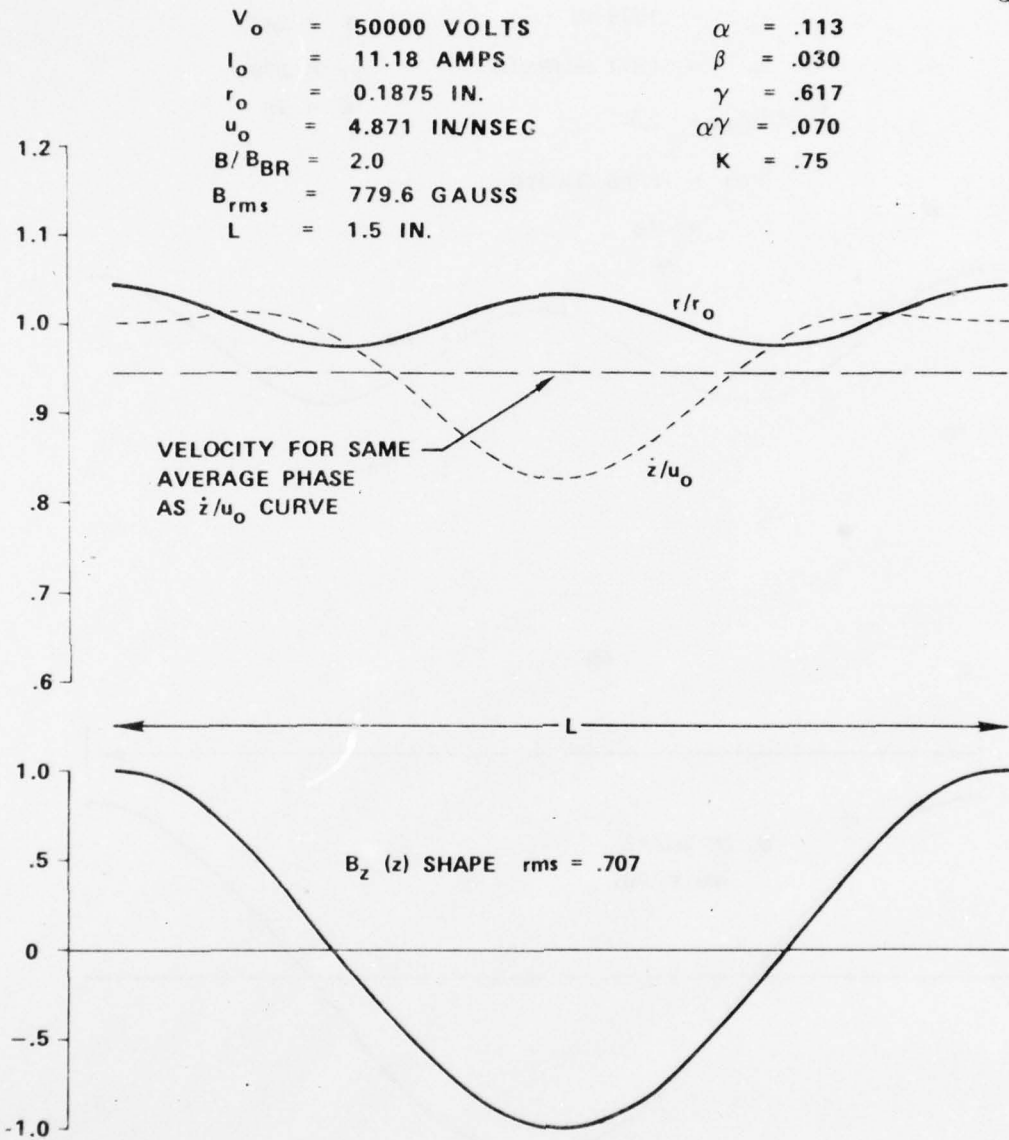


Figure 11 Edge electron calculations for confined PPM beam flow,  $L = 1.5$ .

G5688

$V_0$	= 50000 VOLTS	$\alpha$	= .201
$I_0$	= 11.18 AMPS	$\beta$	= .054
$r_0$	= .1875 IN.	$\gamma$	= .347
$u_0$	= 4.871 IN./NSEC	$\alpha\gamma$	= .070
$B/B_{BR}$	= 2.0	$K$	= .75

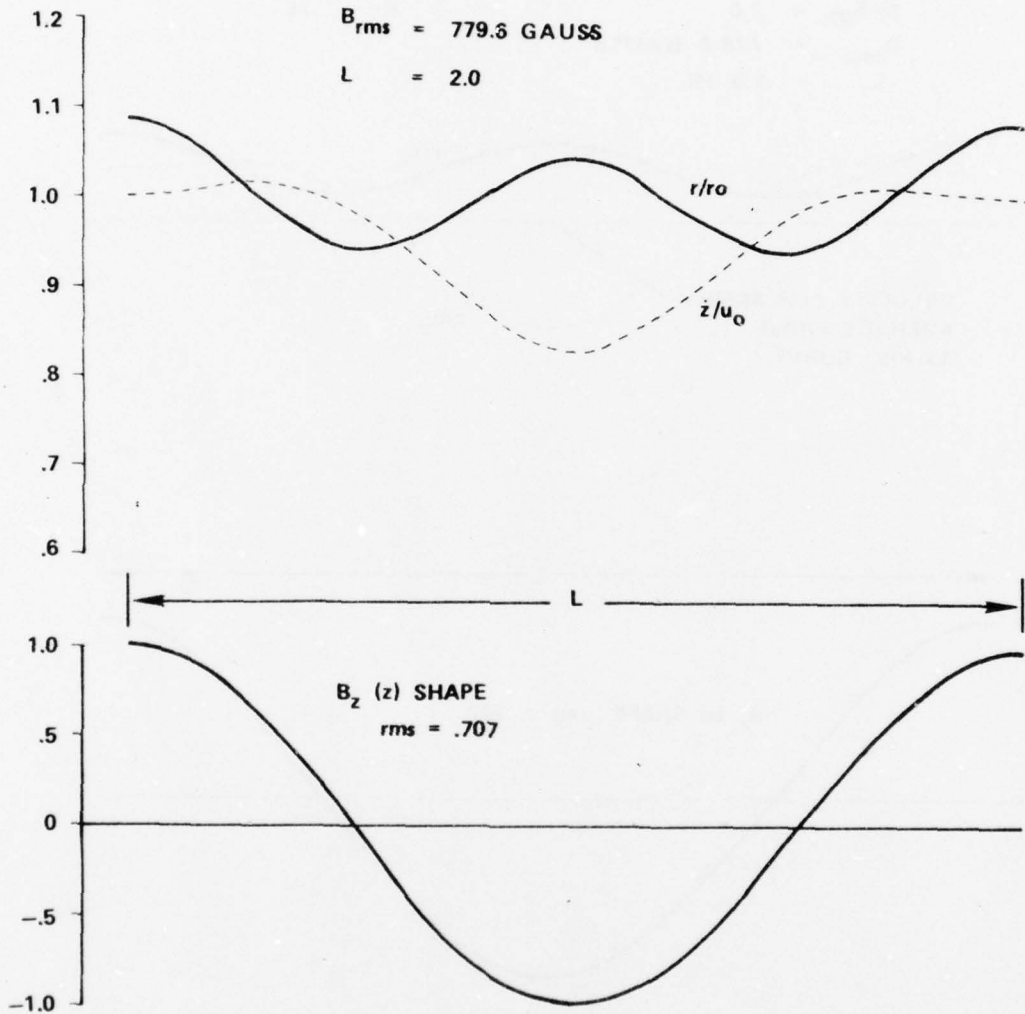


Figure 12 Edge electron calculations for confined PPM beam flow,  $L = 2.0$ .

G5689

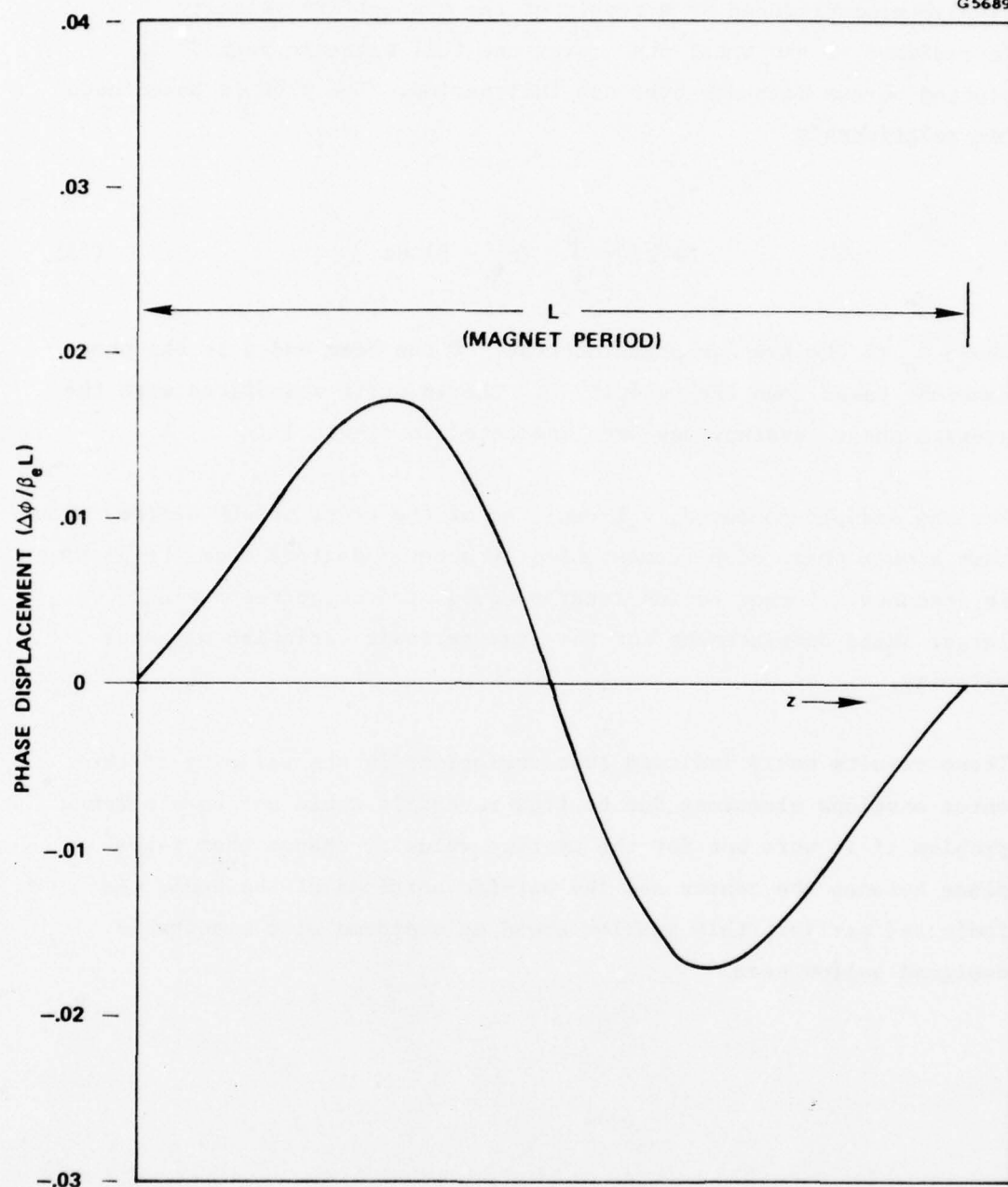


Figure 13 Normalized phase displacement from average phase due to  $\dot{z}/u_0$  variation shown in Figure 11.

displacement produced as a result of the non-uniform velocity (normalized to the total phase over one full magnetic period) is plotted versus distance over one full period. The plot is based upon the relationship

$$\Delta\phi(z) = \int_0^z (\beta_e - \beta) dz \quad (15)$$

where  $\beta_e$  is the average phase constant of the beam and  $\beta$  is the phase constant based upon the velocity  $z$ . The velocity associated with the average phase constant has been indicated in Figure 11.

For the example computed,  $\beta_e L$  would be of the order of 400 degrees such that a peak phase displacement of only about 7 degrees from the average is produced. Longer period lengths would produce correspondingly larger phase displacement for the same periodic variation of axial velocity.

These results would indicate that variations in the velocity of the outer envelope electrons due to flux reversals would not be a serious problem if it were not for the average velocity change that takes place between the center and the outside portions of the beam. As indicated earlier, this problem could be overcome with a suitably designed hollow beam.

### 3.4 TUBE AND FOCUSING PARAMETER RELATIONSHIPS

It is difficult to set arbitrary parameter limits for achieving good focusing when in reality the functional parameters are essentially continuous in nature. In this report it has generally been assumed that for moderate ripple and to maintain a reasonable margin for beam instabilities,  $\alpha$  should have a maximum value of about 0.15. This maintains a nominal theoretical ripple amplitude of just under 5%. Earlier, for  $B/B_{Br}$  ratios in the range 1.3 - 1.4, a limit on  $\alpha\gamma$  of 0.025 was suggested to avoid excessive velocity spreads across the beam which could adversely affect the RF beam-circuit interaction. Combining these limits results in a typical value for  $\gamma$  of around 1/6. It is perhaps interesting to note that for a Brillouin focused beam with  $\beta = \alpha = 0.15$  the corresponding  $\lambda_p/L$  parameter from Equation (37) is around 1.83.

One of the difficulties in studying ways to improve the performance of permanent magnet tubes is the multitude of interrelated tube and focusing parameters that are involved. If one looks at the problem of improving the focusing in existing designs (such as the examples studied in connection with this program) there are a number of parameters associated simply with alternative focusing configurations that can involve various degrees of beam confinement. Added to this is the fact that the tube RF parameters overlap with the focusing parameters to the point where changes in the RF design can greatly affect the kind of focusing that can be achieved. Consequently, one cannot separate the focusing optimization from the total tube design.

Some insights into fundamental design limitations and possible tube and focusing tradeoffs can be obtained through an examination of some basic relationships along with typical values of parameters. For this discussion the following definitions of parameters has been used. The

context in which a parameter is used should avoid any confusion in cases where similar symbols have also been used in connection with parameters described in the periodic focusing discussion.

$\ell_c$  = RF cavity period  
L = magnetic focusing period  
 $\alpha$  = magnetic focusing parameter  
 $H_m$  = operating H of permanent magnet material  
D = magnetic pole piece I.D.  
f = Center operating frequency  
G = magnetic pole piece gap length  
g = RF circuit gap length  
 $\beta$  = RF phase constant ( $2\pi f/v$ )  
 $\beta_e$  = beam phase constant ( $2\pi f/u_0$ )  
 $\eta$  = electron charge to mass ratio  
d = beam diameter (2b)  
b/a = beam filling factor  
2a = beam tunnel diameter  
 $\gamma a$  = electrical measure of beam tunnel radius, where

$$\gamma a = \beta a \sqrt{1 - v^2/c^2}$$

$u_0$  = beam velocity

In cavity type circuits the alternatives for PPM focusing are to have the magnetic structure external to the RF circuit such that the magnet period can be independent of the circuit period, or to have the magnetic

circuit integral with the RF circuit, in which case a full magnetic period equals twice the cavity period.

It has been pointed out earlier that to confine a PPM beam with additional magnetic field and not degrade the focusing, since  $\alpha$  is proportional to  $B^2 L^2$ , the magnetic period must be decreased in inverse proportion to any increased field strength. Unless the required magnetic period for good focusing remains greater than the RF circuit period, a focusing structure external to the circuit may be necessary. This would normally be undesirable from the standpoint of additional size and weight, and it is quite possible that the external structure would not be capable of producing the focusing fields required.

In the case of integral focusing the requirement for magnetic period is

$$L = 2 \ell_c \quad (16)$$

The following expression is actually an identity

$$2 \ell_c = \frac{\beta e \ell_c}{\pi} \cdot \frac{u_0}{f} \quad (17)$$

Also, from the definition of  $\alpha$ , we may write

$$L = \frac{u_0}{B} \sqrt{\alpha} \cdot \frac{4\pi}{n} \quad (18)$$

Combining Equation (17) with Equation (18) gives the following results

$$\frac{2 \frac{\ell}{c}}{L} = \frac{\eta}{4\pi} \frac{\left(\frac{\beta \ell_c}{\pi}\right)}{\sqrt{\alpha}} \frac{B_{rms}}{f} \\ = 1.4 \frac{\left(\frac{\beta \ell_c}{\pi}\right)}{\sqrt{\alpha}} \frac{B_{kgauss}}{f_{GHz}} \quad (19)$$

From the non-relativistic relationship for the Brillouin focusing field one can express

$$\frac{B_{kgauss}}{f_{GHz}} = \frac{0.088 \sqrt{\mu Perv}}{\beta_e^b} \left( \frac{B}{B_{Br}} \right) \quad (20)$$

where  $(B/B_{Br})$  is the ratio of the actual focusing field to the Brillouin value of field.

Substituting Equation (20) into Equation (19) yields

$$\frac{2 \frac{\ell}{c}}{L} = 0.1231 \frac{\left(\frac{\beta \ell_c}{\pi}\right)}{\sqrt{\alpha}} \frac{\sqrt{\mu Perv}}{\beta_e^b} \left( \frac{B}{B_{Br}} \right) \quad (21)$$

Most coupled-cavity tubes operate with a hot bandwidth centered around  $\beta \ell_c / \pi = 1.4$ , where  $\beta$  is the RF circuit phase constant. Since the ratio of beam to circuit velocity,  $u_0/v = \beta/\beta_e$ , is typically of the order of 1.07 at or near band center, a nominal value for  $\beta_e \ell_c / \pi$  at band center would be 1.3. Actually, the ratio of  $\beta/\beta_e$  is a function of beam permeance, but the above assumptions are quite valid for

pervance in the neighborhood of unity. The value of  $\beta_e b$  is a function of the beam size. For typical  $\gamma_a$ 's of around unity  $\beta_e b$  would be essentially the nominal value of the beam tunnel filling factor, which would normally be 0.55 - 0.60. Using  $\alpha = 0.15$  to avoid excessive beam rippling and to give the desired margin of beam stability and combining with the other assumed parameter values reduces Equation (21) to the approximate expression

$$\frac{2 \ell_c}{L} \approx \sqrt{\mu Perv/2} \left( \frac{B}{B_{Br}} \right) \quad (22)$$

From Equation (22) it is seen that for integral focusing (i.e.,  $2\ell_c/L = 1.0$ ) and  $B = B_{Br}$  a beam with  $\mu Perv \approx 2.0$  could be focused satisfactorily. On the other hand, at  $B = 2 \times B_{Br}$  only a  $\mu Perv \approx 0.5$  could be focused within the limitations of the assumed design parameters. Larger pervesances could be focused by assuming larger beam diameters, however, the above relationships only apply to the ability to focus the beam in terms of a limiting period. As indicated earlier, further restrictions on the beam diameter may be imposed as the result of rotational energy in the beam under various conditions of confinement. In fact, one can write the following identity from the definition of the focusing parameter,  $\gamma = (2\pi r_o/L)^2$ ,

$$\frac{2 \ell_c}{L} = \sqrt{\gamma} \left( \frac{\beta_e \ell_c}{\pi} \right) \frac{1}{\beta_e b} \quad (23)$$

provided the normalizing radius is made equal to the actual beam radius (i.e.,  $r_o = b$ ). It has already been shown that a reasonable value for  $\gamma$  might be 1/6 for moderate amounts of confinement. This value, combined with  $\beta_e \ell_c / \pi = 1.3$  would limit  $\beta_e b$  to 0.53 (for the case of

integral focusing with  $L = 2\ell_c$ ). Using this value for  $\beta_e b$  in Equation (21) would be even more restrictive on perveance than the expression given in Equation (22).

For the case of external focusing it is interesting to rewrite Equation (19) in terms of the diameter  $D$  of the external magnetic pole pieces. This can be done as follows:

$$\frac{B_{rms} (L/D)}{f} \equiv \frac{8\pi}{n} \frac{\sqrt{\alpha}}{\left(\frac{D}{\ell_c}\right)\left(\frac{\beta_e \ell_c}{\pi}\right)} \quad (24)$$

Again, the quantities on the right hand side of the identity tend to be relatively fixed, with the exception that the ratio  $D/\ell_c$  becomes smaller with higher voltage circuit designs. The RF cavity diameter ultimately determines the external magnetic pole piece diameter,  $D$ . It can be computed for different design voltages provided certain other cavity design parameters are determined. For example, a typical web thickness to cavity period ratio must be chosen along with a gap to period ratio, tunnel diameter to period ratio and thickness of the drift tube cylinder wall. All of these parameters stay within relatively fixed bounds for any given type of tube design. The cavity period itself may be computed from Equation (17).

Figure 14 presents pictorially examples of computed cavity diameters normalized to period length for several different design voltages and gap-to-period ratios. The assumption of a beam tunnel radius that is one-quarter the cavity period is consistent with assuming  $\gamma_a$ 's of around unity with an operating  $\beta\ell_c/\pi$  of 1.4. The other dimensions are typical values for structural and thermal considerations.

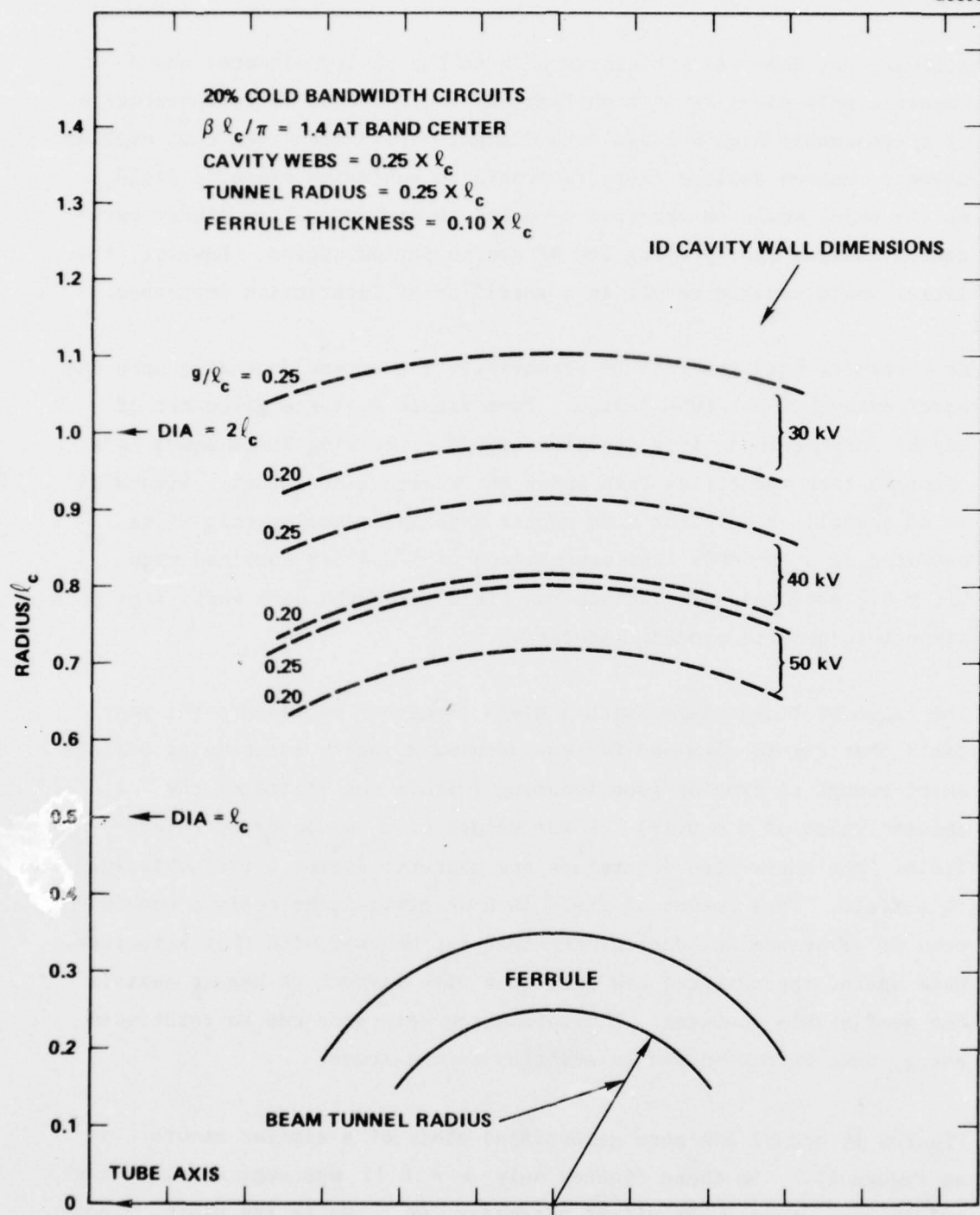


Figure 14 Calculated cavity diameters for various design voltages and  $g/\ell_c$  ratios.

Allowing for some wall thickness between the cavity diameter and a magnetic pole piece it is seen that  $D/l_c = 2.0$  would be representative of a reasonably high voltage tube design. It is also seen that smaller diameter magnet designs (more favorable to achieving magnetic field on the axis) would be obtained by going to higher voltage (lower perveance) designs and by using low RF gap to period ratios. However, the latter would usually result in a sacrifice of interaction impedance.

As a result, Eqdation (24) is essentially a constant depending upon the exact nature of the tube design. From Figure 8, for a given set of magnet parameters  $B$  is a function of  $L/D$ . Setting  $BL/fD$  equal to a constant then identifies each value of  $B$  with a frequency. Figure 15 is an example of this for SmCo magnet material assuming that it is operated at  $H_m = 6000$ . The assumptions of  $T/L = 1/3$  combined with  $G/L = 0.3$  produces near optimum rms field strengths with sufficient pole piece thickness to prevent saturation.

The value of  $B$  associated with a given frequency represents the most field that can be obtained for the assumed  $H_m$  while maintaining periods short enough to provide good focusing (within the limits of the assumed value of  $\alpha = 0.15$ ). Lower values of  $H_m$  would produce less field. The curve also determines the magnetic period  $L$  for achieving this field. This amount of field then determines the maximum combination of perveance and confinement that can be used with that structure. Here again, the criteria has only been with respect to magnet periods for good stable focusing. Limitations on beam size due to rotational energy must be considered in addition to the above.

Figures 16 and 17 are more generalized plots of a similar nature as Figure 15. In these figures only  $\alpha = 0.15$  was kept constant making the frequency a normalized parameter, as shown in the plots. These

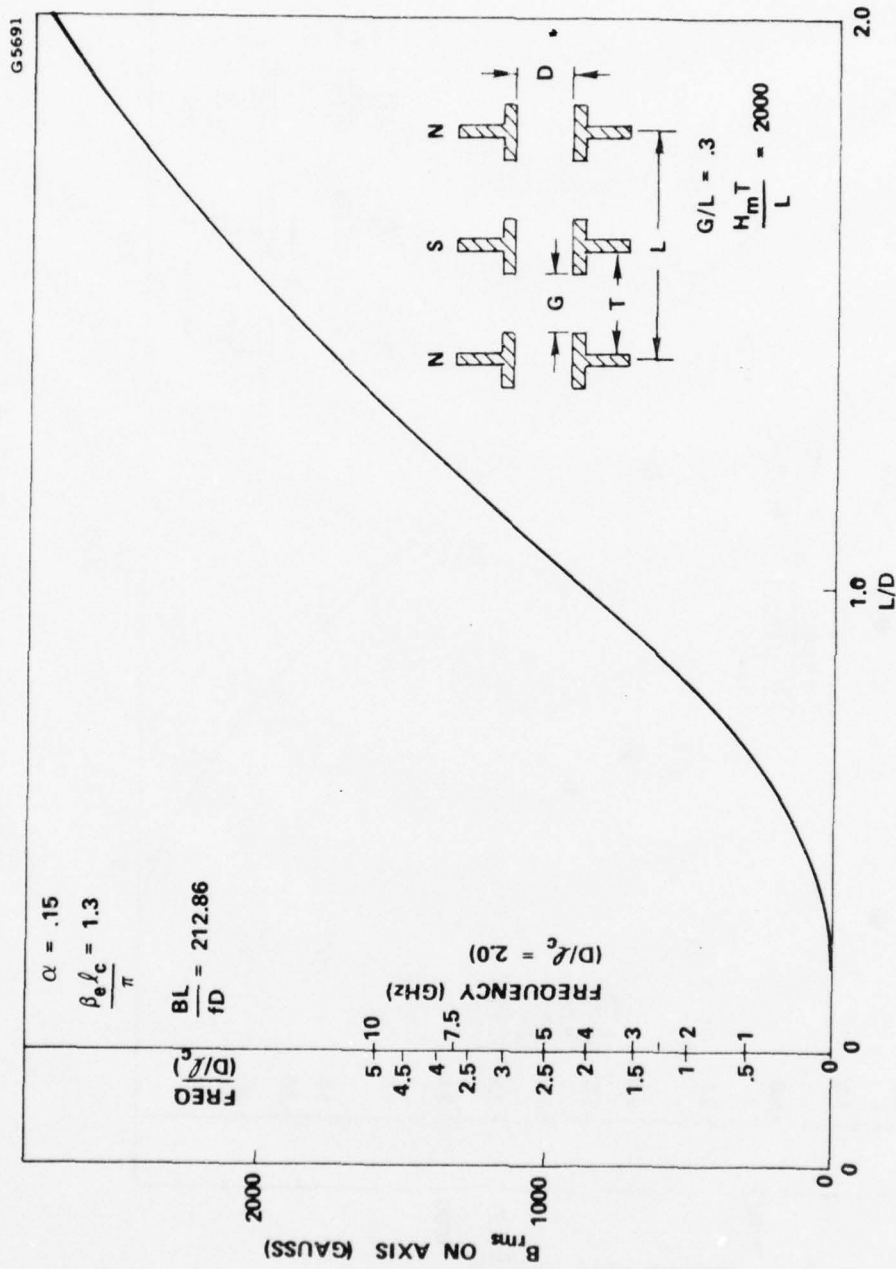


Figure 15 PPM design parameter curve.

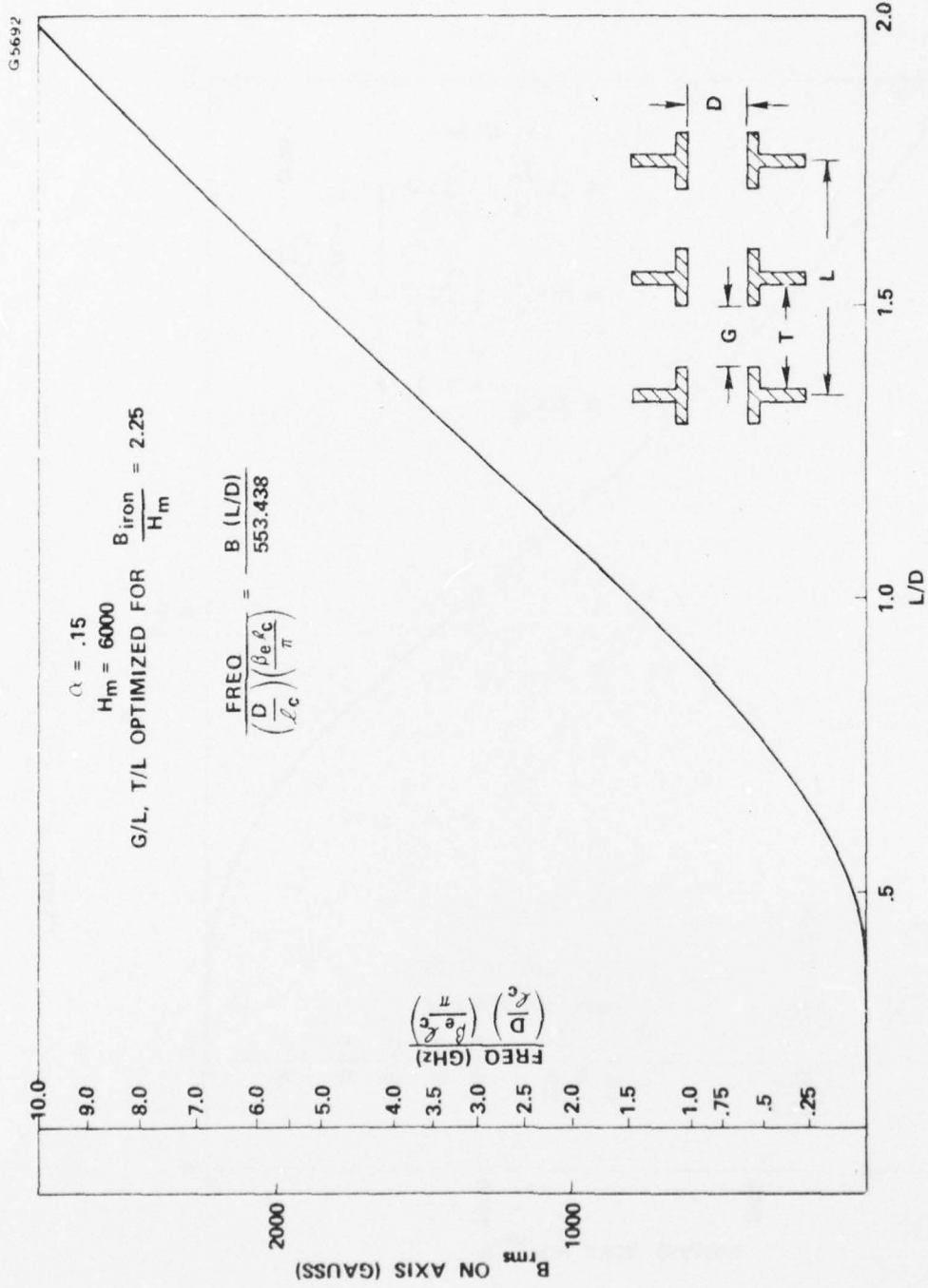


Figure 16  $B_{rms}$  vs  $L/D$  for  $H_m = 6000$ .

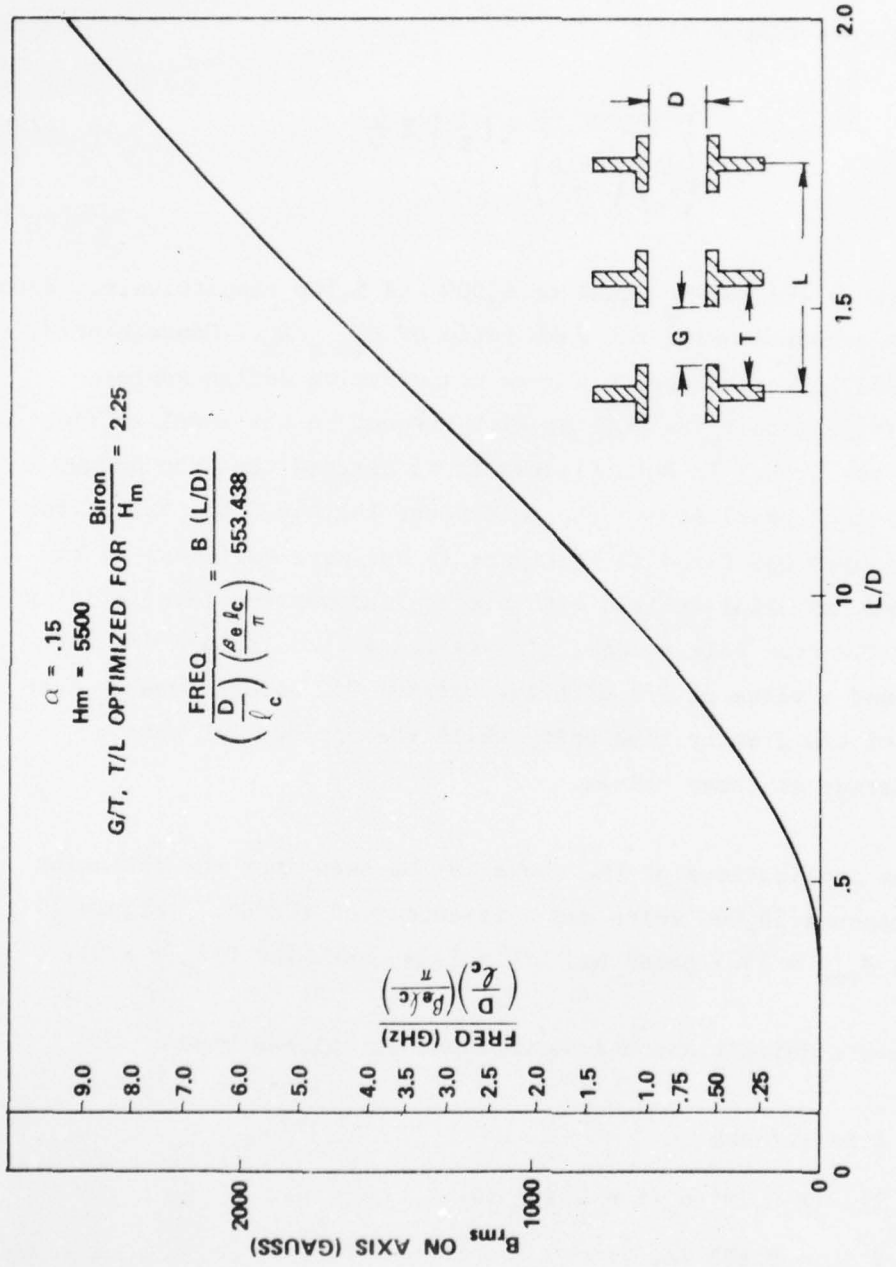


Figure 17  $B_{\text{rms}}$  vs  $L/D$  for  $H_m = 5500$ .

curves could still be used for other values of  $\alpha$  provided that the normalized frequency was further scaled with respect to the square root of  $\alpha$  in accordance with

$$\frac{\text{Frequency } \sqrt{\alpha}}{\left(\frac{D}{l_c}\right) \left(\frac{\beta l_c}{\pi}\right)} = \left(\frac{n}{8\pi}\right) B \frac{L}{D} \quad (25)$$

The two figures are for  $H_m$  equal to 6,000 and 5,500 respectively. Both curves were computed using the same ratio of  $B_{\text{iron}}/H_m$ . Consequently, the  $H_m = 5500$  curve represents a more conservative design approach, both with respect to  $H_m$  as well as with respect to the level of flux density in the iron. In both figures it is assumed that the magnet I.D. is in close proximity to the pole-piece ferrule O.D. Values for G/L and T/L were not fixed as in Figure 15 but were varied so as to optimize the rms axial B-field with a specified maximum level of flux density in the iron pole pieces. It was found that T/L and G/L both varied around a value of 1/3 with the optimum G/L being somewhat less at values of L/D greater than unity while the optimum T/L became somewhat larger at these values.

Some of the implications of the above may be seen from the following example. Assume 50,000 volts and a frequency of 10 GHz. Figure 15 then gives  $B_{\text{rms}} = 1585$  gauss and  $L/D = 1.34$  (assuming  $D/l_c = 2.0$ ).

From the above definitions and assumptions it follows that

$$u_o = 4.87 \text{ in/nsec}$$

$$l_c = 1/2 (\beta l_c / \pi) u_o / f = 0.317 \text{ in.}$$

$$D = 2 l_c = 0.633 \text{ in.}$$

$$L = 1.34 D = 0.849 \text{ in.}$$

$$2a = \frac{l_c}{c}/2 = 0.158 \text{ in.}$$

$$2b = 2a \cdot b/a = 0.087 \text{ in.}$$

$$\alpha = 0.15$$

$$\gamma = 0.10 \text{ (radial focusing parameter)}$$

where a typical beam filling factor of  $b/a = 0.55$  has been assumed.

Computing the Brillouin focusing field from the relationship,

$$B_{Br} = \frac{29.0766}{2b} \sqrt{\frac{I_o}{u_o/c}} \text{ (non-relativistic)} \quad (26)$$

allows one to generate the following data:

$I_o$	$B/B_{Br}$	$P_{d.c.}$	$\mu\text{Perv}$	Required Eff for $P_{out} = 100 \text{ kW}$
1	3.05	50,000	0.09	-
2	2.16	100,000	0.18	100%
4	1.52	200,000	0.36	50%
8	1.08	400,000	0.72	25%
9.3	1.0	464,795	0.83	21.5%

This data indicates that confined PPM beam flow would not be practical under these assumptions at this high frequency using external magnet structures, but a moderate (less than unity) perveance Brillouin focused beam would be practical. The advantage of the external focusing in this case would be simply the elimination of the iron pole pieces as part of the RF circuit structure. This eliminates the coupling (kidney) hole from the magnetic circuit in addition to increasing the thermal handling capability of the RF circuit. (One should note that the thermal conductivity of copper is greater than five times that of iron).

It is also interesting to note that the focusing period in this case (using external focusing) is actually greater than twice the cavity period, which is the magnetic period that would be associated with integral focusing. The magnetic period with external focusing depends a great deal upon the actual value of D that can be used with a given cavity design.

At lower frequencies the external focusing structure is capable of providing enough field to confine the beam in addition to eliminating the iron pole pieces from the RF circuit structure. If the above example is carried out for a frequency of 2.0 GHz it is found that the  $\mu\text{Perv} = 0.83$  beam can be focused using 1.6 times Brillouin field with a magnetic period of slightly more than 2.6 inches. In this instance the external focusing period is shorter than the period that would result from integral focusing. In fact, since the assumption that  $D = 2 l_c$  is made in these examples, the ratio of external period to that of using integral focusing is the same ratio as L/D. In general, the lower the frequency of the design, the greater the possibility of reducing the magnetic period (relative to the cavity period) by using external focusing.

### 3.5 RF DEFOCUSING WITH DRIVE

The one principal factor limiting high average power in PPM focused tubes is high beam interception by the RF interaction circuit under large signal drive. This problem is often overcome in solenoid tubes by confining the beam at two or more times the Brillouin focusing field. From the discussion on beam focusing it is clear that this would not be feasible with PPM solid beams except at very low perveances.

To determine the effectiveness of small amounts of beam confinement through the introduction of initial cathode flux linkages a study of typical beam electron trajectories in the presence of large signal RF fields was made. The study was carried out using the coupled cavity beam trajectory program TWTVA written by J.R.M. Vaughan under Navy Contract N00123-76-C-0424. Although this program does not allow the presence of cathode flux for the case of PPM fields, the results obtained for solenoid fields would be applicable to PPM cases where there is negligible slowing down of electrons as the result of rotational energy in the beam and where the PPM focusing parameters have been chosen to give small ripple amplitudes due to the PPM fields. Since these are the conditions of practical interest in any real tube design, the evaluation is useful in determining the effectiveness of applying confinement to PPM beams.

The 559H high power TWT was used as the tube model in these calculations. Due to the restrictive nature of the TWTVA program, allowing only one cavity circuit type, it could not be used directly to accurately model the existing 559H. (Up to 11 different cavity types were employed to model this tube using the Hughes' large signal program.) Computed gap voltages from the Hughes' large signal modeling were used as a guide in running Vaughan's TWTVA program. The circuit impedance level was arbitrarily adjusted to give the same order of magnitude gap voltages as those obtained with the more accurate program. Then, using the TWTVA program, three-dimensional beam trajectories were calculated through these gap fields to obtain a qualitative result for the RF defocusing of the beam as a function of the degree of beam confinement. The results of these calculations are given in Figures 18 through 22 for a beam filling factor of 0.55.

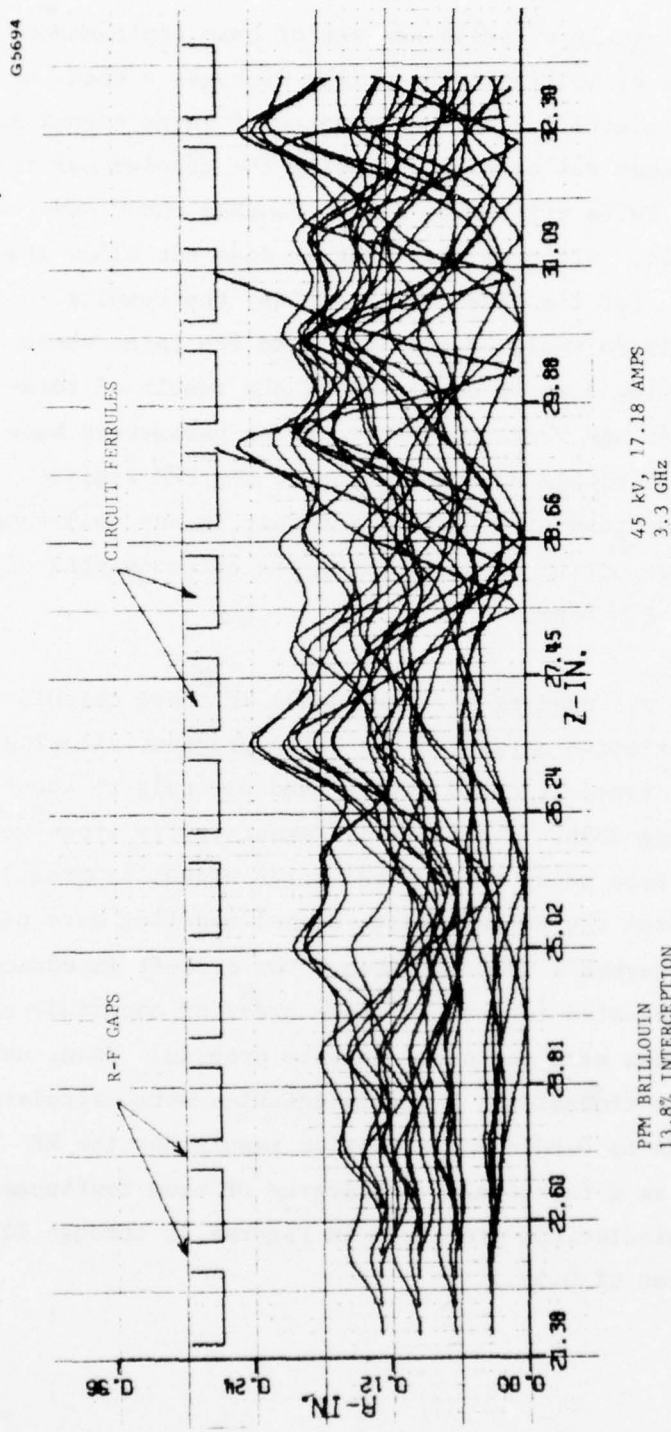
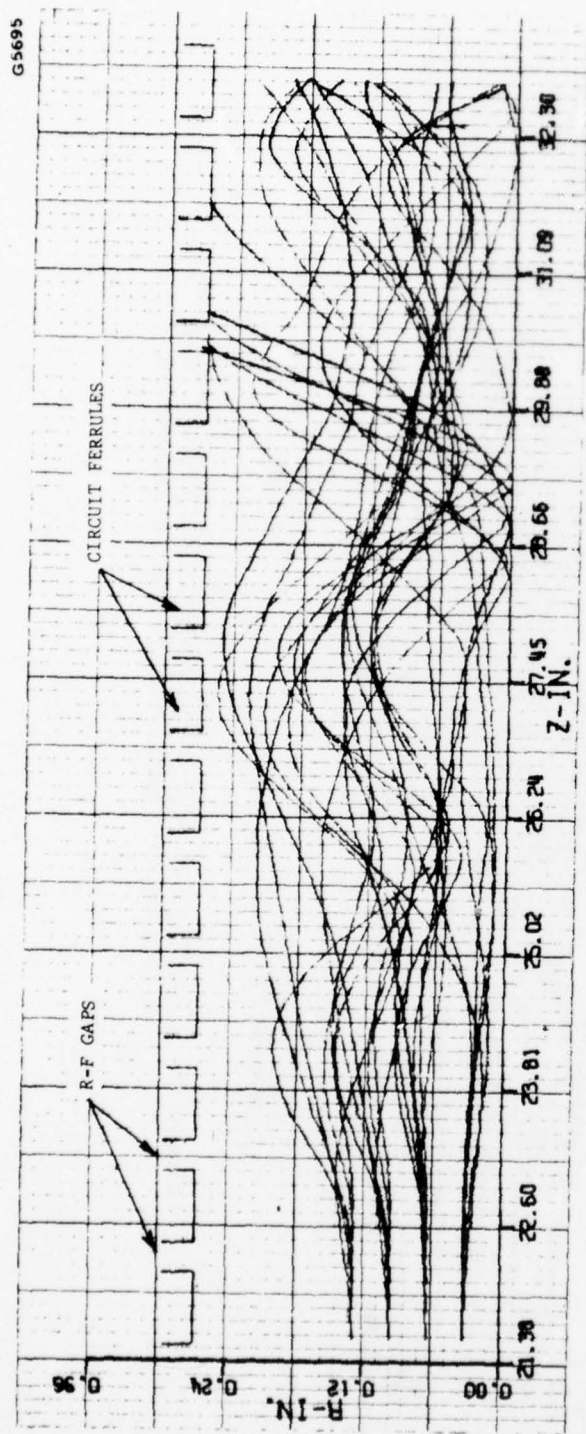


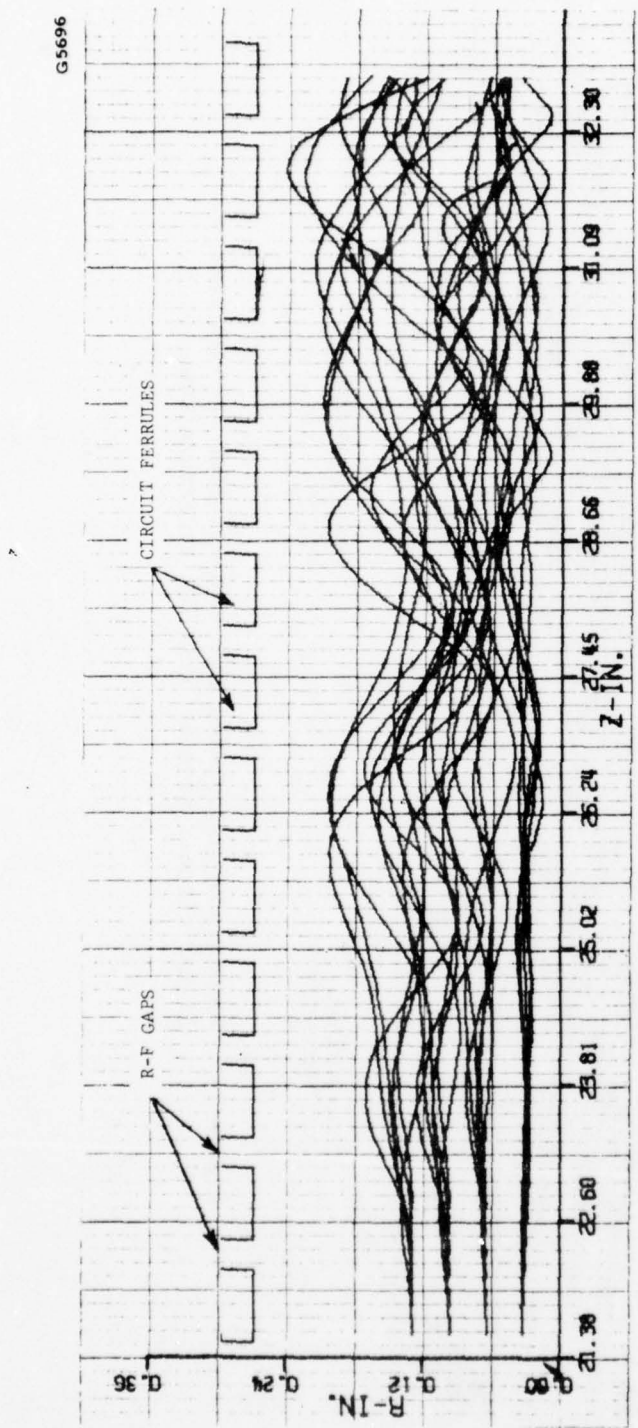
Figure 18 Sampling of calculated beam trajectories through last 12 R-F circuit gaps in 559H TWT at saturation.

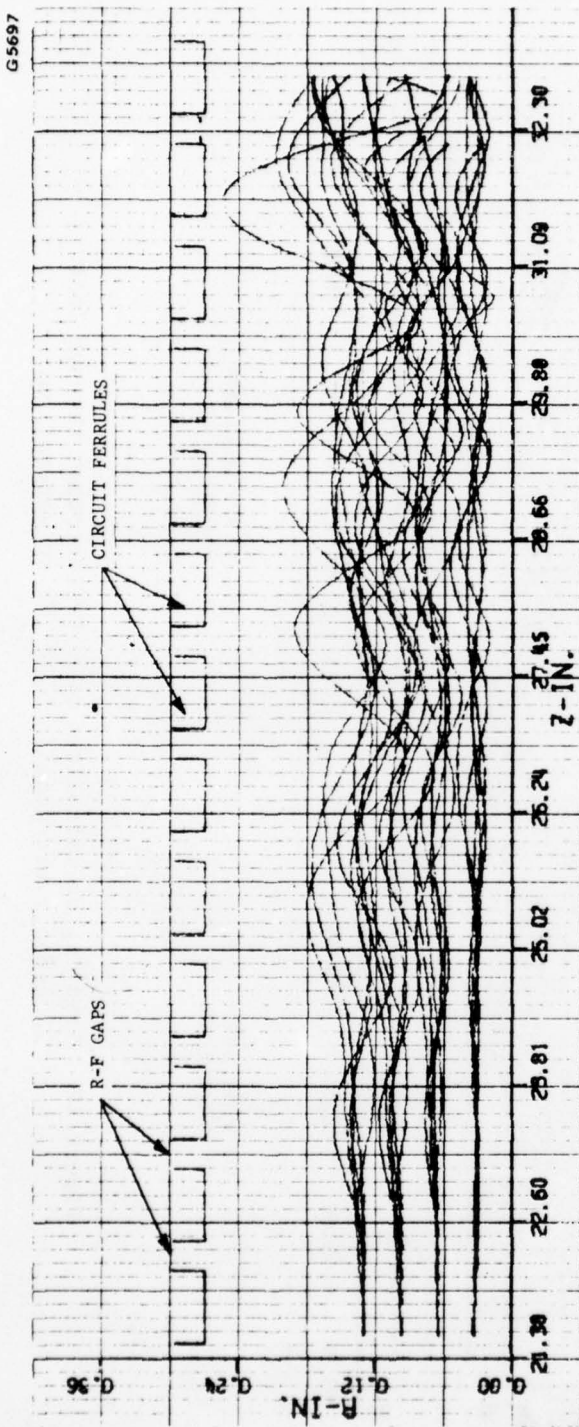


1.0 x BRILLOUIN  
17.6% INTERCEPTION

45 kV, 17.18 AMPS  
3.3 GHz

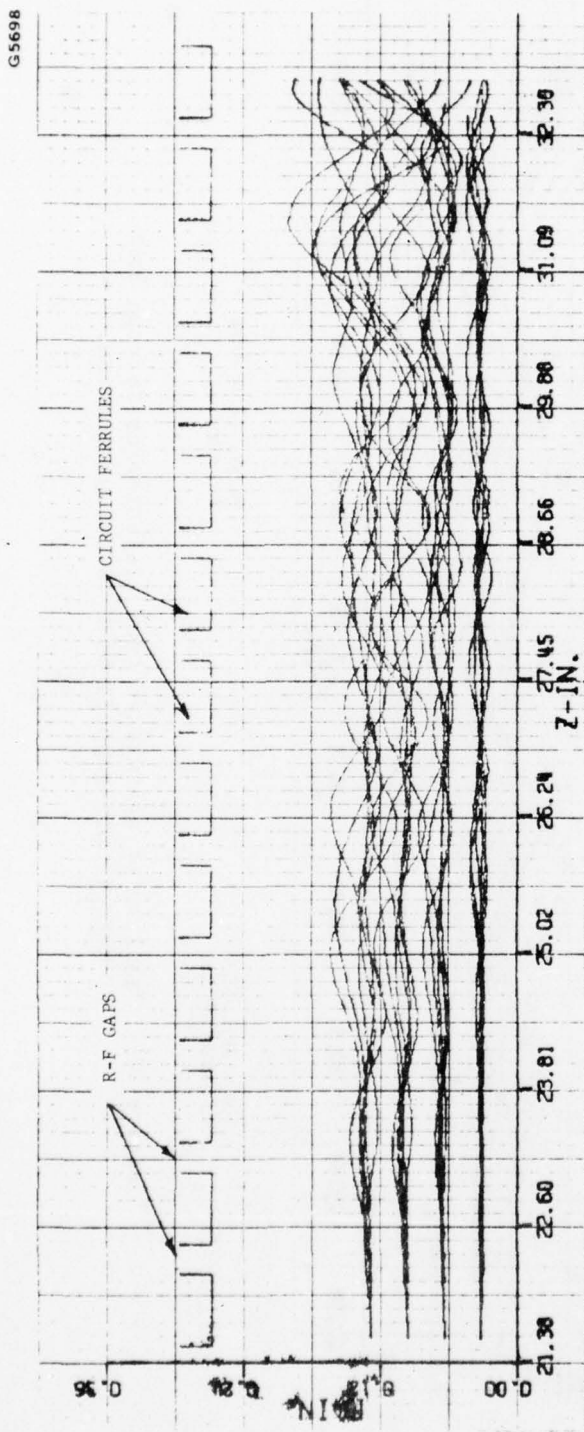
Figure 19 Sampling of calculated beam trajectories through last 12 R-F circuit gaps in 559H TWT at saturation.





4.5 kV, 17.18 AMPS  
3.3 GHz  
1.4 x BRILLOUIN  
NO INTERCEPTION

Figure 21 Sampling of calculated beam trajectories through last 12 R-F circuit gaps in 559H TWT at saturation.



1.6 x BRILLOUIN  
NO INTERCEPTION  
4.5 kV, 17.18 AMPS  
3.3 GHz

Figure 22 Sampling of calculated beam trajectories through last 12 R-F circuit gaps in 559H TWI at saturation.

Figure 18 shows a sampling of trajectories for the case of PPM focusing using an rms value of field equal to the Brillouin field (approximately 600 gauss). Figure 19 shows a similar set of trajectories for the case of a Brillouin value of solenoid focusing field. The nature of the trajectories is similar for the two cases except for the PPM ripple that is superimposed upon the trajectories for the case of periodic field focusing. The calculated interception for these two cases was 13.8% and 17.6%, respectively, whereas the actual tube at saturation typically has around 12% - 15% interception.

Figures 20 through 22 show the effect of beam confinement for 1.2X, 1.4X and 1.6X Brillouin focusing field. It is seen that considerable improvement in the confinement of individual trajectories is obtained with as little as 1.2X Brillouin field. Thus, one could conclude that even small amounts of confinement would be effective in reducing RF defocusing in PPM focused tubes.

Unfortunately, in most high power tube designs, confining the beam is not as easy as simply adding magnetic field. Unless the magnetic period is reduced as the field is increased the focusing will deteriorate, since the parameter  $\alpha$  increases as the field squared. Also, unless the beam diameter is kept small, the rotational energy of the outer beam electrons may produce a large velocity spread across the beam as confinement is introduced into the focusing. For many high power PPM designs the magnetic field is already as high as it should be for good focusing and more field cannot be added unless a shorter period is used. But the shorter period would require an external focusing structure.

In cases where it is not feasible to increase the focusing field a greater ratio of  $B/B_{Br}$  can be achieved with a lower value of  $B_{Br}$

obtained by reducing the beam permeance, although this necessitates increasing the beam voltage to maintain beam power. Since  $\alpha$  is proportional to  $B^2 L^2 / u_0^2$  it remains constant with design changes in voltage, since both  $L$  and  $u_0$  (for integral focusing) scale linearly with the cavity period.

Whether lowering the permeance in a tube such as the 559H will reduce RF defocusing depends on whether the defocusing is caused by the circuit RF fields or by the RF current in the beam. If the circuit fields are so high as to cause electrons to strike the circuit structure, then reducing the current in the beam would not prevent this, and stronger magnetic field would be required. If the circuit fields are weak compared to the RF space charge forces, then reducing the current while maintaining a fixed B-field would reduce the defocusing effect.

The RF gap voltages in the 559H model were in the 10 - 12 kV range at saturation. TWTVA computer runs were made where these saturation voltages were artificially maintained in the gaps as the permeance of the beam was reduced. These results are presented in Figures 23 through 26. As the permeance was lowered and the focusing field remained constant, the beam was made more confined with the introduction of flux into the cathode. In terms of the  $B/B_{\text{Brillouin}}$  ratio of focusing field it can be noted that the effect upon RF defocusing is very similar to results obtained for the high permeance case where additional confinement was accomplished through the employment of greater values of focusing field. It is clear from the very lowest permeance case that the RF circuit fields are not the principal defocusing forces involved in the 559H beam.

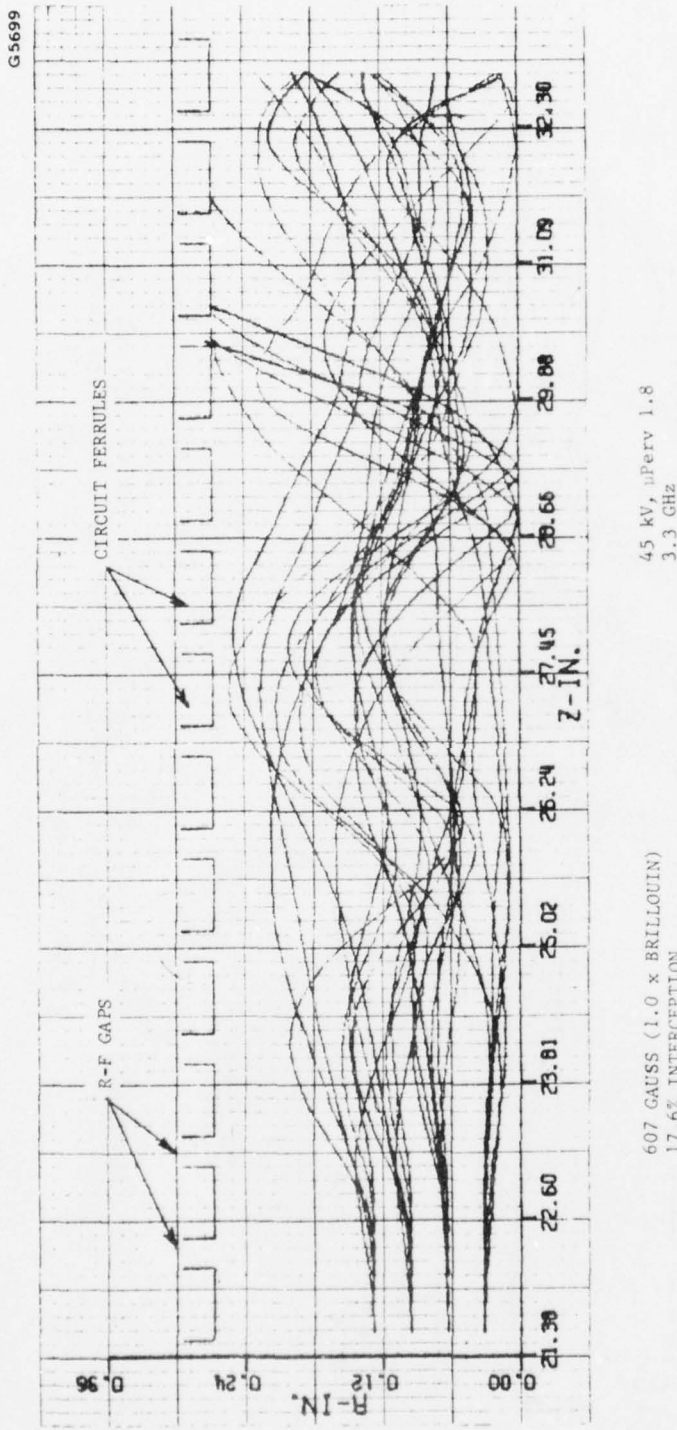
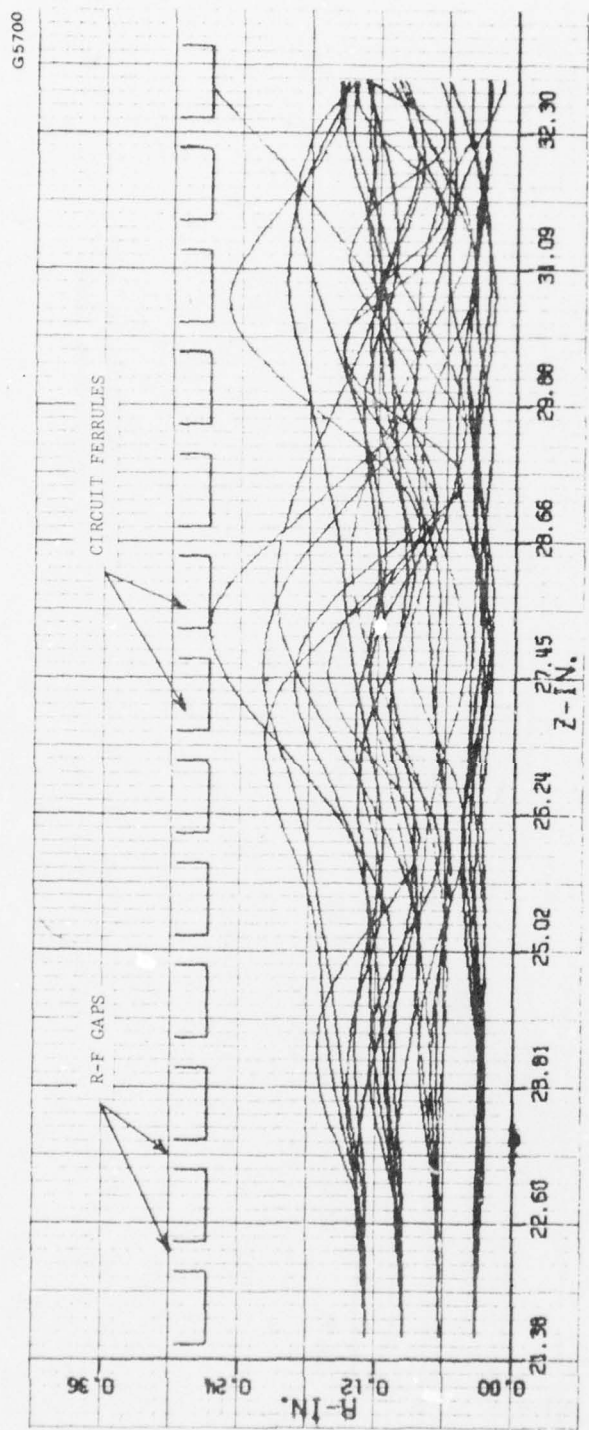


Figure 23 Sampling of calculated beam trajectories through last 12 R-F circuit gaps in 559H TWT for saturation level R-F gap voltages.

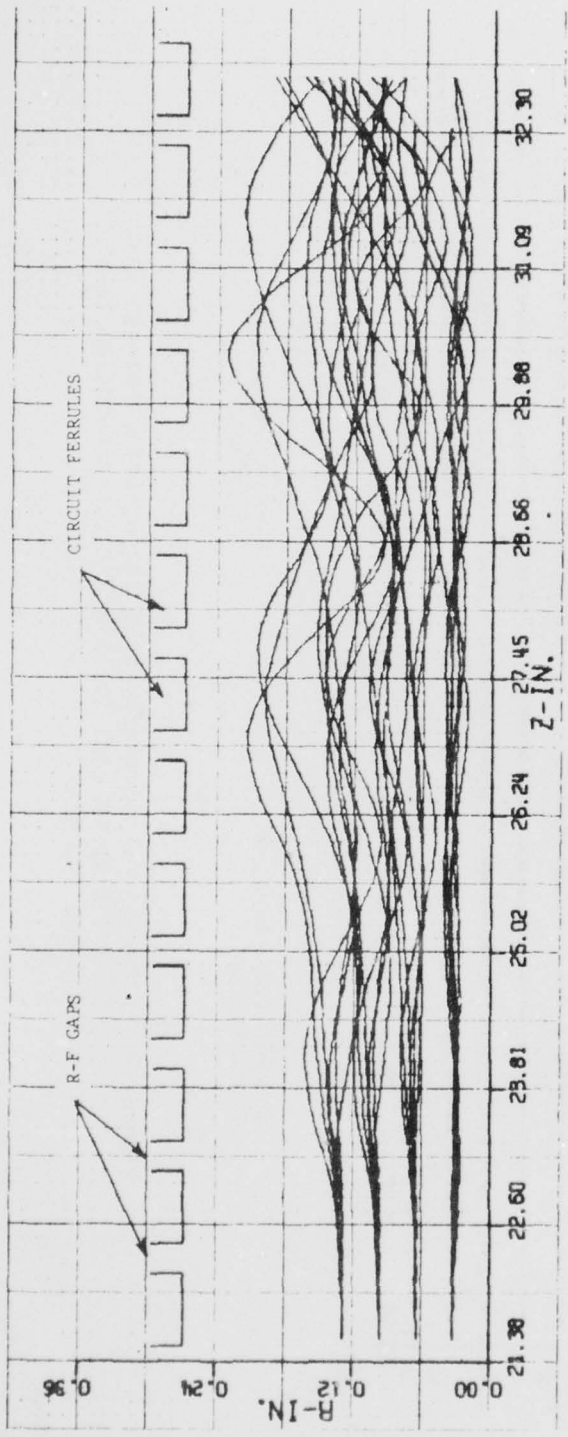


607 GAUSS (1.2 x BRILLOUIN)  
2% INTERCEPTION

45 kV,       $\mu$ Perv 1.25  
3.3 GHz

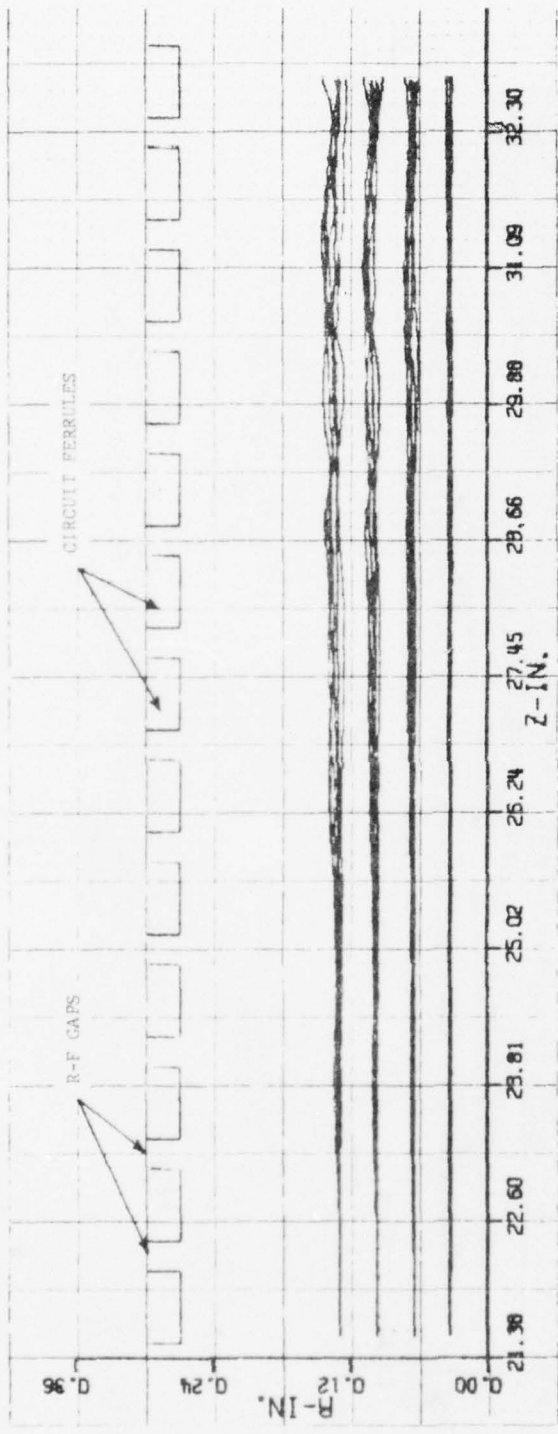
Figure 24 Sampling of calculated beam trajectories through last 12 R-F circuit gaps in 559H TWT for saturation level R-F gap voltages.

G5701



607 GAUSS ( $1.33 \times$  BRILLOUIN)  
0% INTERCEPTION  
45 KV,  $\mu$ Perv 1.0  
3.3 GHz

Figure 25 Sampling of calculated beam trajectories through last 12 R-F circuit gaps in 559H TWT for saturation level R-F gap voltages.



607 GAUSS (3.1 x BRILLOUIN)  
0% INTERCEPTION

45 kV,  $\mu_{\text{Perv}}$  0.18  
3.3 GHz

Figure 26 Sampling of calculated beam trajectories through last 12 R-F circuit gaps in 559H TWT for saturation level R-F gap voltages.

It can also be shown analytically for the 559H tube that with RF gap voltages in the range 10 - 12 kV the radial gap field forces are relatively minor in comparison to the space charge defocusing forces in the high perveance beam. Figure 27 shows the radial and axial field strength for the 559H standard gap. For 10 kV of RF voltage the peak radial field strength at  $b/a = 0.5$  is of the order of 200,000 volts/meter. The DC radial space charge field from a cylindrical beam is

$$E_r = \frac{60 I_0}{r \cdot u_0/c} \quad (27)$$

which, for the 559H beam, is of the order of 400,000 volts/meter. With RF modulation on the beam a steady force field of as much as several times this value may be experienced by the beam edge electrons, whereas the radial components of the gap field are only experienced by the electrons periodically as they travel along the circuit, and then not always at a constant phase.

Thus, in cases where the circuit impedance is low enough for the gap field forces to be negligible in comparison to the space charge forces,  $B/B_{Br}$  becomes a meaningful parameter for characterizing the beam's resistance to RF defocusing. It will also depend upon the level of modulation actually produced in the beam at saturation. In the present TWTVA program there is no measure of the actual RF bunching taking place during any of the final 3-dimensional trajectory calculations. In general, the lower perveance beams will acquire a greater depth of modulation than the high perveance beams because of the lower longitudinal space charge forces.

G5703

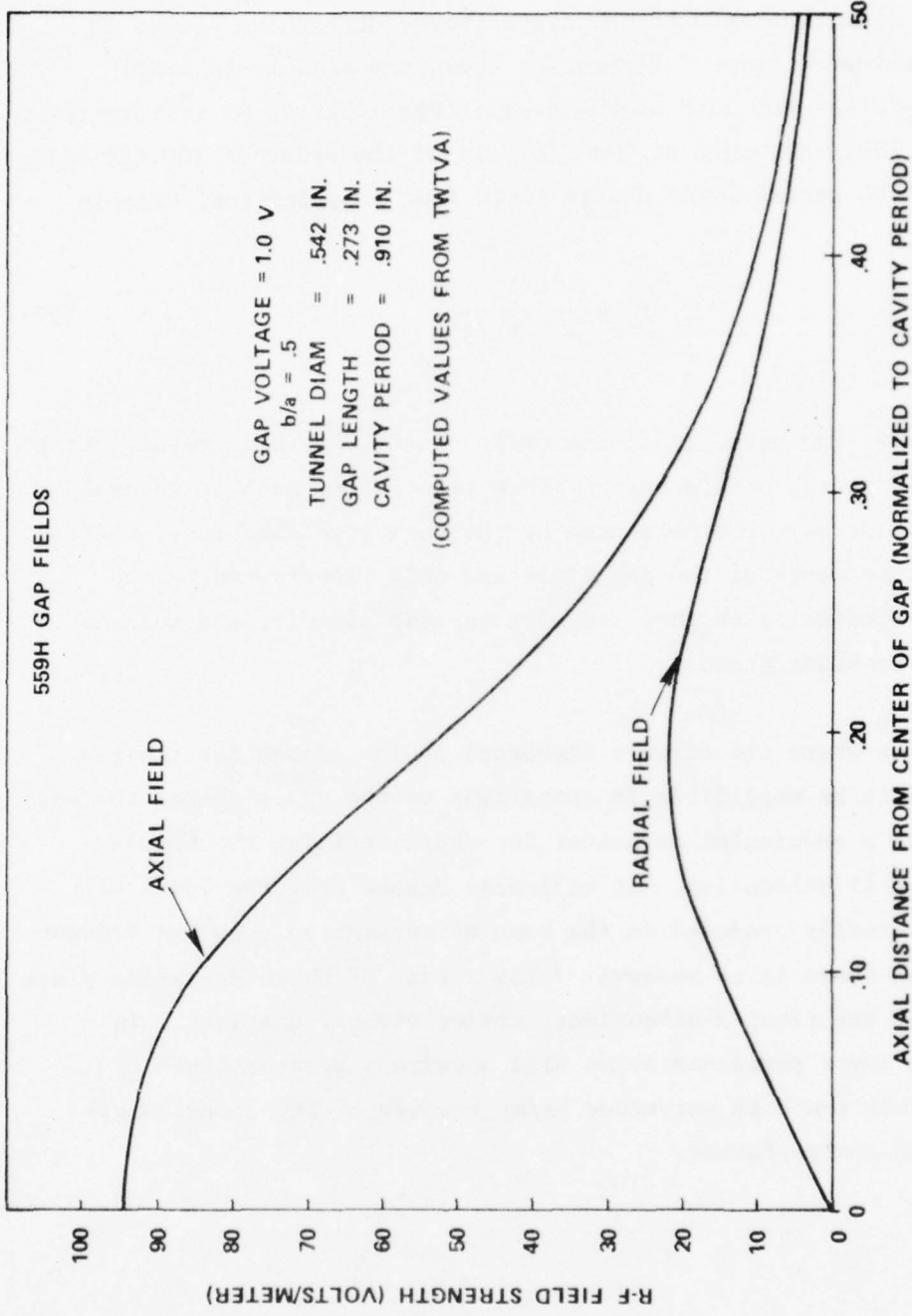


Figure 27 Radial and axial gap fields in the 559H coupled cavity circuit at  $b/a = .5$ .

To design for minimum RF defocusing the maximum focusing field should be used consistent with a good quality of PPM focusing. The beam pervance should then be chosen to be compatible with minimizing the RF defocusing while still giving adequate RF performance and meeting system voltage requirements.

An interesting relationship that can be used as a guide to the maximum focusing field to use in a PPM structure comes from Equation (19). Rewriting this expression, which is actually an identity based on the definition of  $\alpha$ , gives

$$\frac{B_{\text{kgauss}}}{f_{\text{GHz}}} = \frac{\sqrt{\alpha}}{1.4 \left( \frac{\beta_e \ell_c}{\pi} \right)} \cdot \frac{2 \ell_c}{L} \quad (28)$$

For the operating parameters assumed throughout this report of  $\beta_e \ell_c / \pi = 1.3$  typically at midband frequencies,  $\alpha = 0.15$  for 5% or less PPM beam ripple, and for integral pole piece focusing ( $L = 2 \ell_c$ ) the above expression reduces to

$$B_{\text{gauss}} \approx 213 f_{\text{GHz}} \quad (29)$$

This represents the maximum  $B_{\text{rms}}$  focusing field that can be utilized under the above constraints. The use of larger fields would require either relaxing the parameter  $\alpha$ , operating at smaller values of  $\beta_e \ell_c / \pi$ , or going to an external magnet structure such that half the magnet period could be made less than the RF cavity period. For a coupled cavity circuit, the required diameter of an external magnet structure seriously limits its ability to achieve high axial fields at short periods, even with the use of the rare earth magnets. In such a case, size and total weight become extremely important considerations.

### 3.6 PERVEANCE AS A DESIGN PARAMETER

We have seen throughout much of the technical discussion that beam perveance is a key factor in PPM focusing. This is especially true when confinement of the beam is being considered. In general, all aspects of confining and focusing a PPM beam are eased as the beam perveance is made lower.

Beam perveance also plays a major role in the RF interaction process. The coupling between the circuit and beam waves in a linear beam tube is inversely proportional to the beam impedance. Normally, low impedance beams (high perveance, low voltage) are employed in TWT designs to achieve a strong beam-circuit coupling, and also to keep the voltage low from the standpoint of easing system power supply requirements. However, even though the RF coupling may be high, the effect of space charge forces with higher perveances may actually lower the net interaction between the beam and the circuit.

Since the high power tubes studied during the course of this program all suffered difficulty from the standpoint of applying confined PPM focusing to the existing designs, the effect on tube performance of lowering the perveance was investigated. Computer experiments with the high perveance ( $\mu\text{Perv} = 1.8$ ) 559H tube actually showed improved interaction efficiencies with a lower perveance design.

Although the 559H is nominally a 125 kW tube operating over the frequency range 3.1-3.5 GHz Figure 65 (Appendix B) shows midband power output levels in excess of 160 kW. The computer model was simplified to some extent in order not to complicate later variations of the model when design parameters were varied. Even so, 11 different cavity circuit types were employed in order to model the various circuit tapers used in the 559H for either matching or for efficiency enhancement purposes.

Initial computer runs gave approximately 132 kW of saturated power at band center, short of the measured power output. With a slight increase in voltage the computer value was brought up to 139 kW. However, these calculations were based on a beam diameter obtained from an assumed value of rms focusing field based on a measured peak value of field. When an accurate calculation of the ratio of rms to peak field was made for the 559H focusing geometry it was found that this ratio was actually considerably less than the assumed value. A readjustment of the beam diameter consistent with the true rms focusing field in the tube produced a computed saturated output power of 164.7 kW, which is extremely close to the measured values. The final beam filling factor was 0.55 for the output circuit and 0.50 for the drive sections.

Assuming the RF model to be accurate the tube was redesigned, electrically, to operate at a lower perveance (0.7 rather than the original 1.8  $\mu$ Perveance) but with the same DC beam power of approximately 750 kW. This required an operating voltage of around 65 kV. A somewhat smaller beam hole and  $\gamma_a$  were used in the modified design, consistent with the lower perveance beam. The tunnel diameter was reduced from an original 0.542 inches in the input sections and 0.596 inches in the output section to 0.482 inches throughout. The basic cavity period was increased from 0.910 to 1.16 inches for operation at 65 kV and 11.54 amps. The same beam filling factor,  $b/a = 0.55$ , was assumed and essentially the same Brillouin value of focusing field was required (the new design being slightly lower).

The lower perveance design, which would be more compatible for PPM beam confinement and control of RF defocusing, produced over 260 kW of computed saturated power output at band center. The basic conversion efficiency increased from approximately 22% to slightly over 35%.

Realizing that if the beam were to be confined the effective space charge debunching forces would be greater, the performance was also calculated, pessimistically, using the space charge field model appropriate for an infinitely confined beam. Under these conditions the power output dropped to 184.4 kW at band center with 162.9 and 147.7 kW at the lower and upper band edges respectively. Since a PPM beam would never be totally confined, a somewhat higher power output than this could be anticipated in a real design.

Thus, the feasibility of reducing perveance in high power TWT designs without loss of RF performance is indicated. Low perveance beams have less space charge, are more easily focused, the RF defocusing forces are less, and the demodulating or debunching forces are lower such that a greater depth of modulation is achieved for a given circuit interaction impedance. The chief disadvantage of lower perveance is the need for higher operating voltages to achieve the same power output. However, the increased basic efficiency of a low perveance design, combined with the non-linear beam power relationship between perveance and voltage, causes voltage to increase relatively slowly as the perveance is decreased. (For example, if dropping the perveance in half were to result in a design with half again as much efficiency, only a 12 percent increase would be required in the beam voltage.) On the other hand, while it has been demonstrated that a lower perveance design can result in higher efficiencies, the effect of confining a beam increases the effective space charge debunching forces for a given beam geometry, which in turn reduces the gain and efficiency from that which would be achieved without confinement. However, even in a solenoid focused tube, such a penalty in terms of voltage and efficiency would accompany the increase in average power capability achieved through confined flow focusing.

### 3.7 TRAVELING WAVE TUBE THERMAL MODEL

#### 3.7.1 Introduction

A thermal model of the output section of the 559H Traveling Wave Tube (TWT) was prepared to evaluate the effect of axial conduction on temperature distribution in the tube and to perform thermal studies for variations in coolant type and coolant passage geometry.

Conduction and forced convection to the coolant were the only modes of heat transfer considered in the thermal model. Heat losses by free convection external to the TWT and thermal radiation external and internal to the TWT were not considered. Neglecting thermal radiation and free convection results in a conservative analysis in that temperatures of the overall TWT would be slightly higher than actual.

#### 3.7.2 Modeling Technique

Pole pieces and spacers used in the thermal model are shown schematically in Figure 28. Utilizing the fact that the pole pieces are symmetrical about a plane which bisects the kidney hole it was only necessary to model a 180 degree section of the pole pieces. This 180 degree section modeling procedure was also used for the cavity spacers.

All pole pieces were modeled with five distinct slices normal to the long axis of the tube. These continue radially outward to the outside radius of the kidney hole. Outward from this radius the pole pieces are modeled as a single slice normal to the tube axis. Figure 29 is a typical representation of the pole piece modeling described above.

Figures 30 through 34 show a typical nodal model of a circular pole piece. Shown is the radial and circumferential nodal network employed throughout the model.

## BLOCK SCHEMATIC

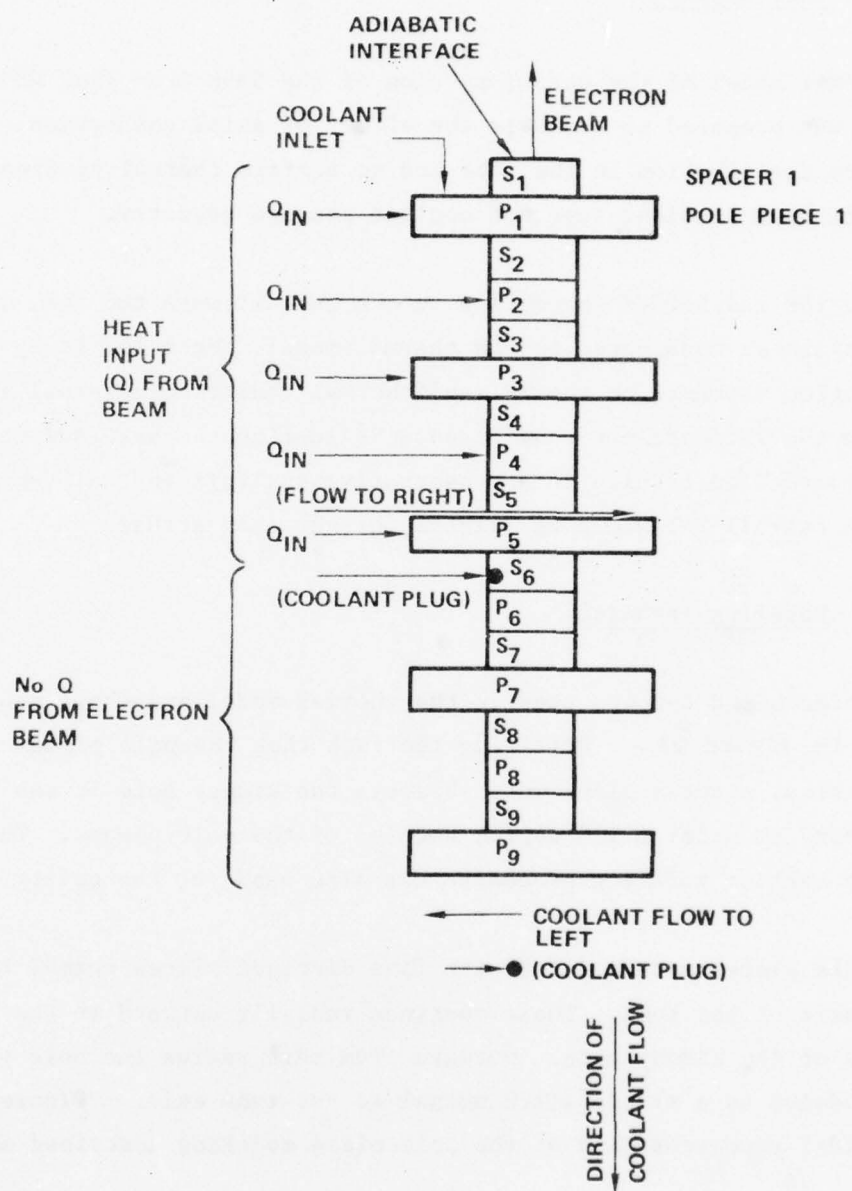


Figure 28 Traveling wave tube thermal model block schematic.

G5705

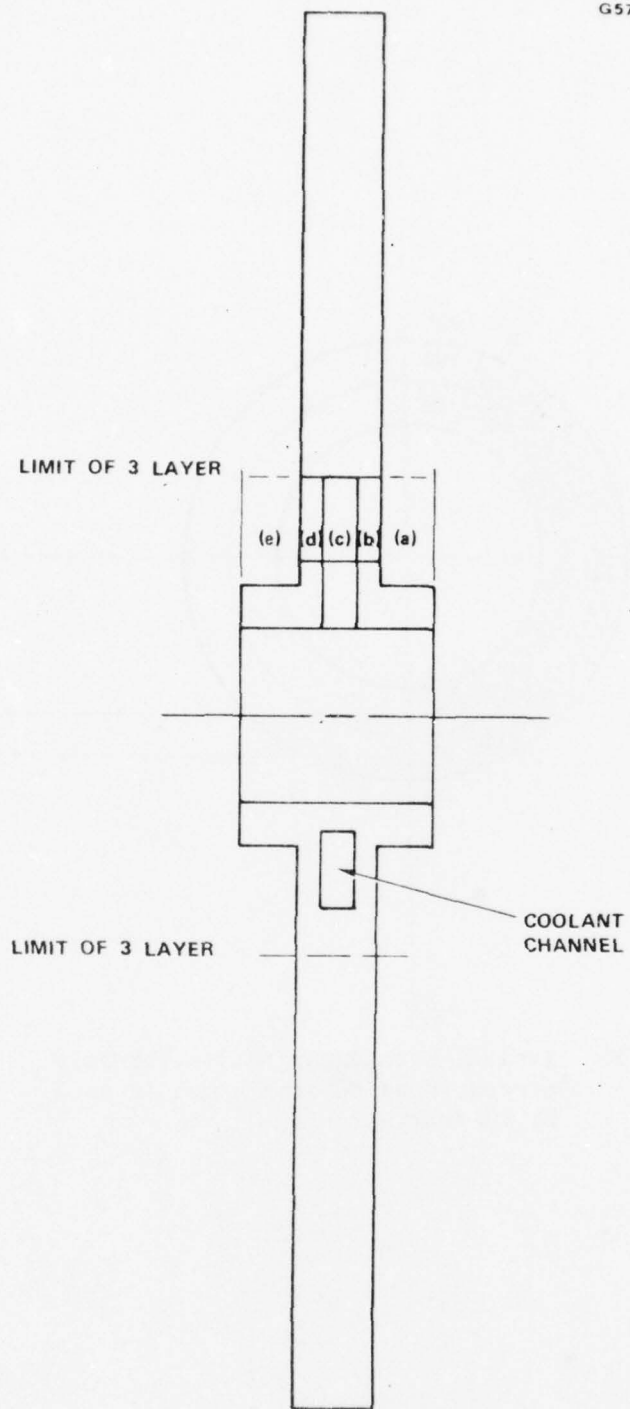


Figure 29 Typical sectioning of pole pieces  
for thermal model.

G5706

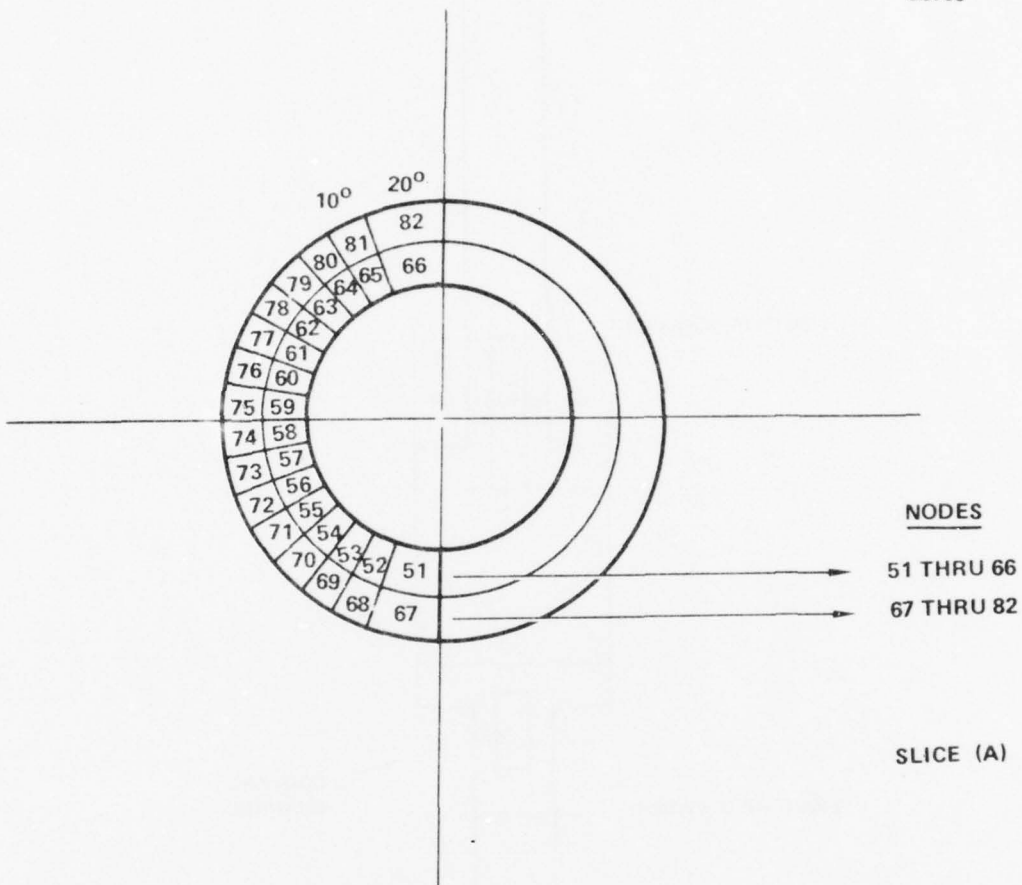


Figure 30 Typical nodal designation for pole pieces (node numbers shown in each block section).

G5707

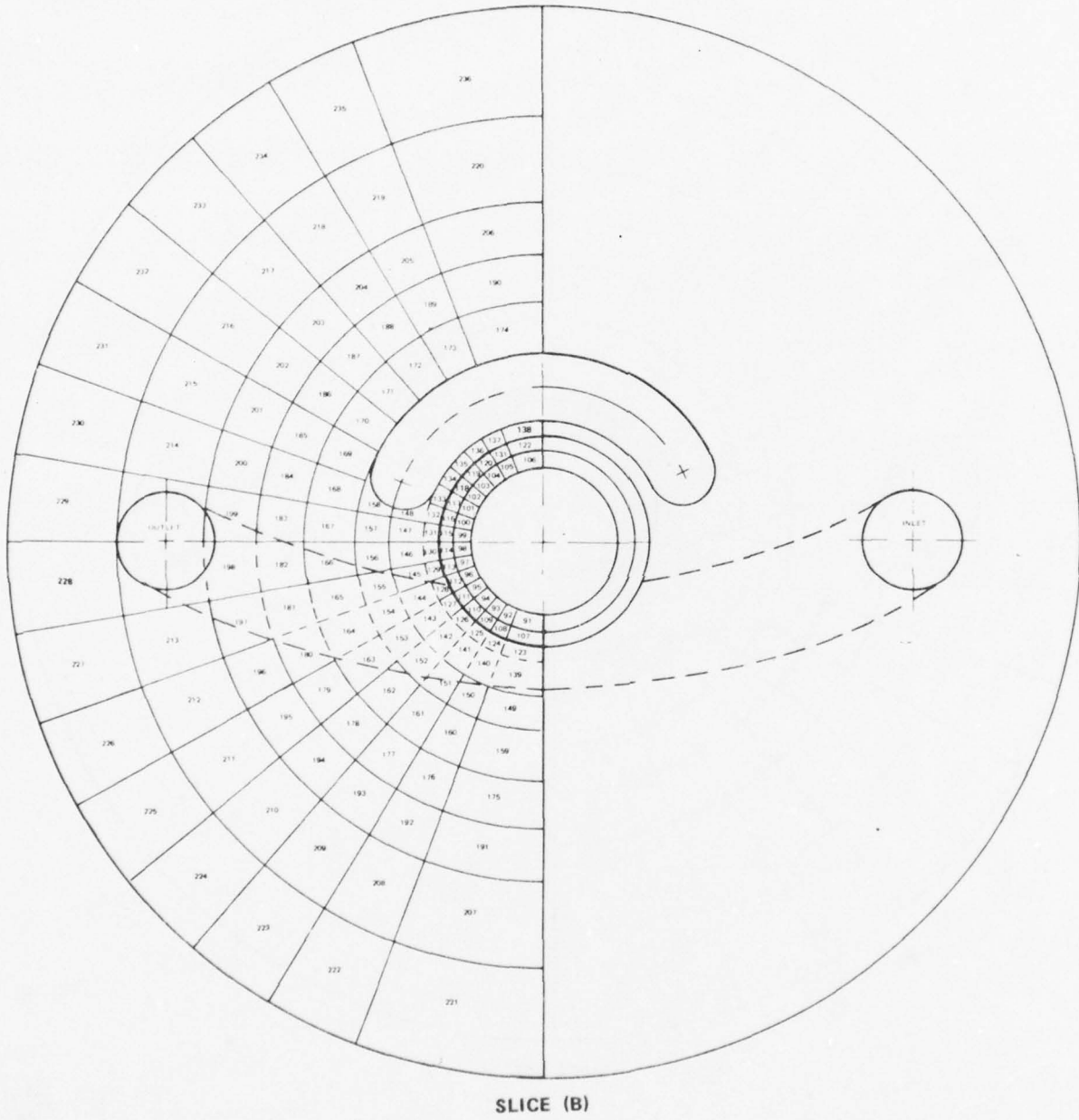


Figure 31 Typical nodal designation for pole pieces (node numbers shown in each block section).

G5708

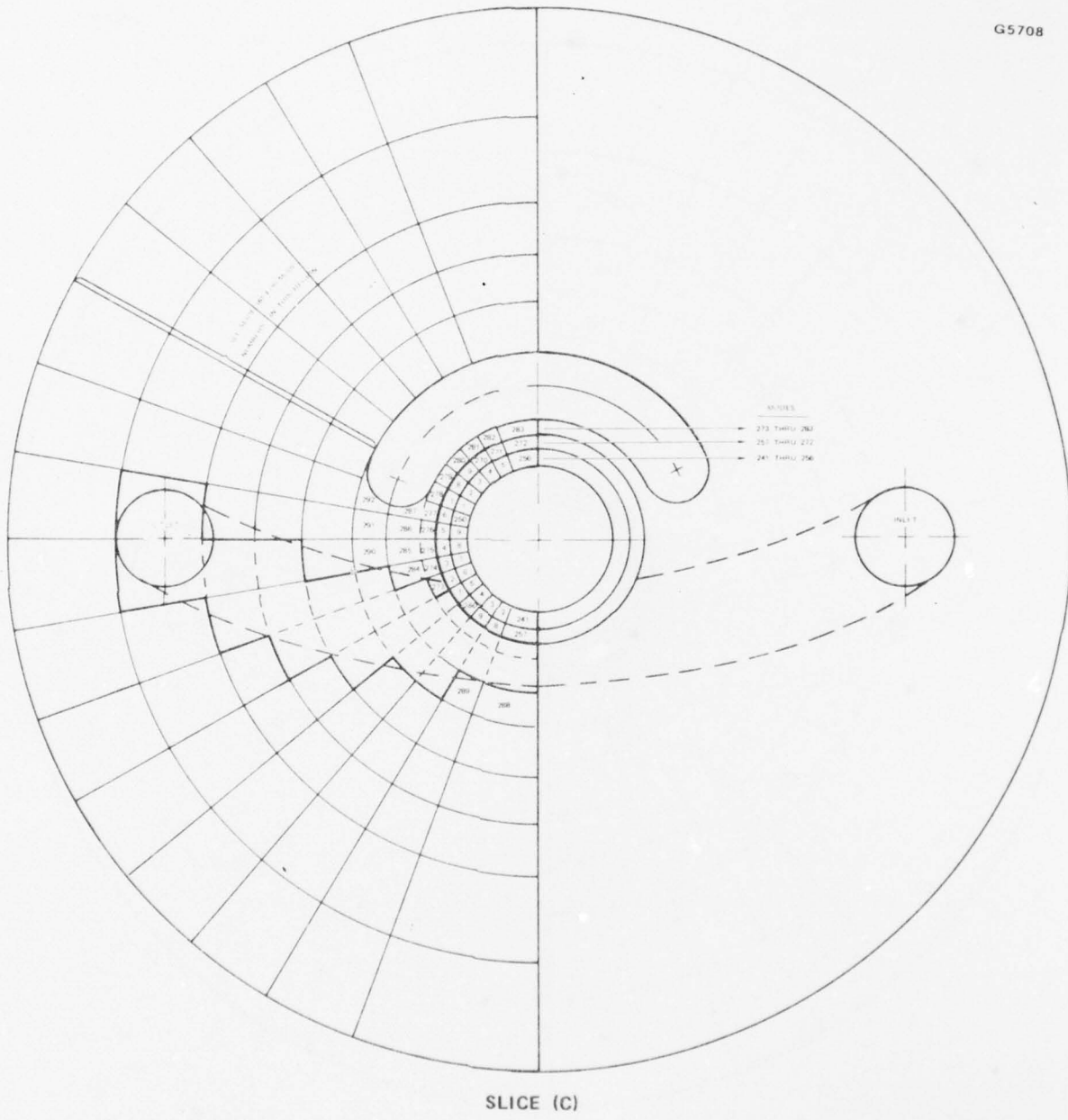
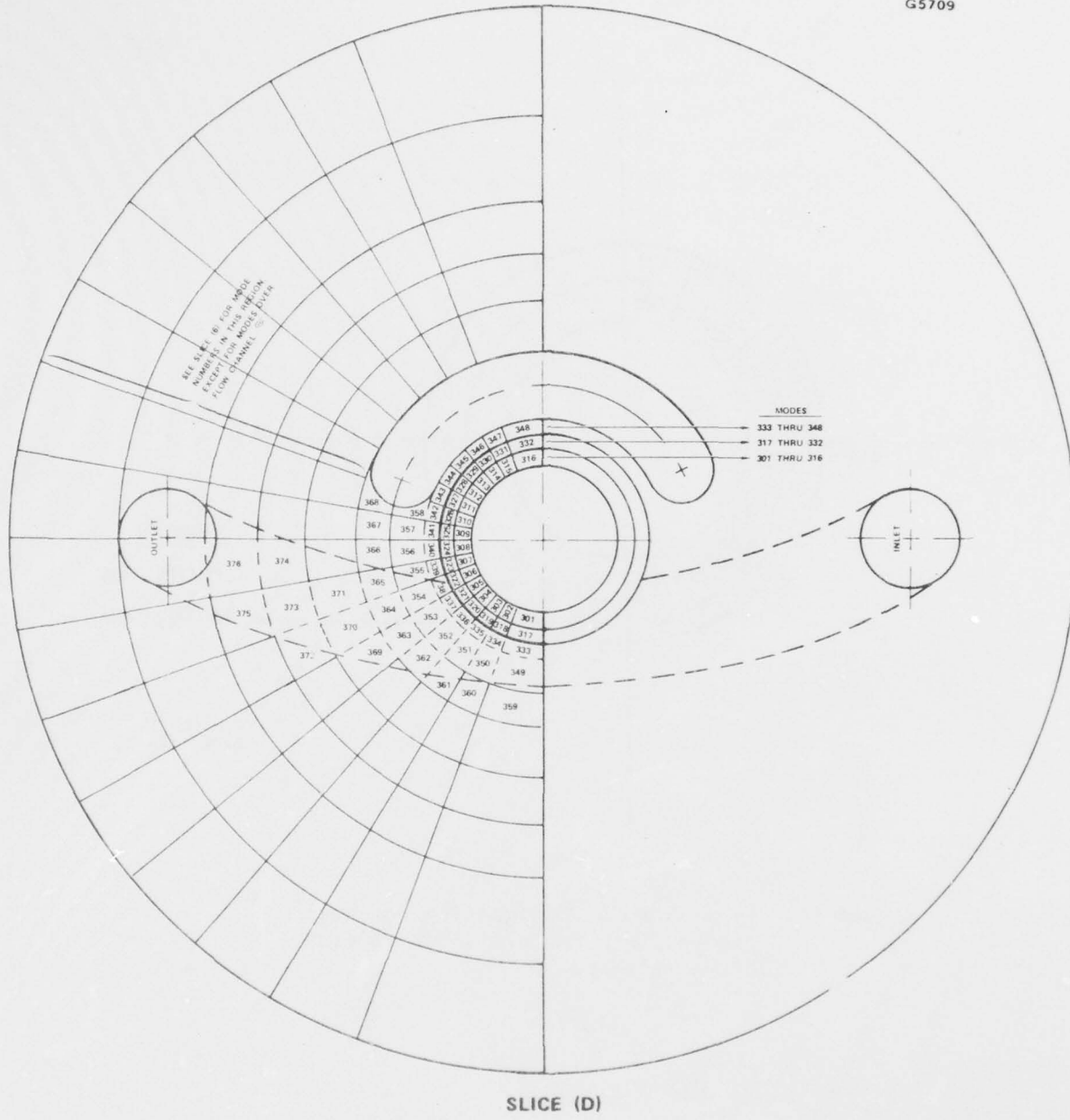


Figure 32 Typical nodal designation for pole pieces (nodal numbers shown in each block section).

G5709



SLICE (D)

Figure 33 Typical nodal designation for pole pieces (node numbers shown in each block section).

G5710

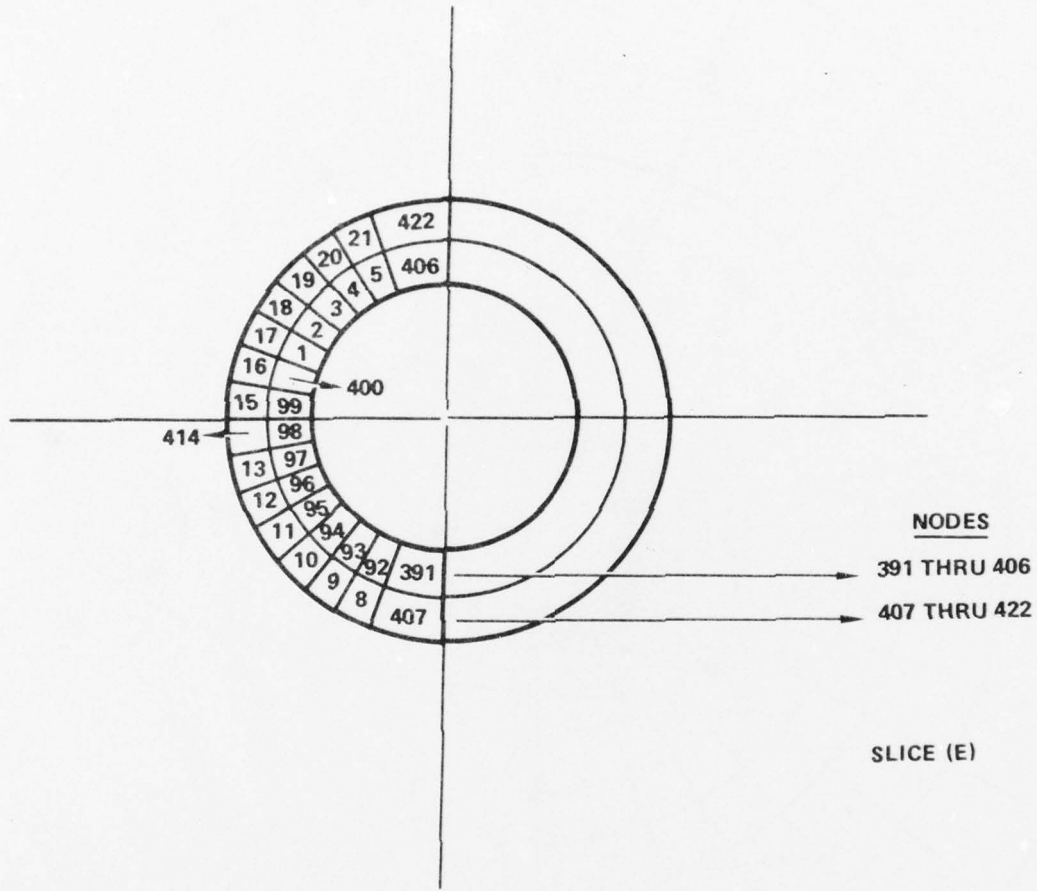


Figure 34 Typical nodal designation for pole pieces (node numbers shown in each block section).

The spacers were modeled using a single radial slice with circumferential node arrangements coinciding with those of the pole pieces.

Blocks of nodes were allocated to each of the spacers and pole pieces to allow for possible later expansion of the thermal model while retaining numerical continuity. Table 1 presents the block node numerical allocations used in the model. Note that all nodes numbered in the 8000 series represent surface nodes of the coolant channels, all those in the 9000 series represent coolant channel fluid nodes. Nodes with other numerical designations represent TWT circuit structure.

Conductors between nodes also were allocated in blocks to allow for possible expansion of the thermal model. Tables 2 and 3 present connector (admittance) lists for thermal paths in the structure and coolant channel systems, respectively. Appendix D presents estimates of the temperature in the area of the node and the subsequent material properties used to calculate the thermal conductances between adjacent nodes. During the computer runs the conductances remain invariant with temperature.

Equations for use in describing turbulent and laminar flow in the TWT coolant channels are presented in Appendix C. Included therein is a general discussion of the effects of channel curvature, asymmetric heating, entrance conditions, and channel roughness on heat transfer.

### 3.7.3 Computer Programs

The 559H thermal model was solved using the CINDA thermal program. CINDA is a digital computer program that is tailored for solving the lumped parameter representation of a physical problem governed by diffusion type equations. It allows the user to choose one of many finite differencing methods unique to transient or steady-state heat transfer

TABLE 1  
NODE NUMBER ALLOCATIONS FOR THERMAL MODEL  
T.W.T. 559 H, H.A.C.

Component	Node Number Allocation for Thermal Model		
	Internal Nodes	Coolant Channel Surface Nodes	Coolant Channel Fluid Nodes
Spacer (S1)	1 → 50	8001 thru 8009	9001
Pole Piece (P1)	51 → 550	8010 thru 8100	9002, 9030 thru 9039
Spacer (S2)	551 → 600	8101 thru 8109	9003
Pole Piece (P2)	601 → 1050	8110 thru 8200	9004, 9040 thru 9049
Spacer (S3)	1051 → 1100	8201 thru 8209	9005
Pole Piece (P3)	1101 → 1600	9210 thru 9300	9006, 9050 thru 9059
Spacer (S4)	1601 → 1650	8301 thru 3309	9007
Pole Piece (P4)	1651 → 2100	8310 thru 8400	9008, 9060 thru 9069
Spacer (S5)	2101 → 2150	8401 thru 8409	9009
Pole Piece (P5)	2151 → 2650	8410 thru 8500	9010, 9070 thru 9079

TABLE 1  
NODE NUMBER ALLOCATIONS FOR THERMAL MODEL  
T.W.T. 559 H, H.A.C. (CONT)

Component	Node Number Allocation for Thermal Model		
	Internal Nodes	Coolant Channel Surface Nodes	Coolant Channel Fluid Nodes
Spacer (S6)	2651 → 2700	8501 thru 8509	9011
Pole Piece (P6)	2701 → 2850	8150 thru 8600	9012, 9080 thru 9089
Spacer (S7)	2851 → 2900	8601 thru 8609	9013
Pole Piece (P7)	2901 → 3050	8610 thru 8700	9014, 9090 thru 9099
Spacer (S8)	3051 → 3100	8701 thru 8709	9015
Pole Piece (P8)	3101 → 3250	8710 thru 8800	9016, 9100 thru 9109
Spacer (S9)	3251 → 3300	8801 thru 8809	9017
Pole Piece (P9)	3301 → 3450	8810 thru 8900	9018, 9110 thru 9119

TABLE 2  
CONNECTOR LIST FOR THERMAL PATHS IN TWT STRUCTURE  
T.W.T. 559 H, H.A.C.

Component	*Connector List, Structural
Spacer (S1)	1 thru 29
Pole Piece (P1)	30 thru 349
Spacer (S2)	350 thru 399
Pole Piece (P2)	400 thru 719
Spacer (S3)	720 thru 799
Pole Piece (P3)	800 thru 1129
Spacer (S4)	1130 thru 1199
Pole Piece (P4)	1200 thru 1599
Spacer (S5)	1600 thru 1699
Pole Piece (P5)	1700 thru 2099
Spacer (S6)	2100 thru 2199
Pole Piece (P6)	2200 thru 2299
Spacer (S7)	2300 thru 2399
Pole Piece (P7)	2400 thru 2499
Spacer (S8)	2500 thru 2599
Pole Piece (P8)	2600 thru 2699
Spacer (S9)	2700 thru 2799
Pole Piece (P9)	2800 thru 2899

\* Includes axial connectors to adjacent component, see Appendix B for additional detail listing of individual connectors

TABLE 3  
CONNECTOR LIST FOR THERMAL PATHS IN TWT COOLANT SYSTEM  
T.W.T. 559 H, H.A.C.

Component	Connector List, Coolant System		
	Conduction, Surface Nodes to Structure Nodes	Convection, Coolant Channel Surface to Fluid Node	Convection Coolant Fluid to Fluid Node
Spacer (S1)	5001 thru 5009	8001 thru 8009	9001
Pole Piece (P1)	5010 thru 5100	8010 thru 8100	9002, 9030 thru 9039
Spacer (S2)	5101 thru 5109	8101 thru 8109	9003
Pole Piece (P2)	5110 thru 5200	8110 thru 8200	9004, 9040 thru 9049
Spacer (S3)	5201 thru 5209	8201 thru 8209	9005
Pole Piece (P3)	5210 thru 5300	8210 thru 8300	9006, 9050 thru 9059
Spacer (S4)	5301 thru 5309	8301 thru 8309	9007
Pole Piece (P4)	5310 thru 5400	8310 thru 8400	9003, 9060 thru 9069
Spacer (S5)	5401 thru 5409	8401 thru 8409	9009
Pole Piece (P5)	5410 thru 5500	8410 thru 8500	9010, 9070 thru 9079
Spacer (S6)	5501 thru 5509	8501 thru 8509	9011
Pole Piece (P6)	5510 thru 5600	8510 thru 8600	9012, 9030 thru 9089
Spacer (S7)	5601 thru 5609	8610 thru 8609	9013
Pole Piece (P7)	5610 thru 5700	8610 thru 8700	9014, 9090 thru 9089

TABLE 3  
CONNECTOR LIST FOR THERMAL PATHS IN TWT COOLANT SYSTEM  
T.W.T. 559 H, H.A.C. (CONT)

Component	Connector List, Coolant System		
	Conduction, Surface Nodes to Structure Nodes	Convection, Coolant Channel Surface to Fluid Node	Convection Coolant Fluid to Fluid Node
Spacer (S8)	5701 thru 5709	8701 thru 8709	9015
Pole Piece (P8)	5710 thru 5800	8710 thru 8800	9016, 9100 thru 9109
Spacer (S9)	5801 thru 5809	8801 thru 8809	9017
Pole Piece (P9)	5810 thru 5900	8810 thru 8900	9018, 9110 thru 9119

analysis of a Resistor - Capacitor (R-C) network representation of a thermal system. The program accommodates large networks upwards of 4,000 nodes. The Hughes Aircraft Co. version of CINDA includes a selection of subroutines from a large CINDA subroutine library and may be used with certain modified Fortran statements as input data. Separate user written Fortran subroutines can be merged with the CINDA program. These attributes permit great flexibility in problem formulation. CINDA is programmed in Fortran IV for execution on the IBM 370 computer.

Once the thermal network is defined within CINDA the execution of the program follows the flowchart shown in Figure 35. All heavy lined boxes in the flowchart represent separate Fortran subroutines or Fortran programming within the CINDA execution block that were written by Hughes. Other subroutines which set initial scalar values, those which read and write information, as well as those decision making boxes in the flowchart are standard on all thermal programs run by the mechanical engineering section at the Electron Dynamics Division of Hughes. The routine (HFLN1) which calculates the heat transfer coefficients in subroutine Variables 1 of CINDA has the same basics as two routines written by Hughes for straight channel flow.

### 3.7.4 Fluid Flow Cooling

The standard straight channel  $\bar{h}$  (film heat transfer) routine needed two changes to be incorporated into the 559H model. Since the numbering of the nodes allowed for later expansion of the model, gaps existed in the node sequence for the fluid to flow channel surface. Arrays were incorporated into the subroutine which allowed the undefined nodes to be skipped in the calculation routines. Appendix C shows the effect curved channels have on heat transfer capabilities compared to straight channels. In this model both straight channels down the long axis of the tube as well as curved channels through the pole pieces exist. In

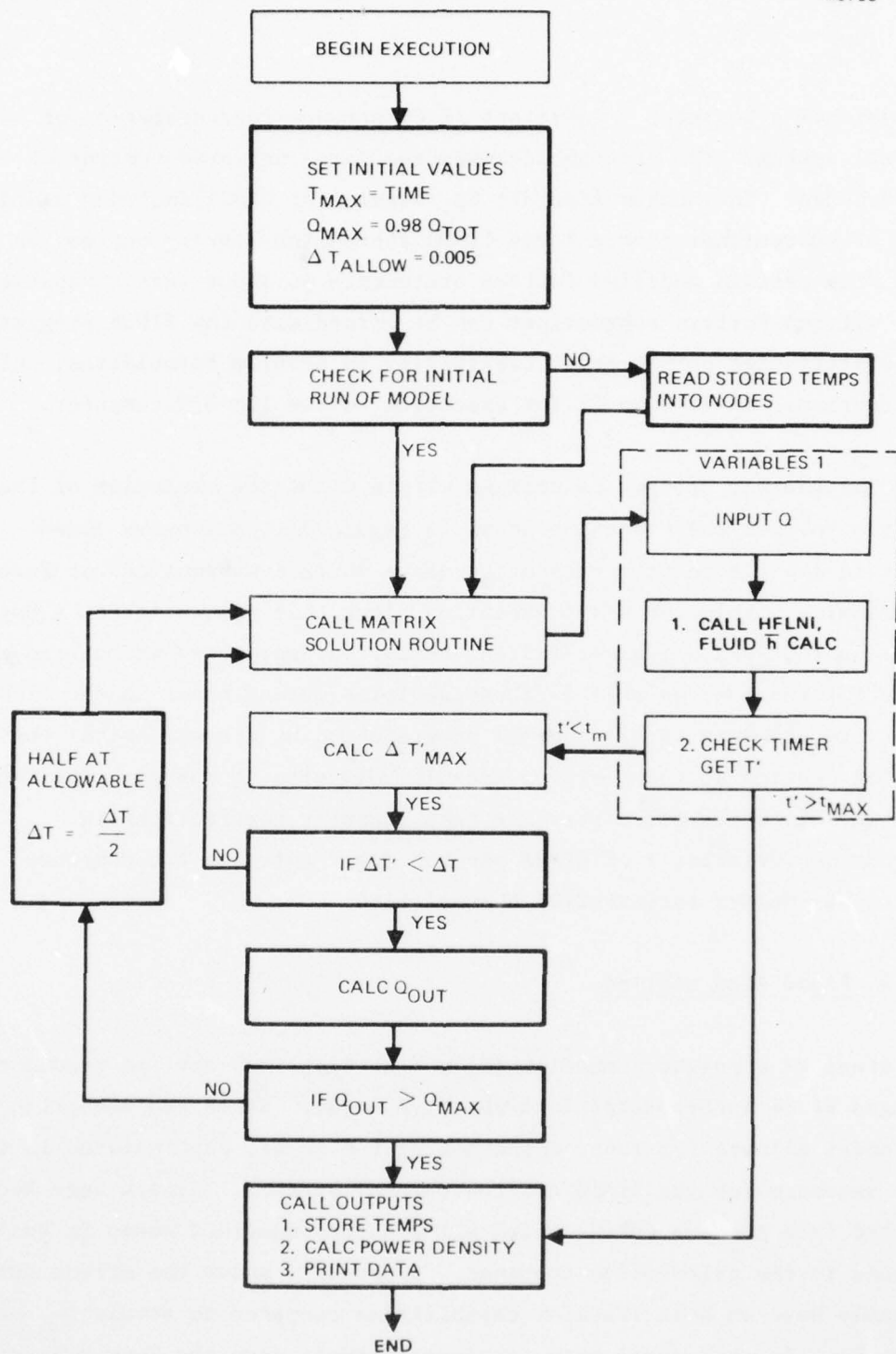


Figure 35 CINDA execution block diagram.

HFLN1 the curved channel heat transfer equations were added to the straight channel equations and a logic decision was incorporated into the subroutine to decide whether a given surface node was in a curved or straight channel.

Since the 559H model represented 180 degrees of a circuit, only 1/2 the total power to the circuit was input. With the entire flowrate of the cooling fluid input, adjustment of the bulk temperature rise of the fluid within the model was necessary. This was accomplished by calculating the amount of power coming from each individual pole piece and then inputting that power into dummy fluid nodes which represent the fluid on the non-existent 180 degrees of the circuit model. The fluid now exhibits a temperature rise indicative of absorbing the amount of power that the entire circuit would absorb.

### 3.7.5 Analytical Results

In arriving at a thermal model for the 559H circuit it is necessary to make certain assumptions with regard to the distribution of the intercepted beam power along the circuit under saturated drive conditions. A typical operating condition was assumed of 4% DC beam interception (most of which is assumed to be intercepted prior to the output section) and approximately 12% total interception under full drive. Allowing for the fact that the RF defocused electrons would, on the average, have lost up to 20% of their original energies the intercepted beam power was taken as 80% of the product of the circuit voltage (44 kV) and the portion of the intercepted current due only to RF defocusing (1.32A) or 46.464 kW peak intercepted power. This power was assumed to be spread over the last five pole piece ferrules with a 10%-20%-20%-25%-25% distribution, the most power being intercepted by the pole pieces closest to the collector. At 5% duty the pole piece intercepted powers are then 232-465-465-581-581 Watts respectively.

The above thermal input powers were used in generating temperature data for a representative condition of operation. No RF heating of the cavity was input. Water Glycol coolant in concentration 60%/40% was input at the collector end of the model with an ambient temperature of 65°C and a flow rate of 4 gallons per minute. Temperatures for representative nodes on each pole piece and spacer are shown in Figures 36 through 53. Figure 54 shows the isothermal profiles around the ferrule on pole piece 1. The temperature distribution on pole piece 1 is also tabulated for an increased flow rate of 8 gallons per minute in Figure 55.

Figure 56 presents an interesting result. Considering that heat is being applied only at the pole piece ferrule, it appears that very little longitudinal heat transfer occurs along the circuit length. This effect is primarily due to the close proximity of the ferrule to the coolant channel. One also notices that a majority of the power is absorbed into the fluid very near the ferrule. This area around the ferrule shows large thermal gradients, as displayed in Figure 54, again primarily due to the proximity of the coolant channel. Figure 55 indicates that only small reductions in the maximum temperature occur by doubling the flow rate. This result is not surprising in that the fluid flowing at 4 gpm is already in turbulent flow and a drastic increase in heat transfer coefficient ( $\bar{h}$ ) is not achievable with 8 gpm flow.

### 3.7.6 Conclusions

The actual energy level and distribution of the intercepted electrons is not known with any accuracy. The thermal model of the 559H with the above assumed thermal input powers gives reasonable temperature rises in each of the various pole pieces and points out the thermal strengths and weaknesses of the design. In this respect the model is useful and

G5712

POWER INPUT = 0 W  
COOLANT  
 $H_2O/GLYCOL$   
FLOW = 4 GPM  
INLET =  $65^{\circ}C$

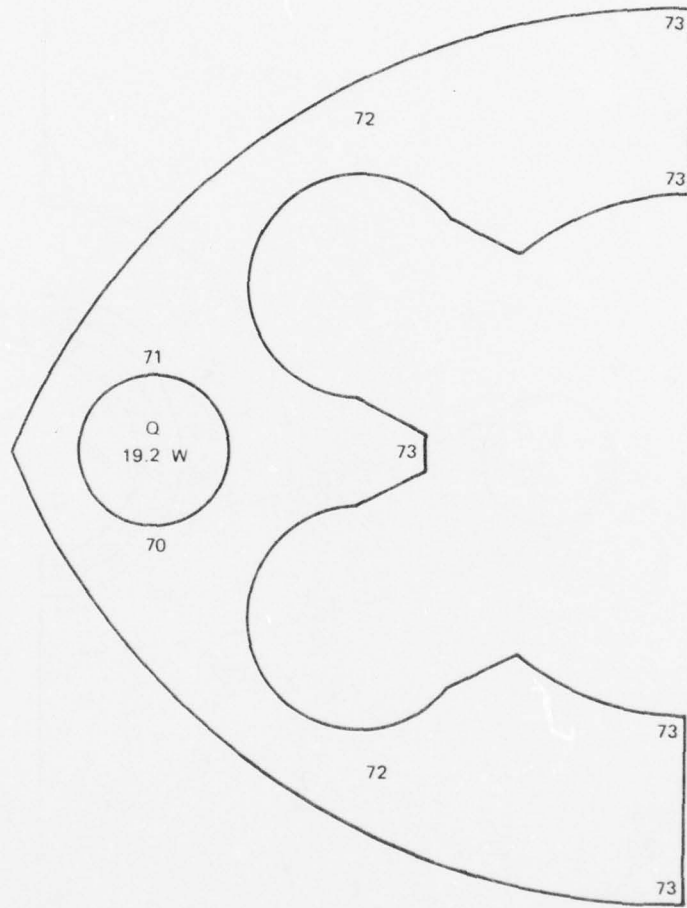


Figure 36 Thermal data spacer I (temperatures in degrees celsius).

G5713

POWER INPUT = 581 W  
COOLANT  
 $H_2O/$ GLYCOL  
FLOW = 4 GPM  
INLET =  $65^{\circ}C$

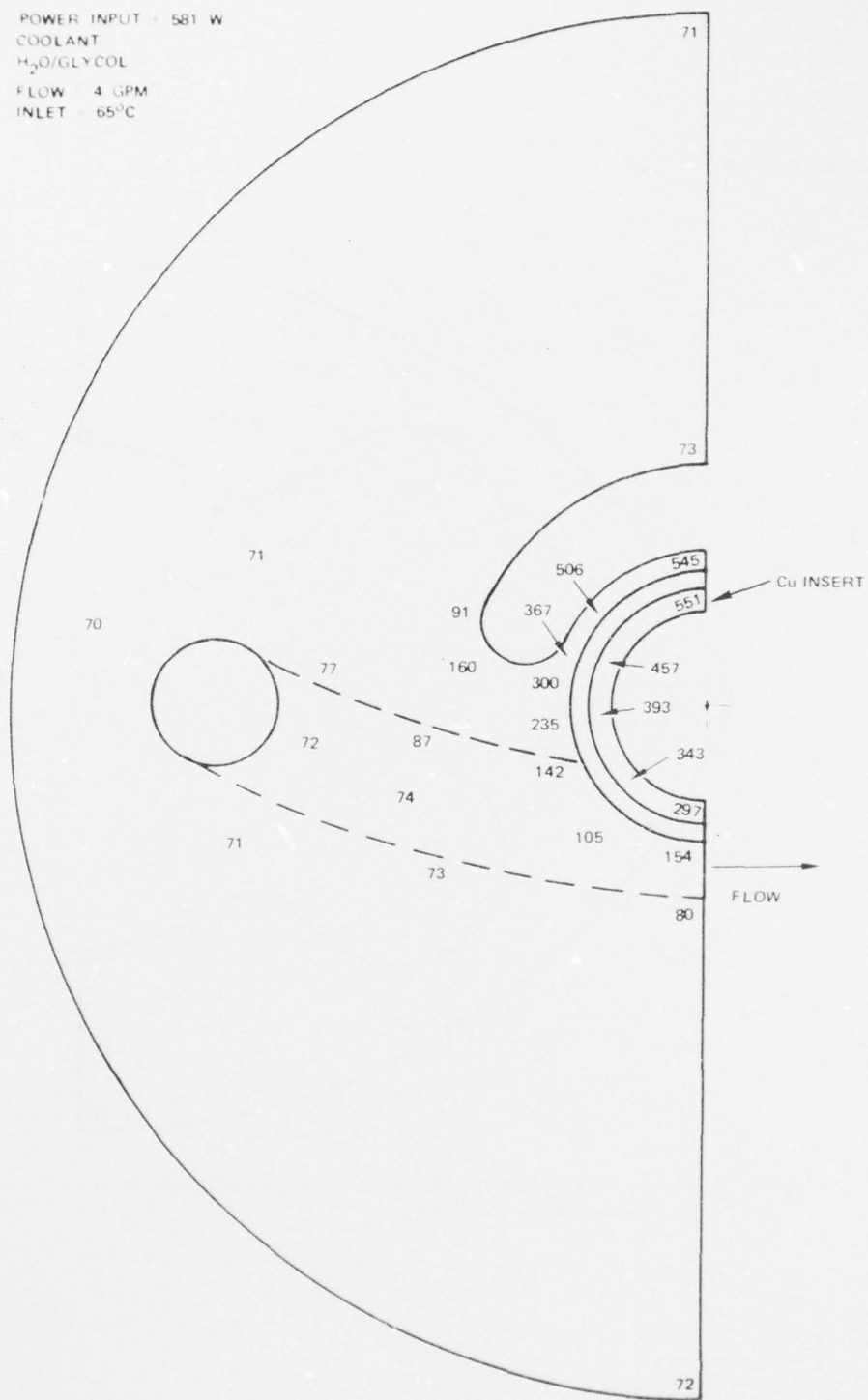
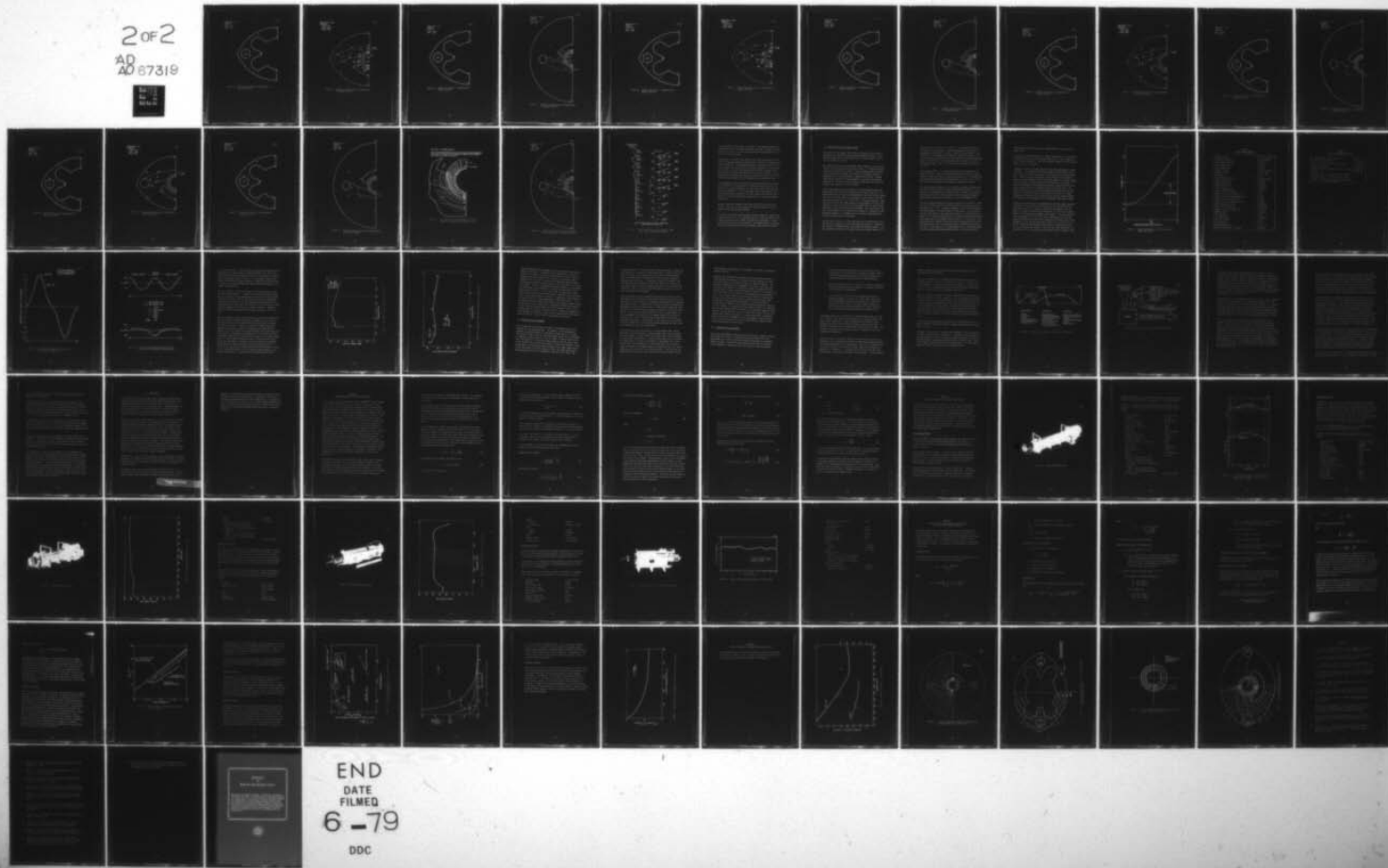


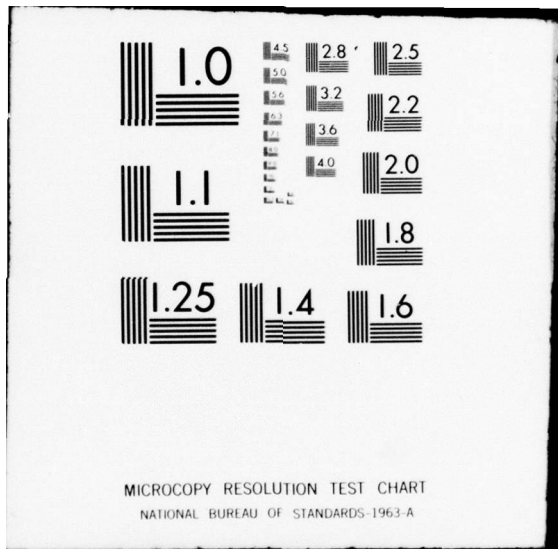
Figure 37 Thermal data pole piece 1 (temperatures in degrees celsius).

AD-A067 319 HUGHES AIRCRAFT CO TORRANCE CALIF ELECTRON DYNAMICS DIV F/G 9/1  
PERMANENT MAGNET STUDY FOR HIGH AVERAGE POWER TWTS. (U)  
FEB 79 W A HARMAN, R S HOLLISTER, J O TILLERY F30602-77-C-0109  
UNCLASSIFIED EDD-W-07407-F RADC-TR-78-288 NL

2 OF 2  
AD 67319  
REF ID: A67319



END  
DATE  
FILED  
6 - 79  
DDC



G5714

POWER INPUT = 0 W

COOLANT

H<sub>2</sub>O/GLYCOL

FLOW = 4 GPM

INLET = 65° C

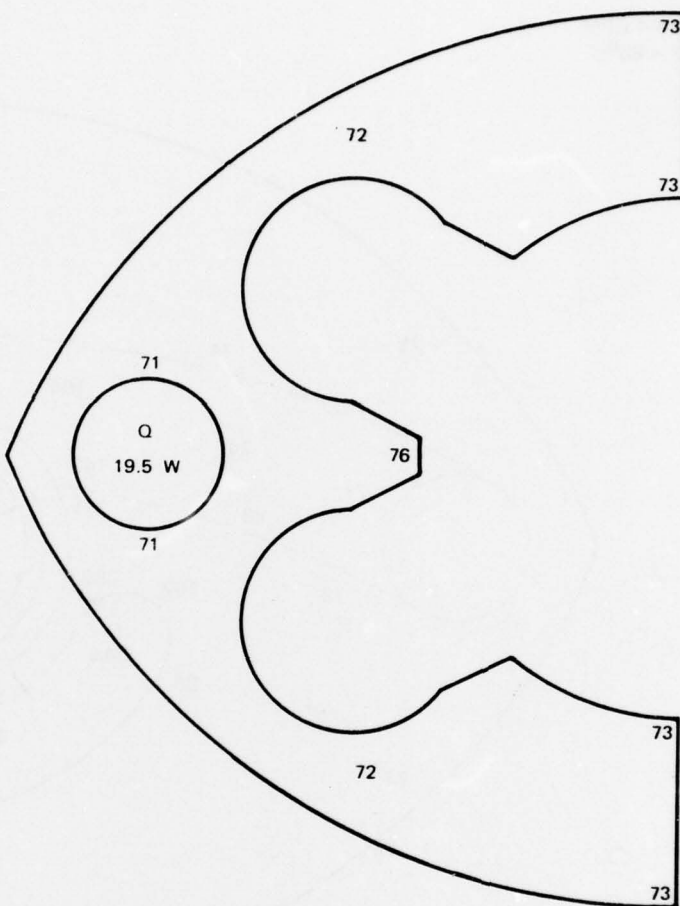


Figure 38 Thermal data spacer 2 (temperatures in degrees celsius).

POWER INPUT = 581 W

COOLANT

H<sub>2</sub>O/GLYCOL

FLOW = 4 GPM

INLET = 65°C

G5715

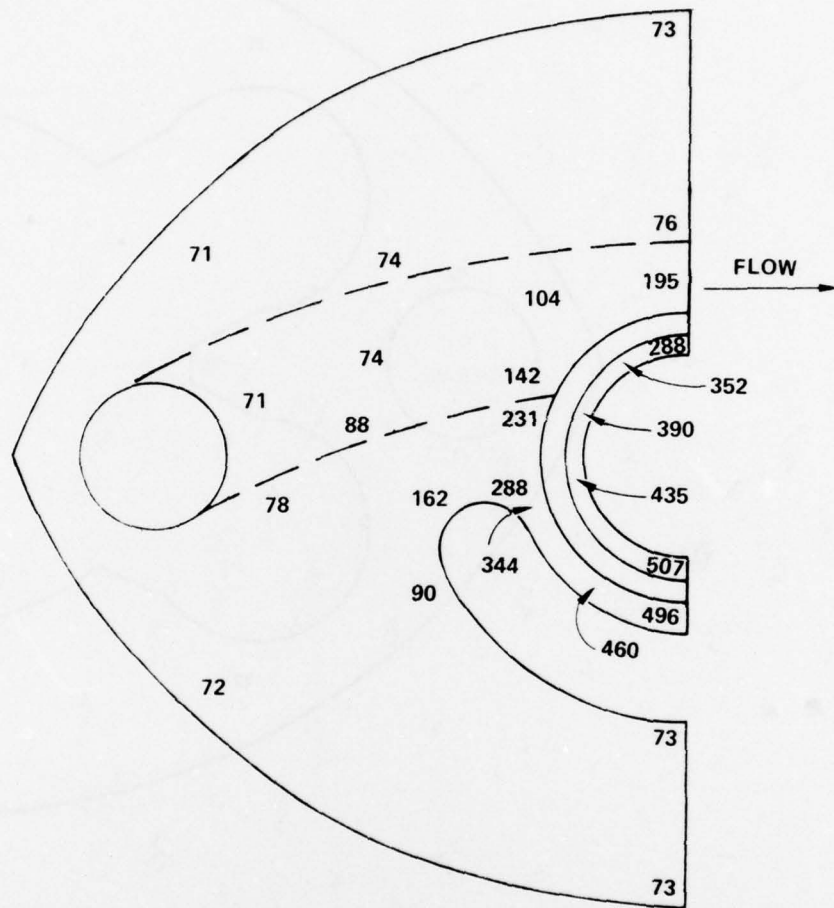


Figure 39 Thermal data pole piece 2 (temperatures in degrees celsius).

G5716

POWER INPUT = 0 W  
COOLANT  
 $H_2O/GLYCOL$   
FLOW = 4 GPM  
INLET = 65°C

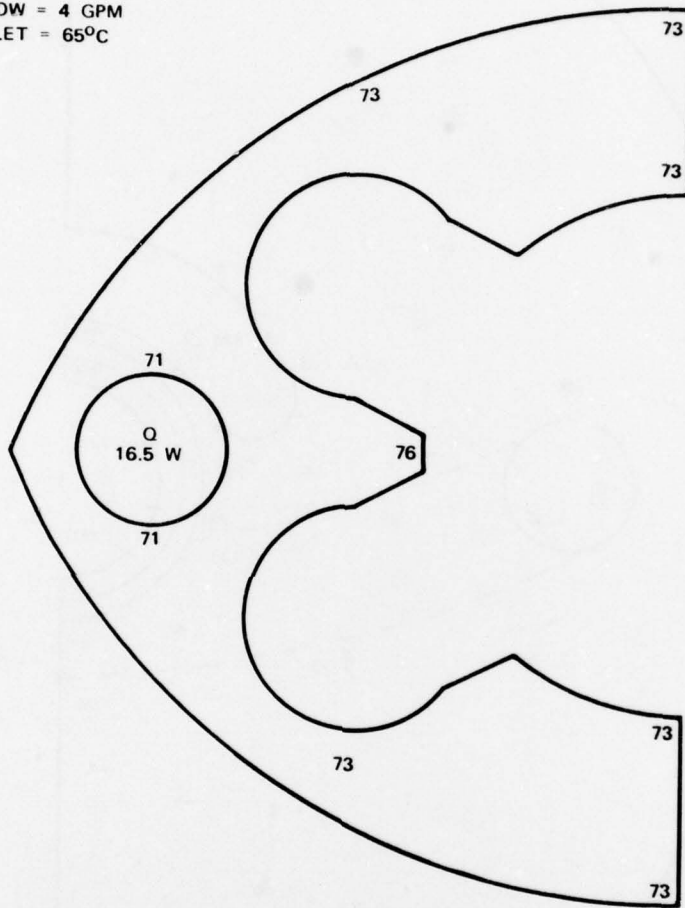


Figure 40 Thermal data spacer 3 (temperatures in degrees celsius).

G5717

POWER INPUT = 464 W  
COOLANT  
 $H_2O/GLYCOL$   
FLOW = 4 GPM  
INLET =  $65^\circ C$

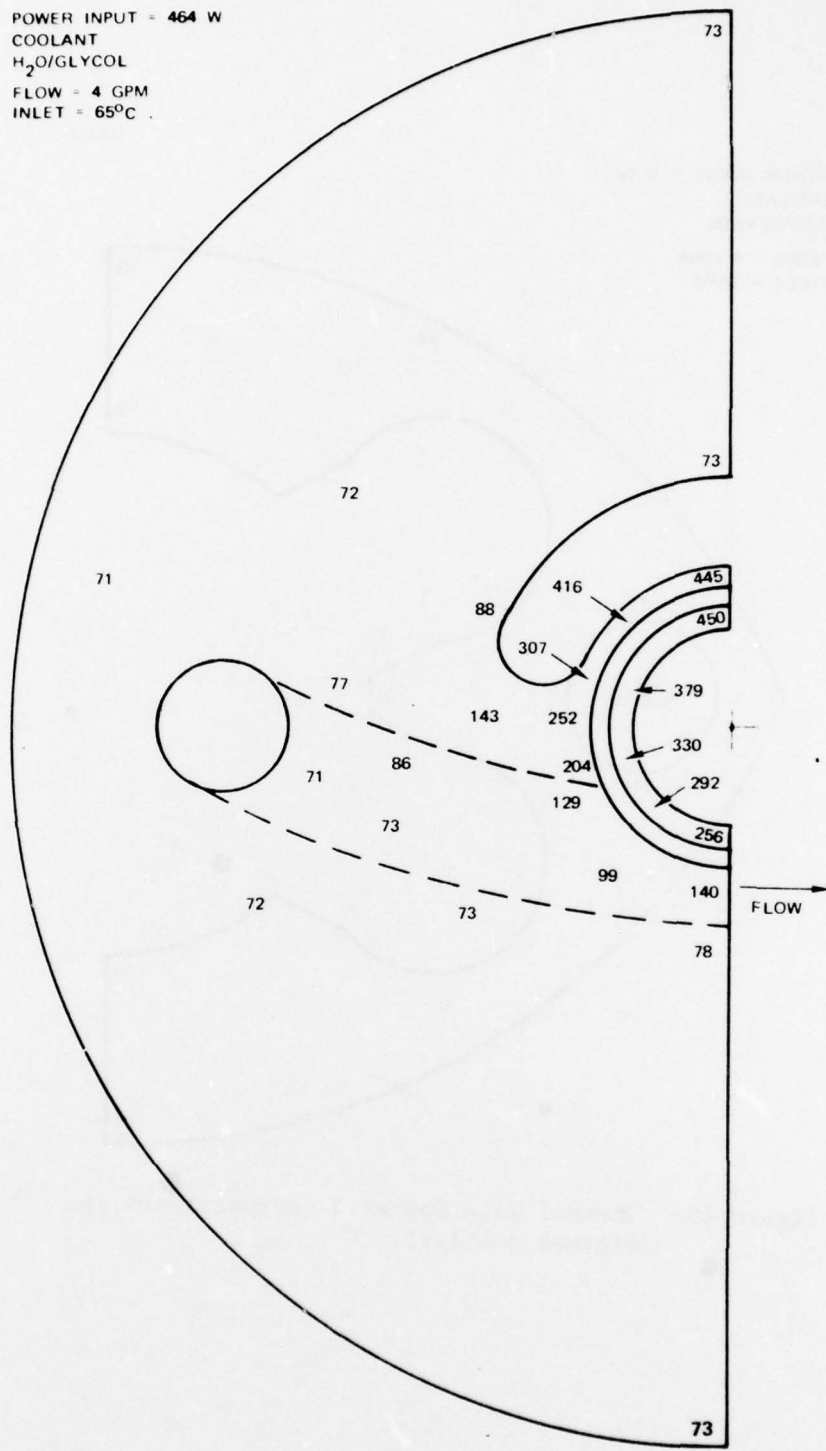


Figure 41 Thermal data pole piece 3 (temperatures in degrees celsius).

POWER INPUT = 0 W  
COOLANT  
 $H_2O$ /GLYCOL  
FLOW = 4 GPM  
INLET = 65°C

G5718

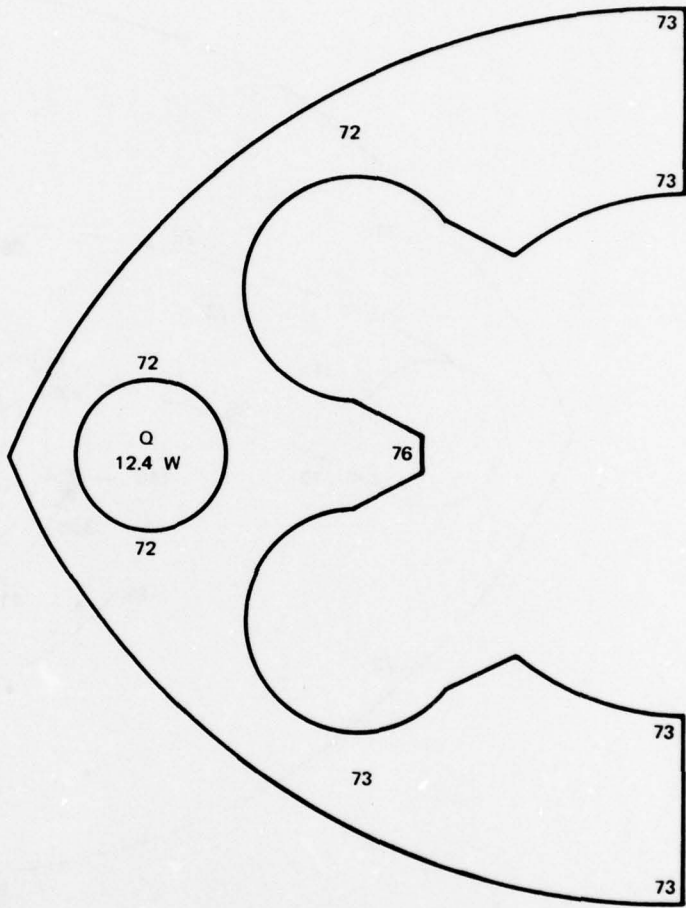


Figure 42 Thermal data spacer 4 (temperatures in degrees celsius).

POWER INPUT = 464 W

COOLANT

H<sub>2</sub>O/GLYCOL

FLOW = 4 GPM

INLET = 65°C

G5719

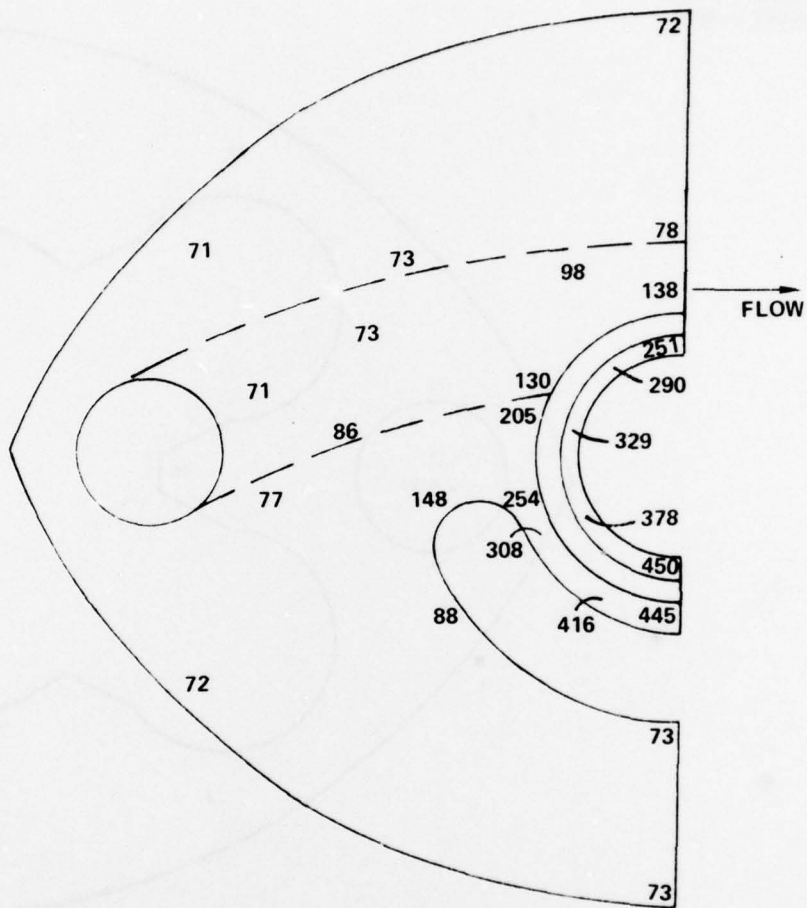


Figure 43 Thermal data pole piece 4 (temperatures in degrees celsius).

G5770

POWER INPUT = 0W  
COOLANT  
 $H_2O/GLYCOL$   
FLOW = 4 GPM  
INLET =  $65^{\circ}C$

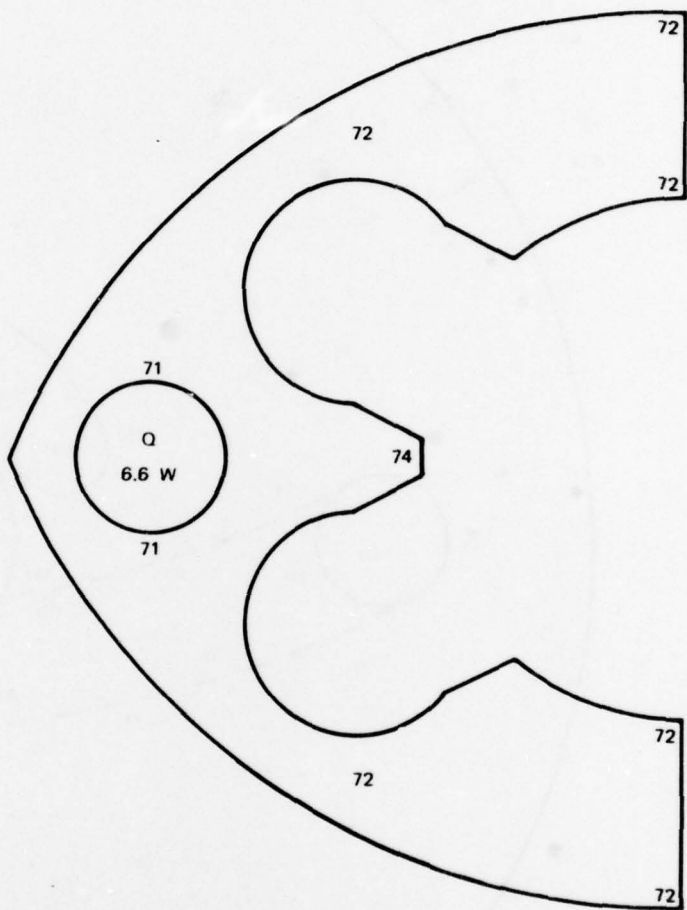


Figure 44 Thermal data spacer 5 (temperatures in degrees celsius).

G5721

POWER INPUT = 232 W  
COOLANT  
 $H_2O/GLYCOL$   
FLOW = 4 GPM  
INLET =  $65^{\circ}C$

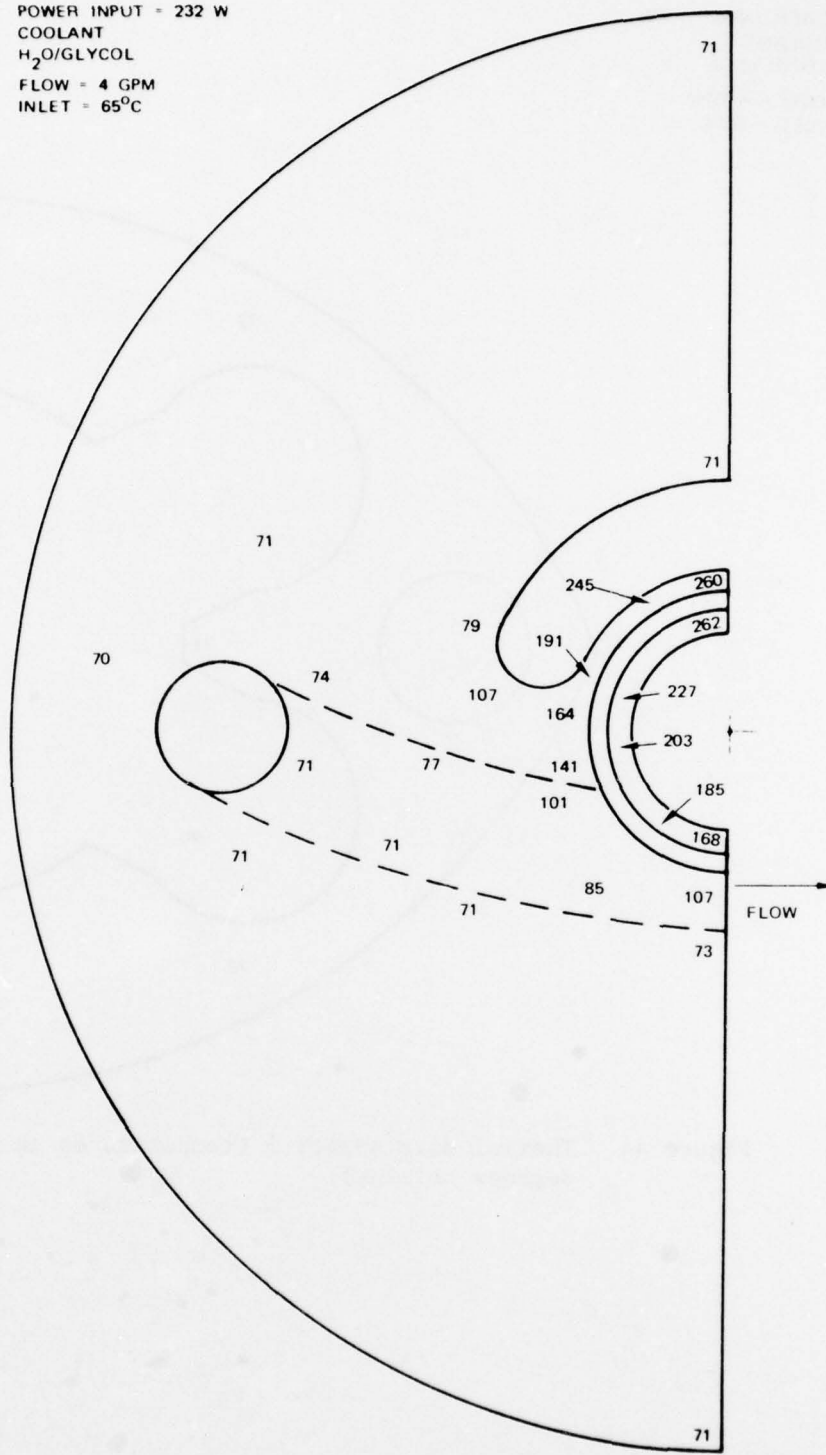


Figure 45 Thermal data pole piece 5 (temperatures in degrees celsius).

POWER INPUT = 0 W  
COOLANT  
 $H_2O$ /GLYCOL  
FLOW = 4 GPM  
INLET =  $65^0C$

G5722

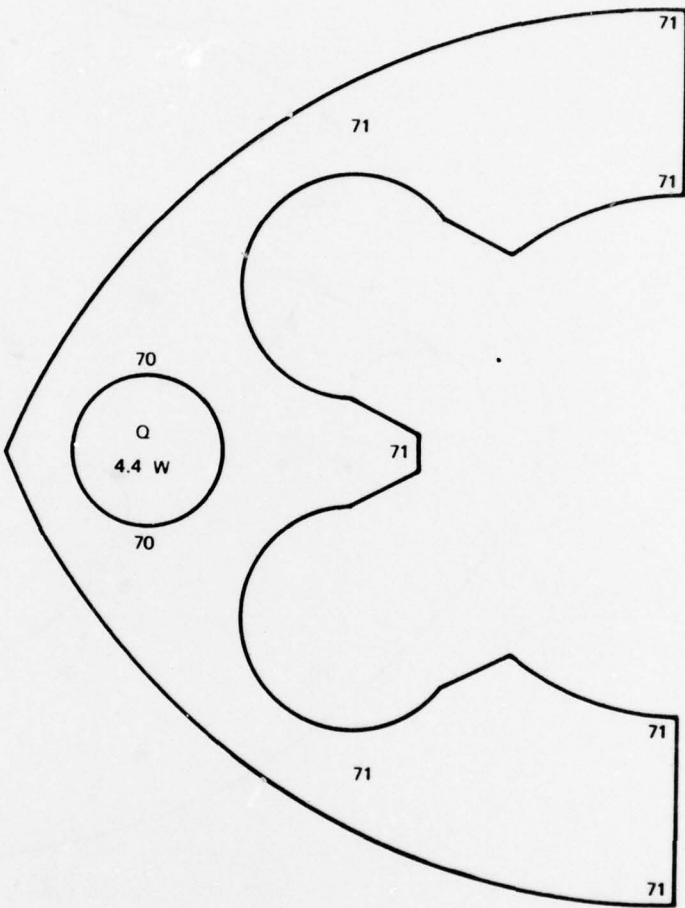


Figure 46 Thermal data spacer 6 (temperatures in degrees celsius).

POWER INPUT = 0 W  
COOLANT  
 $H_2O/GLYCOL$   
FLOW = 4 GPM  
INLET =  $65^{\circ}C$

G5723

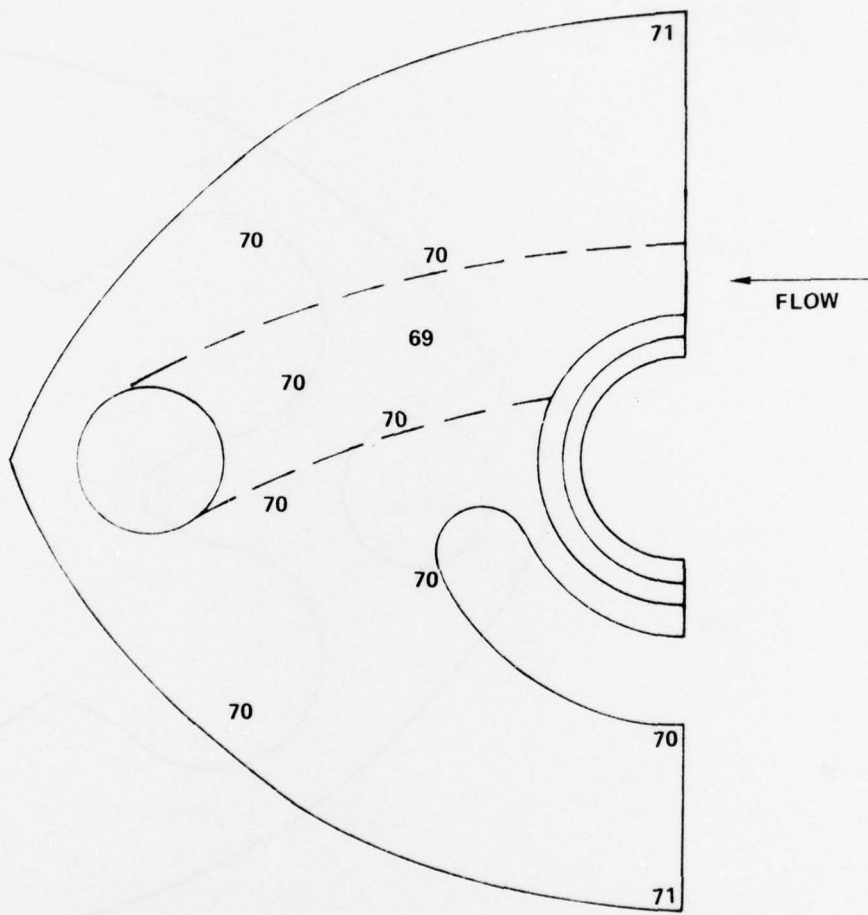


Figure 47 Thermal data pole piece 6 (temperatures in degrees celsius).

POWER INPUT = 0 W  
COOLANT  
 $H_2O$ /GLYCOL  
FLOW = 4 GPM  
INLET =  $65^{\circ}C$

G5724

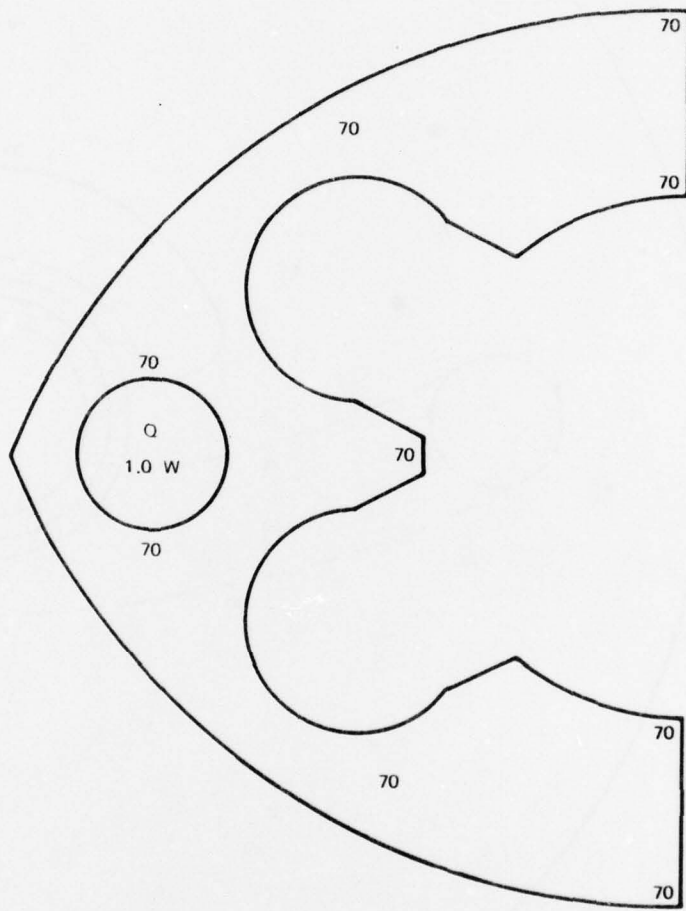


Figure 48 Thermal data spacer 7 (temperatures in degrees celsius).

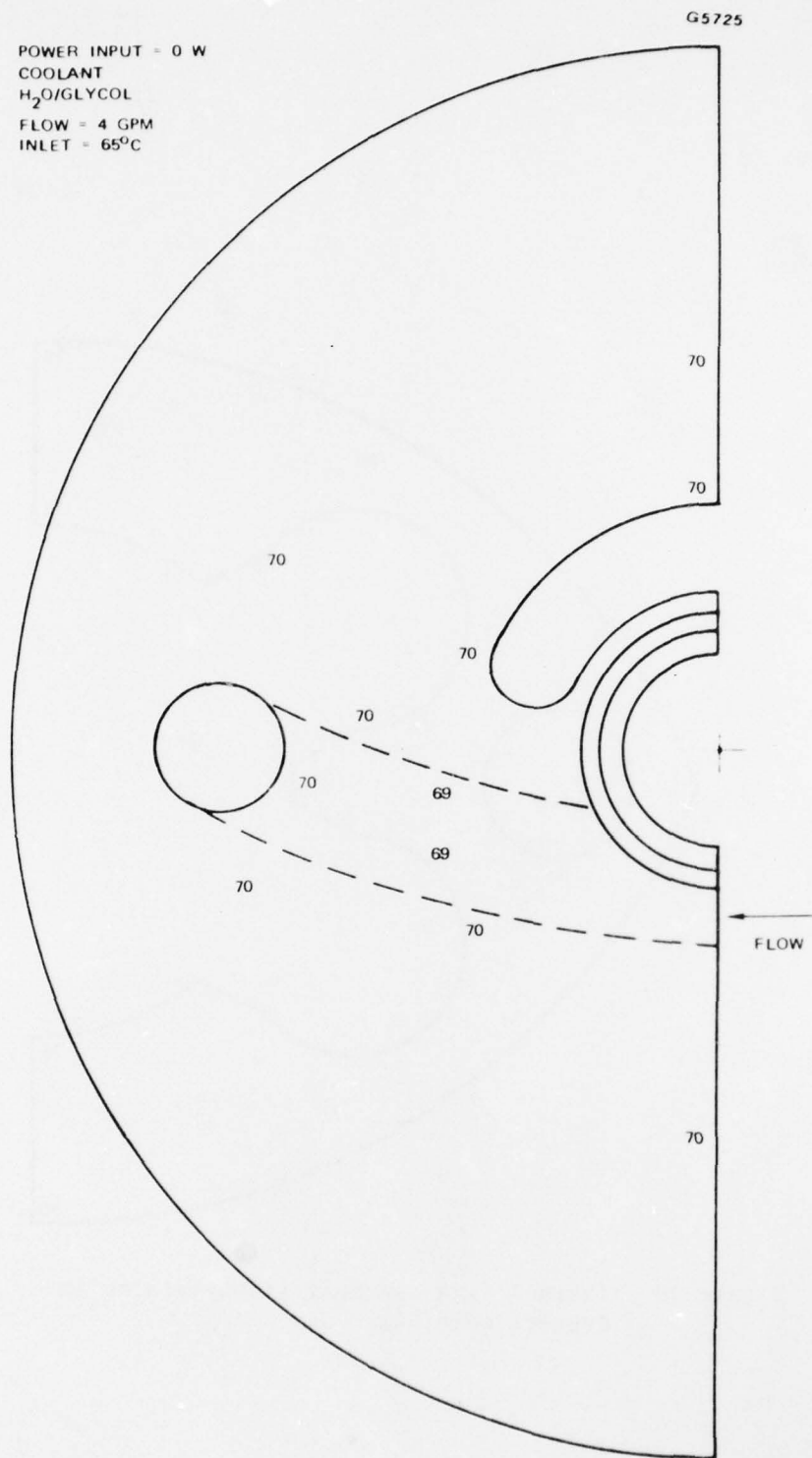


Figure 49 Thermal data pole piece 7 (temperatures in degrees celsius).

POWER INPUT = 0 W  
COOLANT  
 $H_2O$ /GLYCOL  
FLOW = 4 GPM  
INLET =  $65^{\circ}C$

G5726

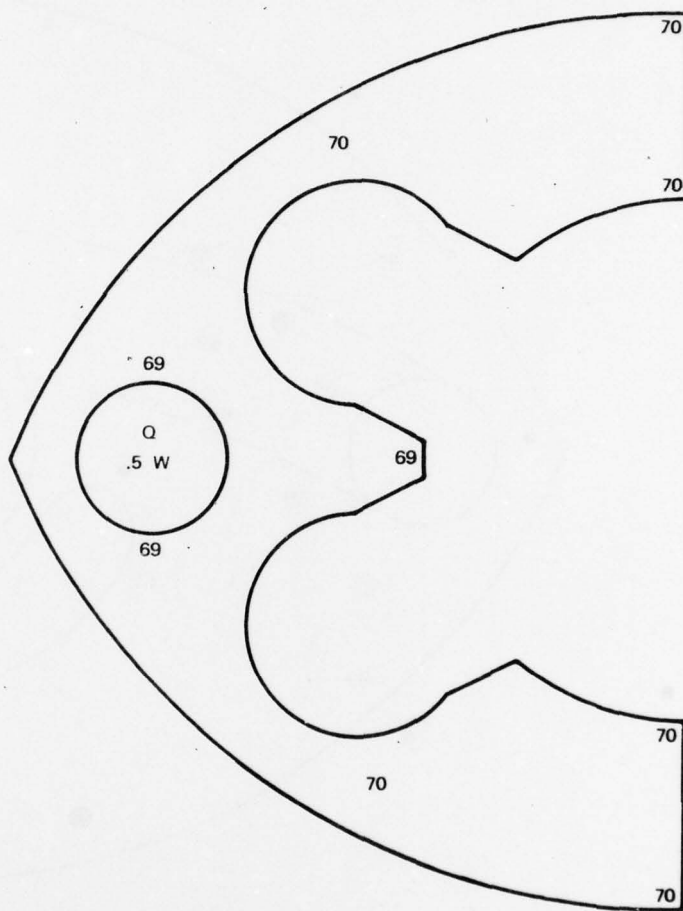


Figure 50 Thermal data spacer 8 (temperatures in degrees celsius).

POWER INPUT = 0 W  
COOLANT

H<sub>2</sub>O/GLYCOL

FLOW = 4 GPM

INLET = 65°C

G5727

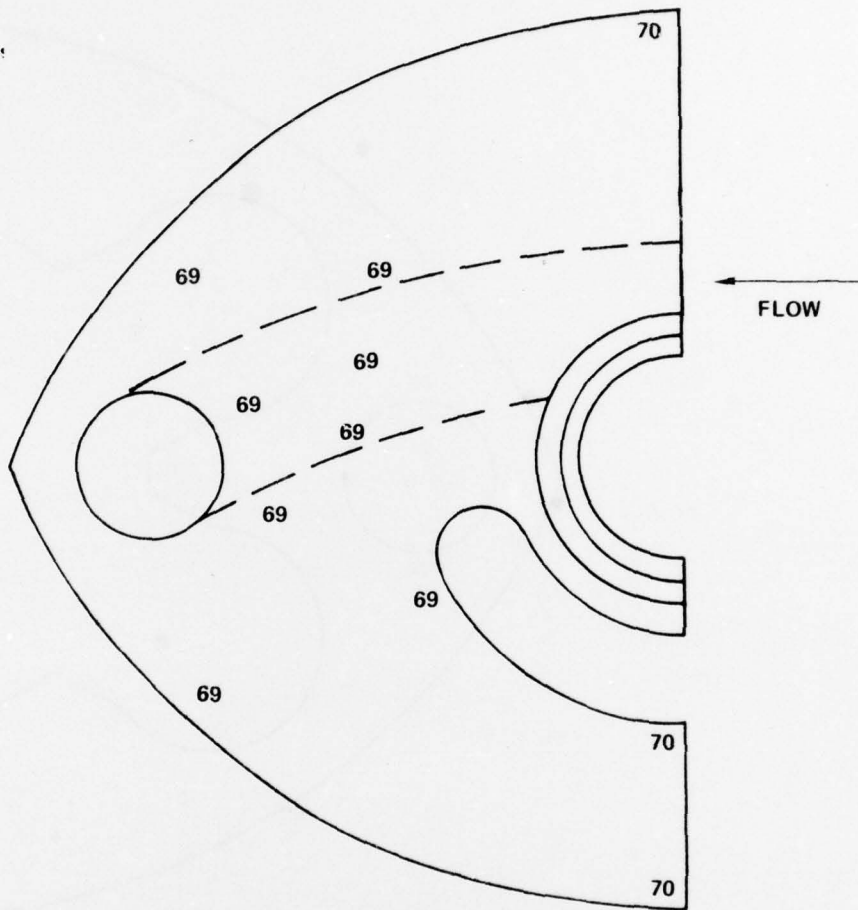


Figure 51 Thermal data pole piece 8 (temperatures in degrees celsius).

POWER INPUT = 0 W  
COOLANT  
 $H_2O$ /GLYCOL  
FLOW = 4 GPM  
INLET =  $65^{\circ}C$

G5728

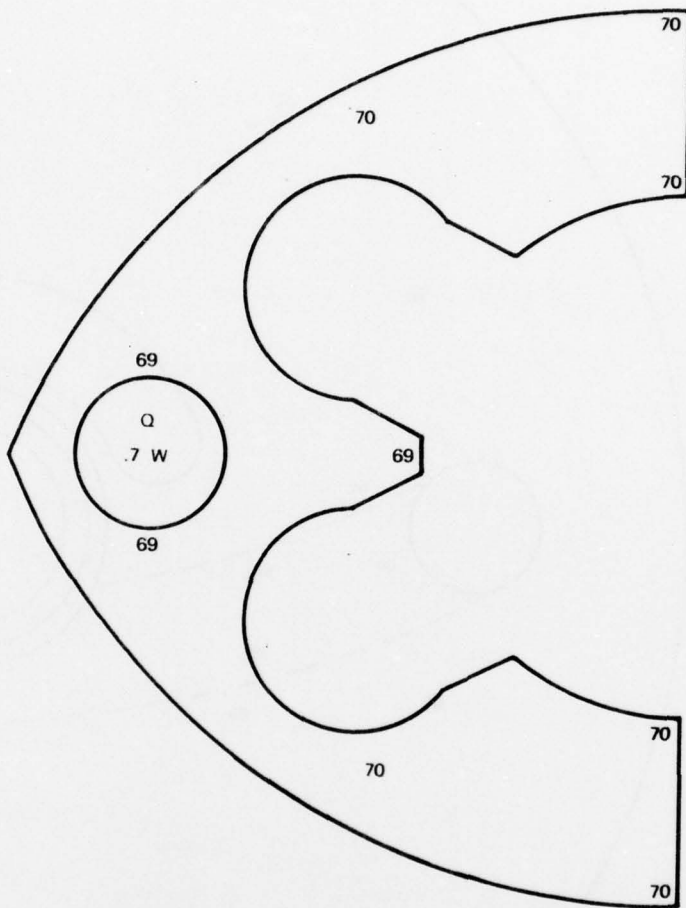


Figure 52 Thermal data spacer 9 (temperatures in degrees celsius).

G5729

POWER INPUT = 0 W  
COOLANT  
 $H_2O/$ GLYCOL  
FLOW = 4 GPM  
INLET = 65°C

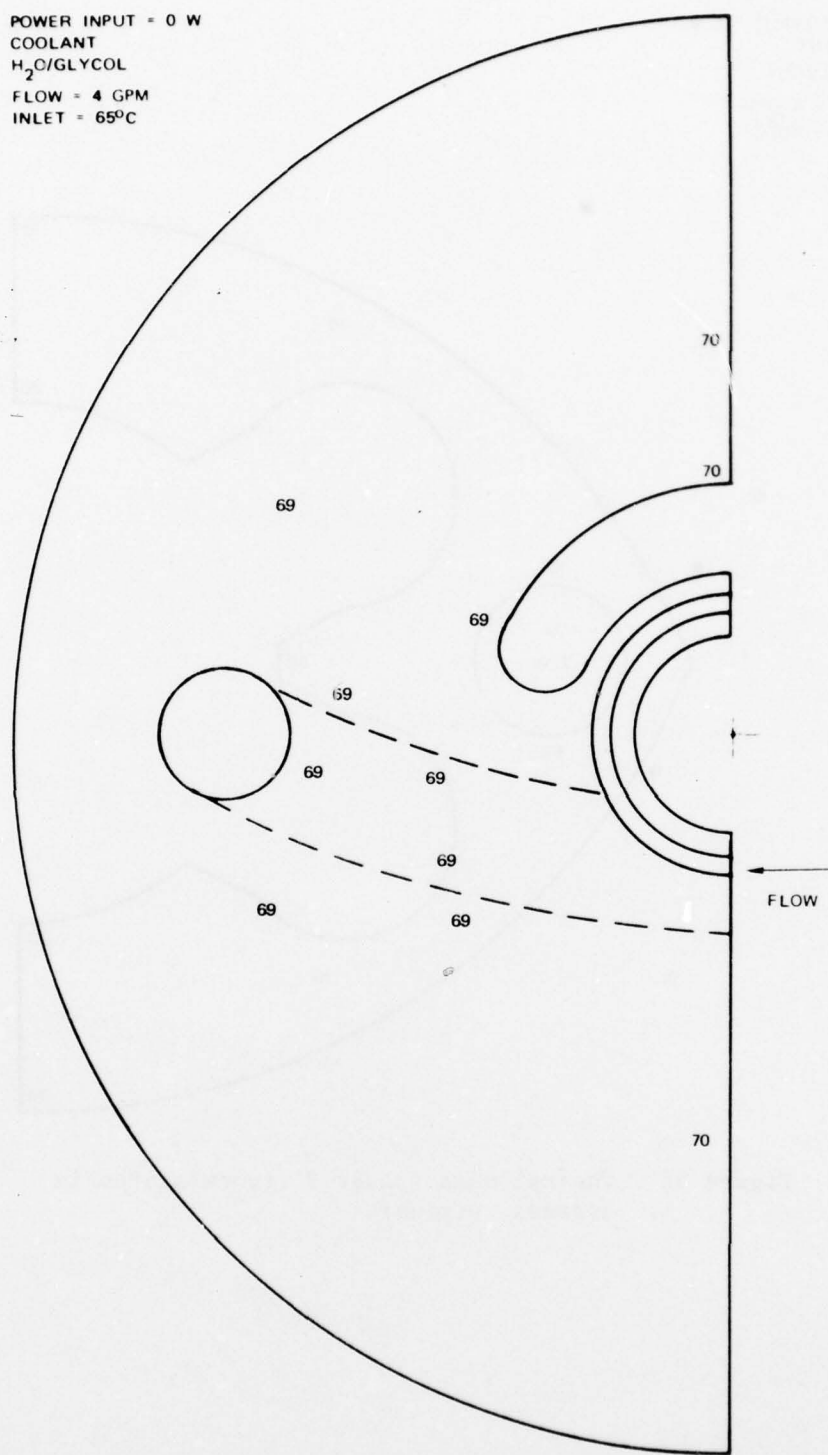


Figure 53 Thermal profiles pole piece 9 (temperatures in degrees celsius).

POLE PIECE 1 – THERMAL PROFILE

THESE ISOTHERMS REPRESENT A SLICE THRU THE POLE PIECE DISSIPATING 581 W. NOTE THE AFFECT OF THE COOLANT CHANNEL ON THE THERMAL DIFFERENTIAL AROUND THE FERRULE

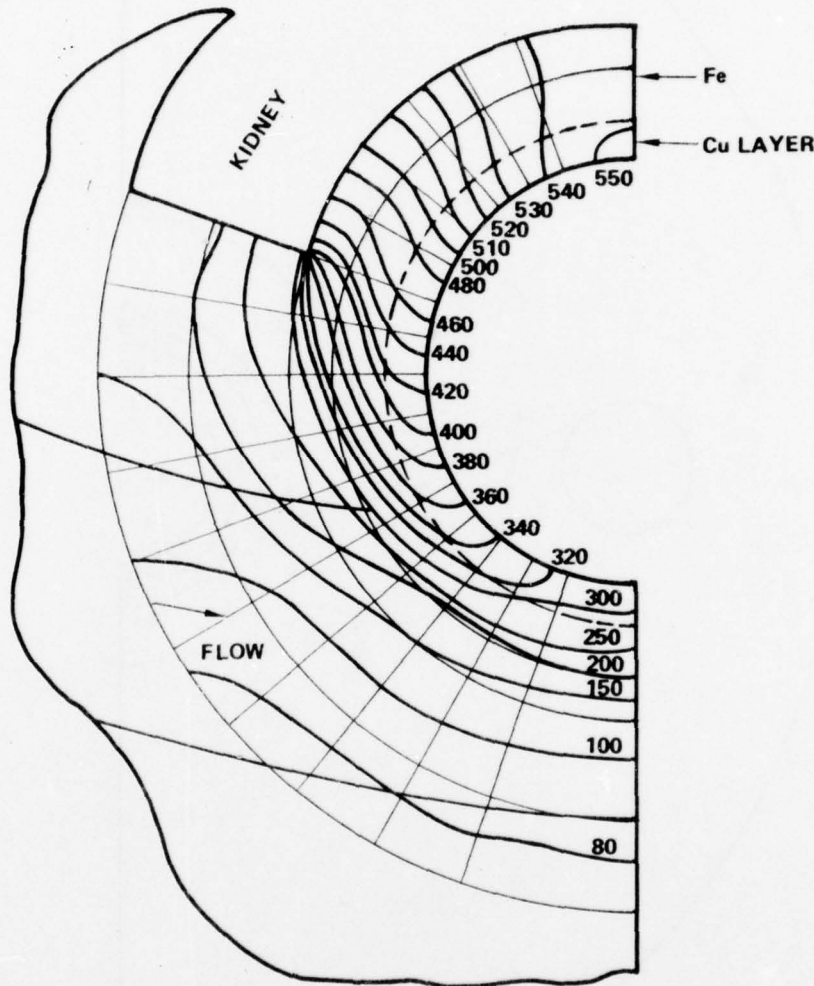


Figure 54 Pole piece 1 ferrule isotherms for 0.8 GPM flowrate (temperatures in degrees celsius).

G5731

POWER INPUT = 581 W  
COOLANT  
 $H_2O/GLYCOL$   
FLOW = 8 GPM  
INLET =  $65^\circ C$

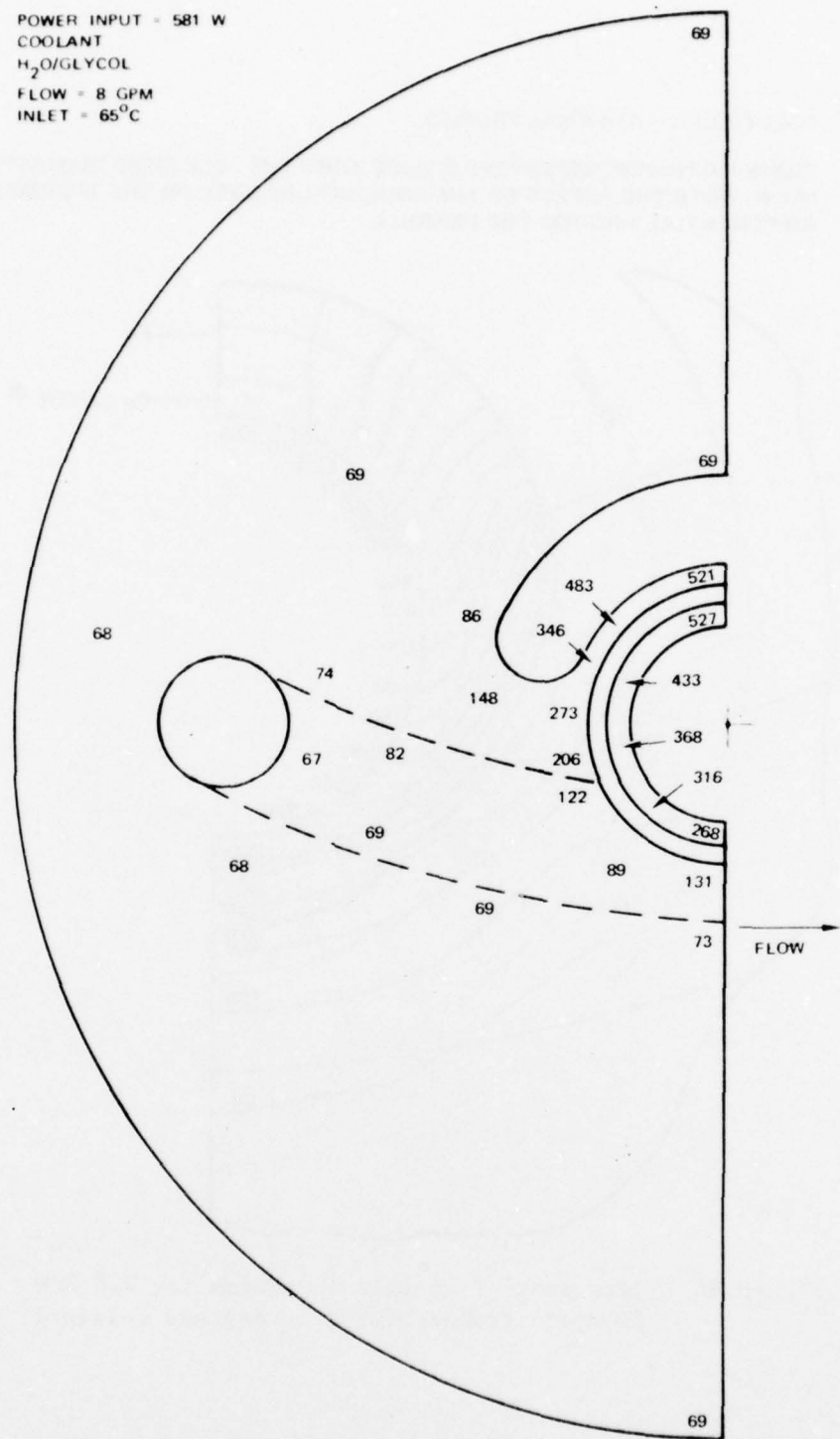
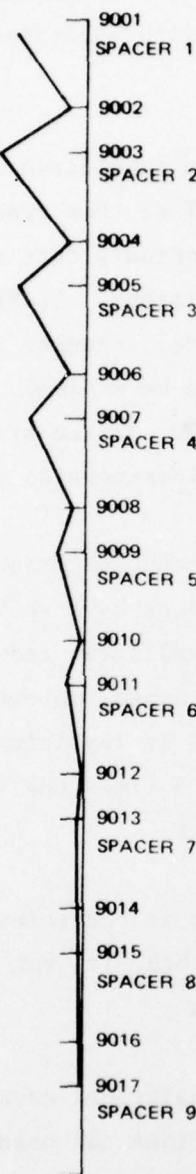


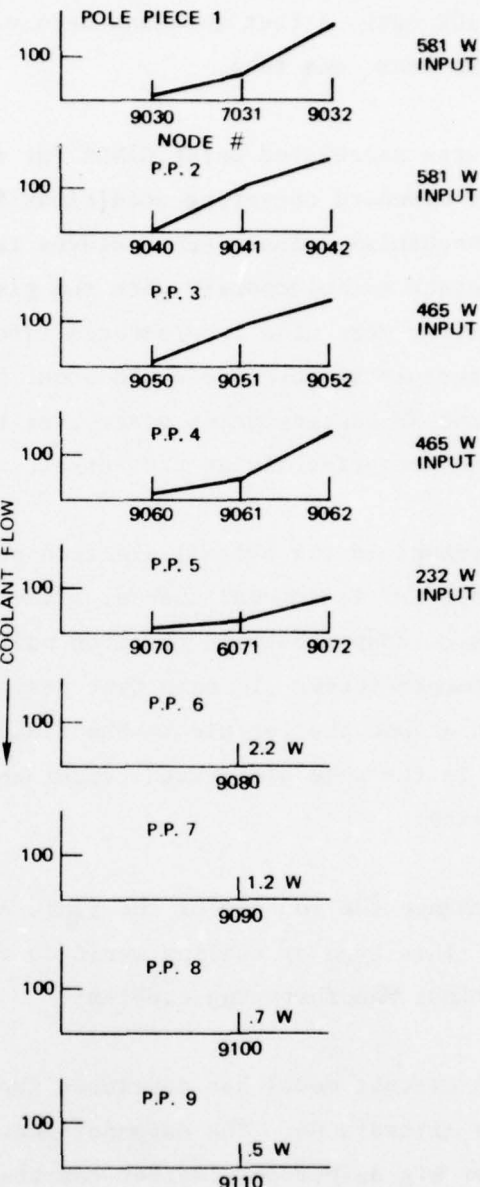
Figure 55 Thermal data pole piece 1, 8 GPM coolant flow (temperatures in degrees celsius).

ABSORBED POWER  
(WATTS)

20 10 0



G5732



POWER ABSORBED INTO FLUID NODES - 559H MODEL  
POWER DISSIPATION VS LENGTH

Figure 56 Power absorbed into fluid nodes -- 559H model power dissipation vs length.

allows meaningful conclusions to be drawn. In an absolute sense, the modeling fell short of demonstrating that the 559H is capable of operating at 10% duty, a fact that has been verified with laboratory test data on at least one tube.

Temperatures calculated using CINDA for the cases considered are indicative of standard operating conditions for a TWT of this frequency and cooling mechanism. These temperatures tend to indicate that this TWT would operate satisfactorily with the given conditions. If RF heating of the cavity were also incorporated into the model, changes in the maximum ferrule temperature would occur but would be minimal. This is because the RF heating takes place over the entire surface area of the cavity and not primarily at the ferrule as with interception power.

An improvement in the overall electron beam interception capabilities of the 559H TWT is accomplishable. Previous studies have shown that laminates of copper between the iron pole piece walls can reduce high ferrule temperatures. In this type design this change improves the heat path around the ferrule to the fluid channel by replacing some of the iron in the pole piece with copper which has 5 times the thermal conductivity.

One may change the routing of the fluid such that it encircles the ferrule. This type of cooling would do the most benefit, but also poses serious manufacturing problems.

This 559H circuit model has developed improved analytical capabilities at Hughes Aircraft Co. The expanded version of CINDA can handle models 4 times as big as before. Better computer file management to reduce computer costs has also been perfected. The thermal model is available for future investigations of this or similar high power TWT circuits.

### 3.8 TUBE DESIGN FOR HIGH AVERAGE POWER

The results of the present study were to be applied in the form of a high power TWT tube design using permanent magnet focusing. It was mutually agreed that the tube should be in the power range of 150 to 175 kW centered at 3.3 GHz.

The 559H tube presently has an average power capability of 10 kW with roughly 12% beam interception under full drive. If the beam interception could be reduced by a factor of two the average power capability could be essentially doubled, since most of the thermal losses are presently due to beam defocusing at large RF drive levels. Reduced interception, combined with improvements in the thermal dissipation capability of the basic circuit structure, could more than double the average power capability of such a device.

Simply adding magnetic focusing field to the 559H design reduces the beam diameter and lowers the interaction efficiency of the tube. In modeling the 559H a change in beam diameter of only 10% (a beam filling factor of 0.50 rather than 0.55) reduced the output power at the mid-band frequency from 164.7 kW to 139.4 kW. If the extra magnetic field was used to confine the beam, keeping the beam diameter the same, some reduction in power would result from the added effective space charge debunching forces that result from confinement. More importantly, however, the parameters of the 559H are not suitable for operating at any appreciable degree of confinement without seriously compromising the focusing characteristics of the beam.

In this study a limit of  $\alpha = 0.15$  has been set for satisfactory focusing from the standpoint of beam ripple and beam stability. However, at low values of confinement this could perhaps be relaxed somewhat. The  $\dot{z}/u_0$  velocity variation of the beam in the flux reversal regions is a

direct function of  $\gamma$  where  $\gamma = (2\pi r/L)^2$ ,  $r$  is the beam radius and  $L$  is the magnetic focusing period. The actual magnitude of this effect is determined by the product  $\alpha\gamma$  and by a function of the degree of confinement. For confinements of roughly  $\sqrt{2} \times$  Brillouin a value of  $\alpha\gamma = 0.025$  limits the  $\dot{z}/u_0$  variation to approximately 5% during the negative peaks of the PPM field, or approximately 10% slow-down in terms of equivalent voltage. For  $\alpha = 0.15$  this would correspond to a limit on  $\gamma$  of 1/6.

In the present 559H,  $\alpha = 0.15$  would limit the rms focusing field to around 670 gauss. Since the tube now operates with around 550 gauss (rms) this would only allow a  $B/B_{Br}$  ratio of about 1.2. The beam diameter under these conditions would represent a  $\gamma$  of 1/3, or  $\alpha\gamma = 0.05$ , which is twice the above value assumed for acceptable focusing.

The lower perveance redesign of the 559H uses a smaller diameter beam and circuit which results in a high interaction efficiency. It also keeps the  $\gamma$  focusing factor low (below 0.13). However, the relatively high Brillouin value of field associated with the smaller diameter again prevents using more than about a 1.2-1.25 confinement ratio.

This 65 kV design operates with a cavity period of 1.16 inches. Assuming a 62.5 kV beam velocity on the axis limits the focusing field to 640 gauss for  $\alpha = 0.15$ . Assuming a maximum  $\gamma$  of 1/6 allows increasing the beam diameter to a design value of 0.300 inches. A circuit diameter of 0.550 inches is then required to maintain a filling factor of around 0.55. The actual Brillouin field is now 460 gauss (relativistic) which would allow a confinement ratio of nearly  $1.4 \times$  Brillouin. The non-relativistic Brillouin field that would be consistent with the PPM focusing analysis used in this report can be calculated from Equation (26) and is 489 gauss, or a 1.3 confinement ratio. This design meets the above accepted focusing criteria, and at  $1.4 \times$  Brillouin field

could be expected to operate with a minimal amount of RF defocusing under drive.

In each of the above designs the  $\omega\beta$  phase characteristic of the circuit was assumed to be that of the present 559H circuit. This characteristic is shown in Figure 57. The 3.3 GHz center frequency for this circuit falls at a  $\beta l_c / \pi$  of 1.4188.

A summary of some of the more pertinent tube design parameters is given in Table 4. The magnetic pole piece diameter of 0.630 inches allows for a 0.040 inch thick copper insert for forming the actual beam tunnel wall. Direct cooling of the output circuit ferrules is provided by means of coolant channels in each of the pole pieces in a similar manner as in the 559H. Although mechanically more difficult, achieving a maximum improvement in average power capability requires that the coolant be routed such that it completely encircles the ferrules. The thermal analysis of the 559H shows that passing coolant over only the portion of the ferrule opposite the kidney hole results in a large temperature differential in the ferrule away from the coolant channel. This showed up as the weakest link in the present 559H thermal design.

Single period PPM focusing is suggested employing SmCo magnet material. The shape of the rms field is not critical to the focusing and with integral focusing it is common to make the RF and magnetic gaps the same. The shape of the PPM field (normalized to 0.707 rms) is shown in Figure 58 for two separate magnetic gap lengths. The larger gap has less 3rd harmonic, but it was felt that a smaller gap would provide greater shielding of the beam from transverse field effects due to the asymmetry of the RF coupling slots in each of the pole pieces. Figure 59 shows the computed beam ripple and  $z/u_0$  variation for each of the two magnetic gap lengths. Note that the ripple magnitude is of the order of 5%, as is the velocity slow-down during the negative peak

G5733

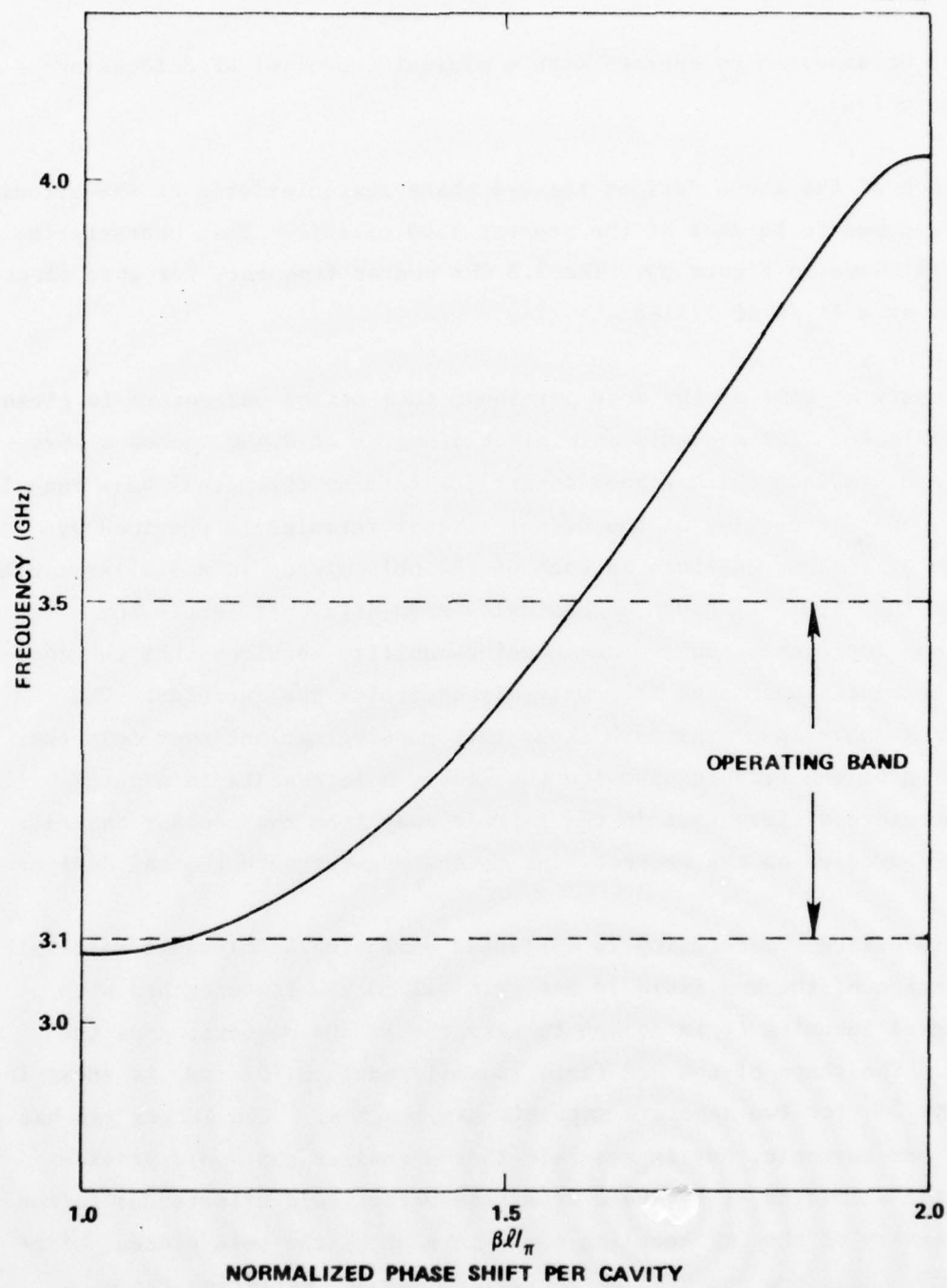


Figure 57 Phase characteristic of the 559H coupled cavity TWT circuit.

TABLE 4  
DESIGN-TUBE PARAMETERS

Frequency range	3.1 to 3.5 GHz
Power output (peak)	150 kW (min.)
Power output (average)	>20 kW
Small signal gain	>50 dB
Large signal gain	>45 dB
Cathode voltage	65 kV (nominal)
Cathode current	11.54 Amps
$\mu$ Perveance	0.7
Axial beam velocity ( $u_o$ )	5.358 in./nsec
Cavity period ( $\ell_c$ )	1.16 in.
Magnetic period (L)	2.32 in.
Beam diameter (2b)	0.300 in.
Circuit diameter (2a)	0.550 in.
Beam filling factor (b/a)	0.545
Magnetic focusing parameter ( $\alpha$ )	0.15
Space charge focusing parameter ( $\beta$ )	0.088
Radial focusing parameter ( $\gamma$ )	0.165
Velocity variation parameter ( $\alpha\gamma$ )	0.0248
RMS focusing field (B)	640 gauss
Peak focusing field ( $B_{pk}$ )	1090 gauss
Magnetic pole piece diam. (D)	0.630 in.
Magnetic gap (G)	0.350 in.
G/L (magnetic)	0.151
RF cavity gap (g)	0.350 in.
$g/\ell_c$ (RF circuit)	0.302
L/D (magnetic)	3.68
$B/B_{Br}$ (confinement)	1.3 - 1.4
$\beta\ell/\pi$ (circuit phase at 3.3 GHz)	1.4188

TABLE 4  
DESIGN-TUBE PARAMETERS (CONT)

$\gamma_a$ (RF normalized circuit radius)	0.94
No. of cavities (11-12-14)	37 total
Output cavity period taper (2 cavities)	70% - 70%
Cavity web thickness	0.280 in.
Ferrule thickness (including 0.040 in. Cu insert)	0.084 in.
Ferrule O.D.	0.718 in.
Focusing - SmCo, PPM, single period, integral	
Band edge stability - resonant loss buttons	
Cooling - liquid (cross-channel direct cooling of pole piece ferrules)	

G5734

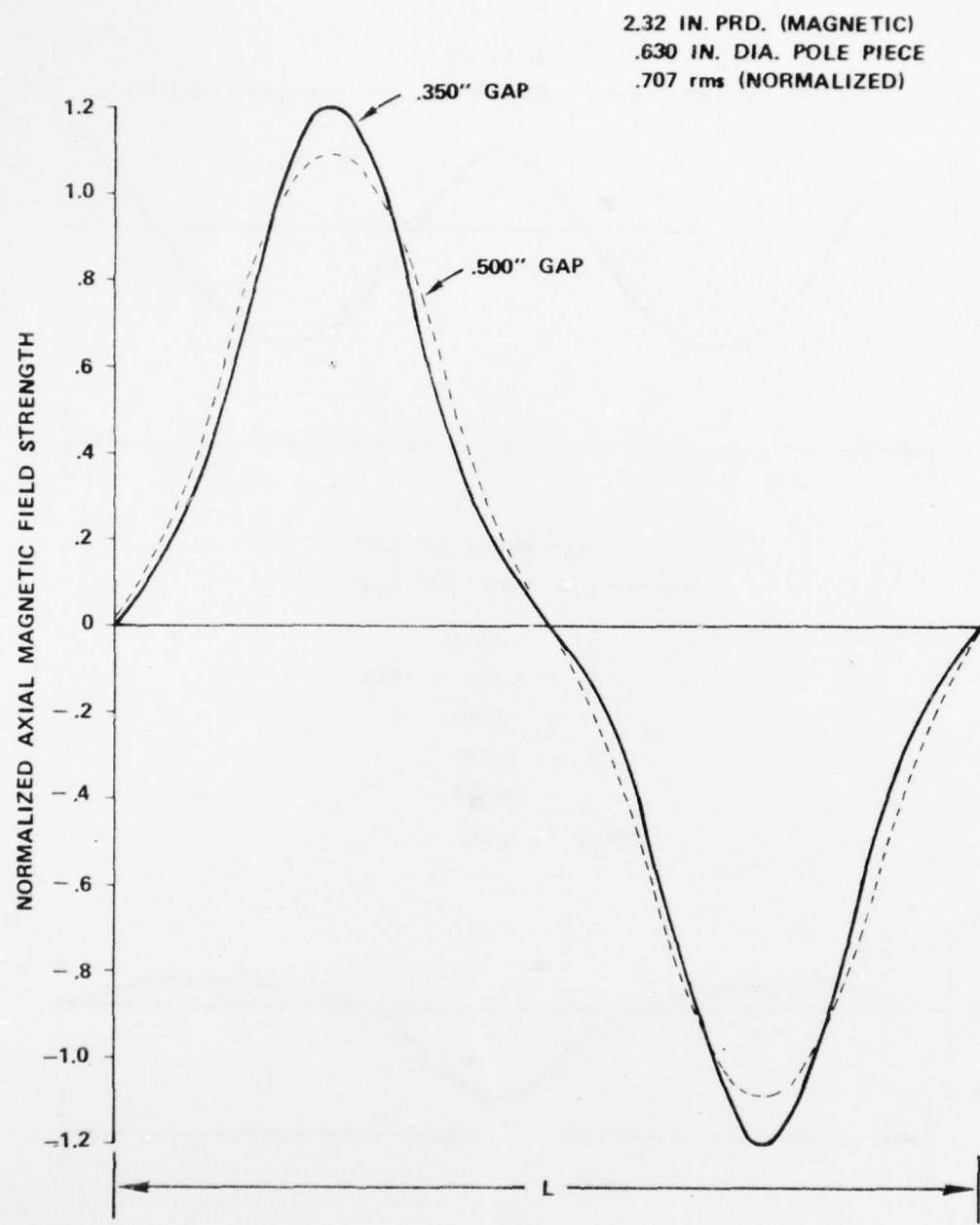
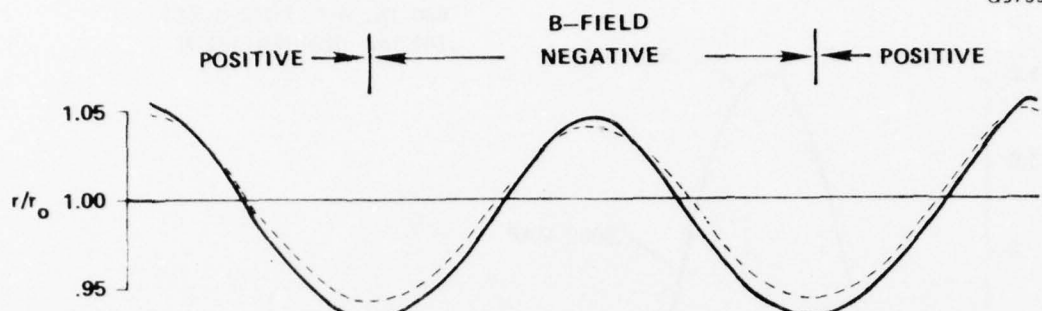


Figure 58 Calculated PPM magnetic field shapes for two different magnetic gaps.

G5735



- - - .500" MAGNETIC GAP  
 - - - .350" MAGNETIC GAP

$$r_0 = .150 \text{ IN.}$$

$$u_0 = 5.358 \text{ IN./NSEC}$$

$$\alpha = .15043$$

$$\beta = .08770$$

$$\gamma = .16503$$

$$B/B_{BR} = 1.310$$

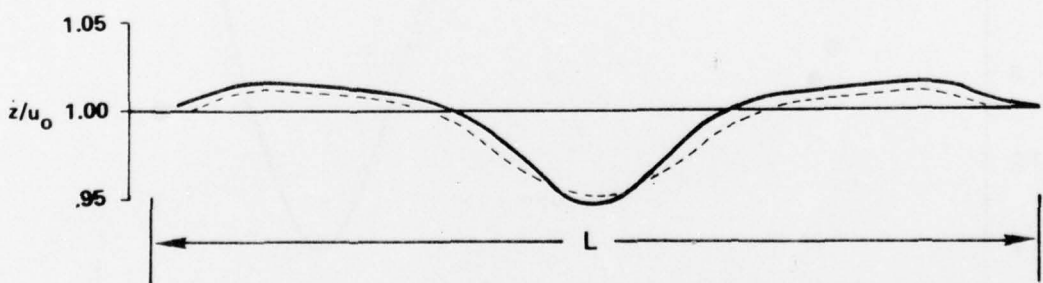


Figure 59 Calculated beam ripple and axial velocity variation for the assumed focusing design.

of the focusing field. Double period focusing produces essentially the same results as single period focusing when there is no flux in the cathode, because of the symmetrical nature of the positive and negative field focusing (see Figures 4 and 6). In the present design, with initial cathode flux, focusing symmetry no longer exists and the beam is subject to becoming unstable with double period focusing due to the longer focusing period.

The RF performance of the above design was calculated for both large and small signal behavior. Figure 60 shows calculated small signal gain for the three section design which consists of 11-12-14 cavities including a velocity taper in the output for efficiency enhancement. Large signal calculations show this configuration producing 175 kW of saturated power at band center (3.3 GHz) for a 65 kV operating voltage with the assumption that the beam is totally confined. Figure 61 shows the calculated saturation power output across the 3.1-3.5 GHz band.

One of the questions that came up during the study of PPM beam confinement was whether a confined beam that is somewhat closer to the circuit would be better than a smaller Brillouin beam that was further away from the circuit. Normally, a reduction in beam size reduces interaction efficiency because of increased space charge effects. However, the low permeance of the present design has already minimized these effects. Assuming the non-relativistic  $1.3 \times$  Brillouin level of confinement, additional RF calculations were made for the above design with a 1.3 times smaller (Brillouin) beam. This would result from having the same magnetic focusing field and no degree of confinement. The difference in plasma frequency reduction factors between the Brillouin and confined beam caused the smaller Brillouin beam to interact in a comparable manner (for both large and small signals) to the larger confined beam. In either case the RF defocusing should be

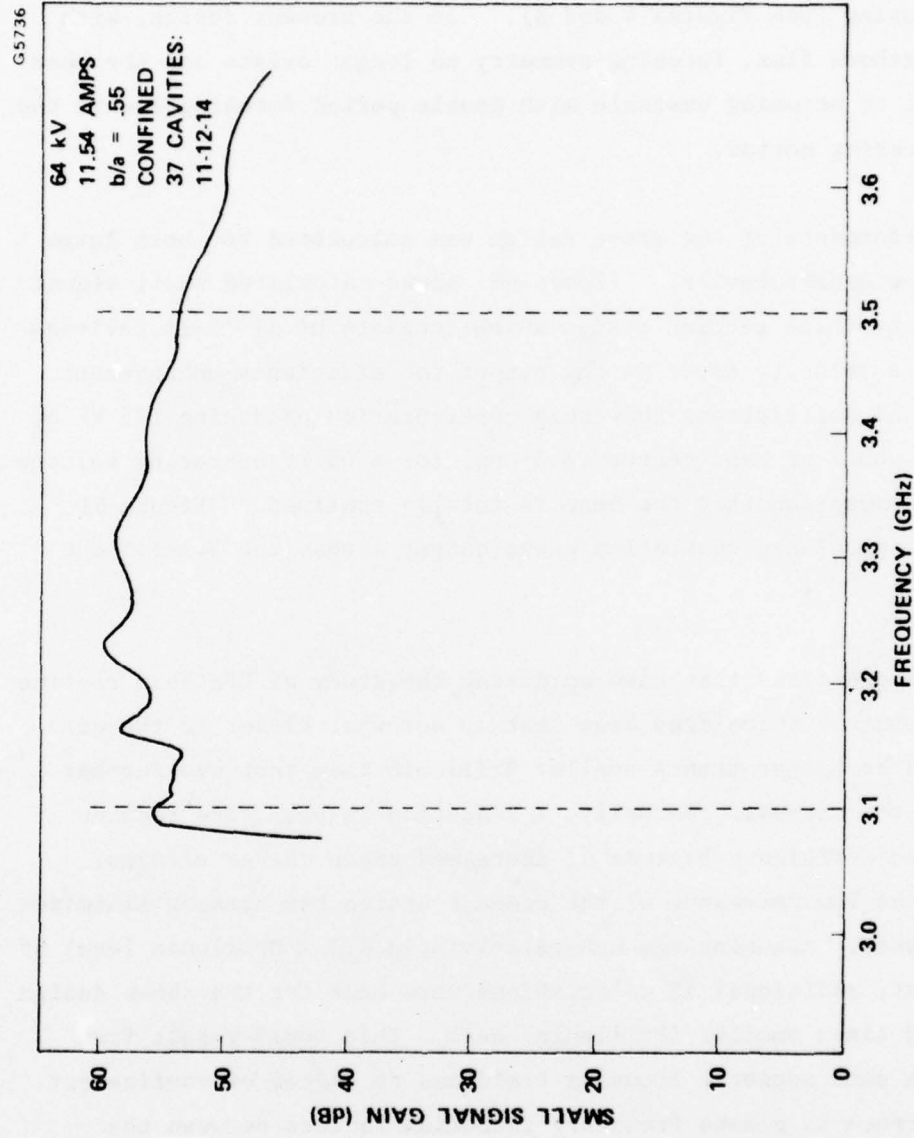


Figure 60 Calculated small signal gain of design tube.

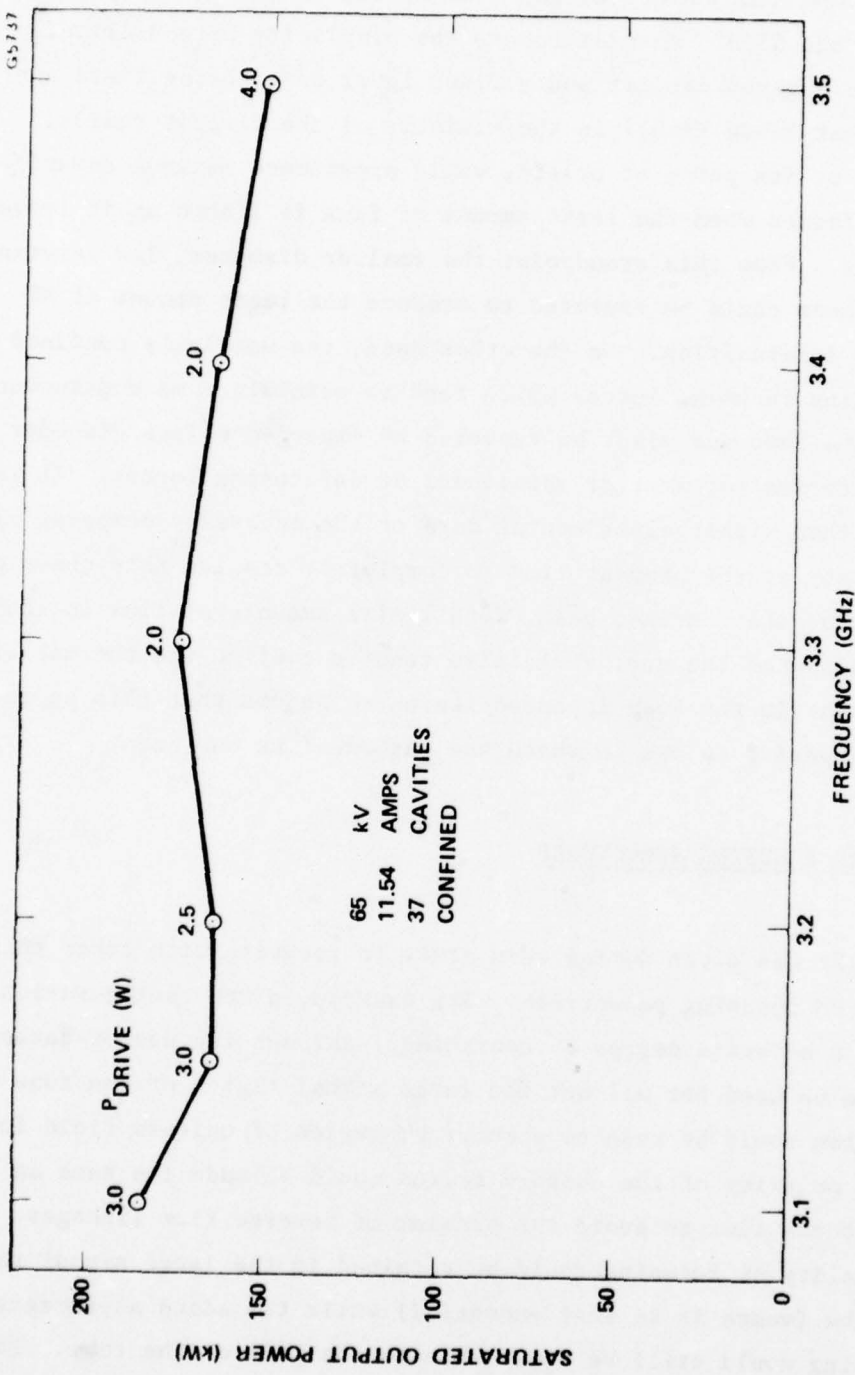


Figure 61 Calculated large signal performance of design tube.

improved dramatically over designs such as the original high perveance version of the 559H. In addition to the simplicity of a Brillouin design, for a given circuit and a fixed level of focusing field any electron that finds itself in the vicinity of the circuit radius, regardless of its point of origin, would experience maximum inward restoring forces when the least amount of flux is linked as it leaves the cathode. From this standpoint the smaller diameter, low perveance Brillouin beam could be expected to produce the least amount of RF defocusing interception. On the other hand, the partially confined beam contains focusing forces which tend to maintain a more structured order to the beam and might be expected to experience less disorder in its trajectories for similar magnitudes of defocusing forces. It is not clear that either experimental data or the necessary computer capability exists at the present time to completely resolve this question. The fact that the confined beam, with finite amounts of flux in the cathode region of the gun, would also tend to confine the thermal electrons present in the beam is added reason to assume that this approach might be superior to one in which the cathode flux was zero.

### 3.9 HYBRID FOCUSING STRUCTURES

Some thought was given during this study to focusing with other than straight PPM focusing geometries. For example, a PPM configuration embodying a moderate degree of confinement through the use of cathode flux could be used for all but the large signal region of the tube where a transition could be made to a short PM region of uniform field focusing. The polarity of the uniform region could be made the same as that of the cathode flux to avoid the problem of reverse flux linkages. Thus, a high quality of focusing could be retained in the large signal region of the tube (where it is most essential) while the added advantages of PPM focusing would still be applicable to the rest of the tube. The

compounding effects of the beam slowing down both because of large signal interaction and because of high peak values of reverse flux could thus be avoided. Beam interception as the result of RF defocusing would be minimized over straight PPM focusing, thereby increasing average power limitations. In addition, a region of straight field focusing would allow complete freedom with respect to RF output circuit period tapers in those instances where the circuit structure and periodicity also form a part of the PPM magnetic structure, as is the case with integral PPM focusing.

Other configurations than straight PPM focusing that could be used to advantage would be tapering the strength of the PPM fields to increase beam control in the regions of large signal interaction and/or tapering the magnetic period. A tapered period structure would be desirable for maintaining a level of beam control in a region where significant slowing down of the electrons was occurring as a result of high level interaction. In the case of coupled cavity TWT circuits using common circuit and magnetic periodicities, the tapered magnet period would be combined with a cavity circuit velocity taper design for purposes of efficiency enhancement. Optimization of the taper could lean towards either the magnetic or the electrical design depending upon their relative importance in specific applications.

In investigating these alternatives it became apparent that, while there were certain advantages to these schemes, none really addressed the real problem of losing control of the beam optics in the presence of large signal interactions. A uniform field region that is preceded by a PPM region is limited in the degree of confinement that can be used by the focusing parameters of the PPM section. Thus, no additional advantage of confinement could be realized and only the limited advantage of straight field over PPM would result. The fact that the same problem of defocusing occurs with uniform field focusing as with

PPM focusing, in the absence of confinement, is clearly illustrated in Figures 18 and 19 .

Tapering the field toward the output of the tube can be effective in reducing beam interception, but always with some sacrifice of interaction efficiency as the beam is forced to a smaller diameter. The principal advantage of this arrangement over using a high field over the entire tube length is in allowing the beam to become more fully bunched before it enters the high efficiency portion of the interaction. This takes place fairly rapidly in a high perveance, high efficiency tube. Yet, a rapid change in focusing field introduces large perturbations in the trajectories which can combine with the large signal defocusing to intensify beam interception. On the other hand, a gradual taper in magnetic field reduces the beam size before the beam is fully bunched. As pointed out in the previous section in connection with the high average power tube design, a low perveance beam can still interact strongly with the circuit at small beam filling factors due to reduced space charge in the beam. It would appear that low perveance beams, either with confinement or with high magnetic field Brillouin flow (low beam filling factor) are the most effective means for minimizing interception due to RF drive.

### 3.10 SYSTEM LIFE CYCLE ANALYSIS

One of the requirements of this study was to analyze a solenoid focused, production TWT in order to determine the percent system life cycle improvement that could be realized through the application of permanent magnet focusing. The AWG-9 Weapons Control System (WCS) was selected as the candidate to demonstrate the life cycle cost criteria because:

1. The system is both in production and in Navy field service. Consequently, the availability of technical personnel familiar with the hardware design assures field data indicating real systems reliability and maintainability (R&M) problems.
2. This system has been and is the subject of critical examination by several organizations with respect to improving reliability and maintainability performance.
3. As a by-product of these critical examinations, Hughes is presently engaged in the third of a three phase reliability and maintainability program for the AWG-9 WCS. Within the scope of the R&M Program, the present system, transmitter, and TWT have been carefully scrutinized for exact determination of failure cause (primary/GTWT or secondary/system).

The present AWG-9 radar transmitter was designed between 1969 and 1970. As of October, 1976, Hughes had delivered 380 of the approximately 480 AWG-9 radar transmitters. These transmitters were deployed at NAS Miramar, NAS Oceana, aboard aircraft carriers, and at various Navy evaluation facilities such as NAS Patuxent River and NAS Pt. Magu. Substantial valid Navy field experience exists to adequately define the transmitters reliability.

Life Cycle Cost (LCC) Analysis typically provides the total cost of a system for use in evaluating alternative choices among competing systems or competing mechanisms of a single system. The LCC of a system is the total cost incurred from the initial design stage until the system is phased out of inventory. For costing, the life cycle is divided into three phases: development, investment, and operating. The LCC profile

shown in Figure 62 relates the funding required per unit of time for each phase of the life cycle.

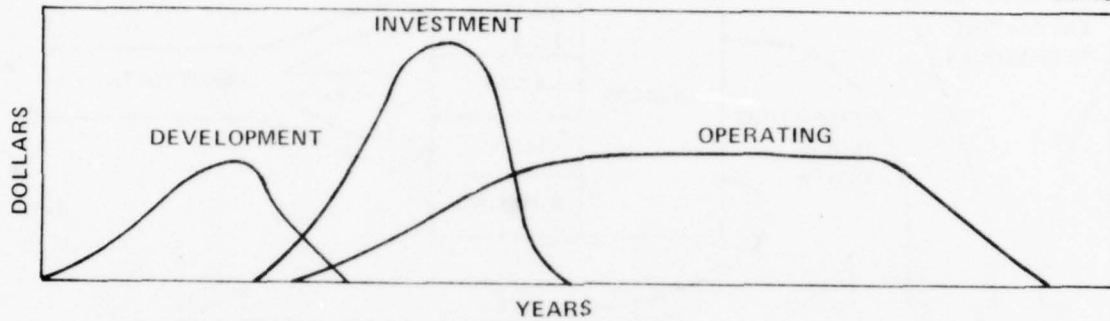
Practical LCC Analyses are concerned with the relative cost impact of candidate courses of action or system design changes. In these cases, the LCC element of interest is the operating phase (and in some cases, a portion of the investment phase) cost savings compared to the development and, usually, all of the investment phase cost.

Since life cycle cost analysis is used so extensively for evaluation of candidate designs or actions, generally it is not necessary to continue to compute the LCC of the entire system. Only the differences in costs and savings need be determined after the life cycle cost of a base line system configuration is calculated. Consequently, the relative near-term development and investment costs are best determined by making engineering cost estimates. Because of the complexities in estimating all cost elements, modeling is the best method of determining operating costs.

To perform the detailed analysis required for the AWG-9 WCS, a set of models capable of operating together to produce system life cycle costs had to be used.

The Hughes' life cycle cost computer model (HACCOST) shown in Figure 63 can produce generalized LCC information. Although a cost estimating and accounting model, it cannot calculate operating costs with the amount of detailed logistics information available from the AWG-9 system. Therefore, ALARM (A Logistics Analysis and Ranking Model), also developed by Hughes, is used in conjunction with the HACCOST model.

G5738

DEVELOPMENT

DESIGN  
PROTOTYPES  
TESTING  
SYSTEM ENGINEERING  
PROGRAM MANAGEMENT  
TECHNICAL DATA

INVESTMENT

IMPLEMENTATION  
PROGRAM MANAGEMENT  
HARDWARE PROCUREMENT  
INITIAL SPARES  
ENGINEERING SUPPORT  
INITIAL TRAINING  
MAINTENANCE MANUALS

OPERATING

DIRECT PAY & ANALYSIS  
INDIRECT PAY & ANALYSIS  
TRAINING  
FACILITIES MAINTENANCE  
SPARES  
DEPOT REPAIRS

Figure 62 Profile of funding for life cycle cost analysis.

G5739

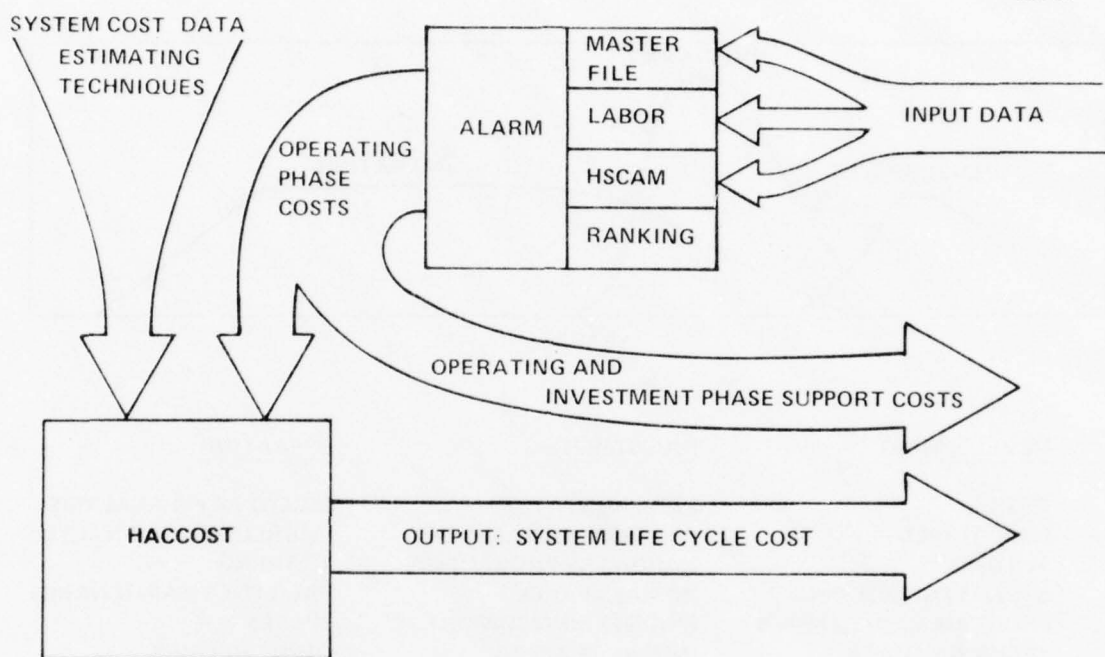


Figure 63 Hughes' life cycle cost model relationships.

The HACCOST model inputs operating phase cost estimates that are received from the ALARM model; the actual data transfer is made via a magnetic tape produced by HSCAM, a submodel of ALARM, in a format which can be read by HACCOST. ALARM is composed of four submodels or programs that may be operated together to provide a unified result or run individually to produce answers limited to that program's emphasis. The HACCOST model features the ability to calendarize the dollar amounts (fiscal funding) and separate and display costs in desired groupings (development, construction, etc.).

Operating phase cost calculations require a variety of input variables. Scenario constants (flight rates, aircraft per squadron, etc.) and logistics data (mean time to repair, ship arrival rates, etc.) provide the common data base. The sources of these data are Navy approved Maintenance Engineering Analysis (MEA) and Maintenance Material Management (3M) field data. Data are required for each weapon replaceable assembly (WRA) and each of the 500 shop replaceable assemblies (SRA).

Life cycle support costs are the sum of fixed and variable costs required to operate and support the systems during their operating phase. Fixed costs such as maintenance of technical publications, facility space costs, and some depot facility costs, are relatively independent of the operating system's demands for resources. The larger portion of the life cycle support costs are variable and depend on the level of resources required to maintain the systems. The resource demand depends on the system's demand for maintenance; in other words the system reliability. These support resources (primarily replenishment spares and labor) costs are calculated and summed to determine the variable support costs.

The Hughes Life Cycle Cost model has, for the purposes of this study, been utilized only to determine a base line from which an electromagnetically focused TWT and an equally well designed permanent magnet focused TWT may be compared with respect to system life cycle improvement. The problem then was to 1) generate an accurate data base, 2) establish the system's failure rate, 3) eliminate the solenoid and solenoid power supply failures from the data base, 4) recalculate the system's failure rate, and 5) compare the failure rates for improvements.

These data indicate a permanent magnet focused TWT would improve the AWG-9 WCS failure rate by 6% when compared to the existing electromagnetically focused TWT. This assumes both tubes have equal thermal design margin and perform equally with the same operating parameters. Under these circumstances, it can be concluded that 1) a properly designed electromagnetically focused TWT (and the attendant power supply) may be utilized without significant impact upon system reliability, and 2) some system reliability improvement may be achieved when utilizing permanent magnet instead of electromagnetic focusing in the TWT design. While the first conclusion is certainly true, the second conclusion becomes suspect with regard to the initial assumptions.

Typically, solenoid focused units incorporate copper as the base material for the slow wave structure while a considerable amount of iron is used in PM focused TWTS. In order to achieve the same thermal margin within the slow wave structure, the cathode voltage in the PM focused TWT may have to be increased to maintain proper focusing. Increased voltage requires greater design complexity in the power supply and electron guns. Consequently, system reliability may decrease and the apparent advantage achieved when selecting a PM focused TWT become negated.

The impact, at the system level, of removing all TWT failures associated with the focusing structure, i.e., the solenoid, turned out to be small.

This is probably attributed to the particular system chosen as the vehicle for the analysis.

In this system the TWT is considered to be at the component level within a major subsystem. When calculating the impact of changes in the TWT on the system life cycle, the tube failure rate must first be adjusted to exhibit the effect of the candidate improvement. This new TWT failure rate must be reflected as a change in the failure rates of first the subsystem and then finally the complete system.

In systems which utilize lower frequencies and/or higher power levels the size and complexity of the TWT may be such that the tube is elevated to the subsystem level. In this case, significant changes in the TWT failure rates would reflect more directly upon the system life cycle data.

The size and weight of a TWT are generally inversely related to the frequency. Typically, except for handling considerations, the size and weight of a unit should not impact the system life cycle operation. This should be true for all well designed TWTs regardless of the focusing mechanism employed.

The complexity and hence cost associated with electromagnetically focused TWTs is in general greater than that associated with permanent magnet focused units. Unfortunately, as the frequency, power levels, and duty cycle increase, the thermal stresses on the slow wave structure also increase. In order to prevent catastrophic circuit damage, greater control of the electron beam must be achieved. At some point, the heat being generated by beam power impinging upon the TWT circuit will exceed the metal's thermal capabilities. When this occurs, the use of electromagnetic rather than permanent magnet focusing (at least of the periodic type) becomes mandatory.

#### 4.0 CONCLUSIONS

At the present time, the principal factor limiting the average power capability of high peak power PPM focused traveling wave tubes is the thermal dissipation of beam interception power by the circuit as a result of RF defocusing of the beam under drive. Some improvements in the thermal capability of circuit structures is possible; however, achieving maximum power capability ultimately requires that steps be taken to improve the quality of the beam focusing under drive.

Results of this study indicate that significant improvements in the beam defocusing should be obtainable by maximizing the rms focusing field consistent with maintaining acceptable beam focusing parameters and by choosing a beam perveance that will allow partial confinement of the beam with at least 1.2 - 1.4 times Brillouin, assuming a modest beam filling factor of .50 - .55 times the tunnel diameter. Calculated performances indicate that similar characteristics may also be possible without confinement by maintaining a high focusing field and allowing the beam to become even smaller in diameter. The principal factors for preventing RF defocusing are high rms focusing fields and low space charge beams. Limitations on perveance and beam size ultimately depend upon the ability of the beam and circuit to interact properly at acceptable RF levels and upon system voltage limitations.

Advantages for using at least some degree of beam confinement are better containment of thermal electrons and a more laminar and better structured beam that might have less tendency towards disorder in the presence of defocusing forces.

The present study points out the complexities of the problem. It is questionable that current computer software capability exists for determining complete tube performance including RF beam defocusing in the

PRECEDING PAGE NOT FILMED  
BLANK

presence of confined PPM focusing fields taking into account thermal electrons and the axial slowing down of electrons as the result of transverse energies generated by the focusing fields. The attempt in this study has been to look at a few of these problems separately in order to obtain indications of the directions in design that would be beneficial to improving performance beyond that which is currently obtained.

APPENDIX A  
LAMINAR BEAM MODEL INCLUDING AXIAL FORCES

In the standard paraxial treatments of PPM focusing<sup>2,4-7</sup> only a radial force balance within the beam is considered. The omission of any axial forces results in the implicit assumption that the entire electron beam possesses a constant drift velocity in the axial direction. Mathematically the resulting focusing equation, e.g., Harker's Eq. (12), remains stable for all finite values of parameters, at least for those parameters representative of any normal physical beam and focusing condition. In contrast to this, one of the effects of including axial force terms in the focusing expression is to introduce instabilities into the PPM focusing equation similar to those that are observed experimentally. (Interestingly, as various treatments point out, with the absence of any space charge in the beam and for no cathode flux the standard equation reduces to a form of Mathieu Equation that also exhibits focusing instabilities typical of measured performance. The full significance of this is not entirely clear since under these conditions the mathematical model no longer represents a physical beam. It actually results in the special case of no forces present to prevent electrons from crossing the axis. It does tend to substantiate observations that the focusing stability of PPM beams is primarily a lens phenomenon and that it is relatively independent of actual beam parameters.)

In addition to forming a more realistic model, in the case of immersed or confined beam flow (i.e., with finite values of cathode flux) it is even more important that the effects of axial forces be included when there are focusing regions involving flux reversals. The resulting changes in total flux linked by electrons as they enter the reversed field regions can lead to large amounts of rotational energy being

generated at the expense of longitudinal drift energy. The assumption of constant drift velocity may then represent a significant error in the analysis.

The following paraxial ray treatment of the beam envelope, including the effects of axial forces, was utilized in the present study for determining the principle characteristics associated with confined PPM flow. The model is non-relativistic and assumes that the flow is laminar. Solutions to the final pair of focusing equations were obtained from a digital computer program run interactively on time share.

In this treatment the radial force balance is obtained in the usual manner<sup>2</sup> with the exception that the beam velocity,  $\dot{z}$ , is no longer considered constant, but varies both as a result of the interaction of rotational electron velocities with radial components of magnetic field and from variations in potential along the beam caused by changes in the beam envelope geometry and/or from charge density changes resulting from variations in beam velocity. The basic force equations that are integrated numerically by computer are

$$\ddot{r} = r\dot{\theta}^2 - n B_z r\dot{\theta} + \frac{n I_o}{2\pi\epsilon r\dot{z}} \quad (30)$$

for the radial force balance relationship, and

$$\ddot{z} = n B_r r\dot{\theta} + n \frac{\partial V}{\partial z} \quad (31)$$

for the axial force equation.

In the above expressions  $\eta$  is the electron charge-to-mass ratio and  $\dot{\theta}$  is the electron rotational angular velocity which, according to Busch's theorem, can be expressed as

$$\dot{\theta} = \frac{\eta}{2\pi r^2} (\psi - \psi_c) \quad (32)$$

In this last expression  $\psi_c$  is the initial flux linkages of an electron as it leaves the cathode surface and  $\psi$  is the flux linkages at the point where  $\dot{\theta}$  is being evaluated.

Since numerical integration is employed in the computer program, the analysis is not limited to sinusoidal focusing fields but may optionally use the actual field forms associated with specific focusing geometries.

It is clear that when  $\ddot{z} = 0$  (no axial force terms) then  $\dot{z} = u_o$  (i.e., a constant value for the beam velocity) and the focusing equation reduces to the standard form found throughout the literature.

It is convenient to define the following set of dimensionless parameters for use in characterizing various cases:

Magnetic Field parameter,

$$\alpha = \left( \frac{\eta B_{rms}}{2k u_o} \right)^2 = \frac{\omega_L^2}{\omega^2} \quad (33)$$

Space Charge parameter,

$$\beta = \frac{\eta I_o}{2\pi r_o^2 \epsilon u_o (k u_o)^2} = \frac{\omega_p^2}{2\omega^2} \quad (34)$$

Cathode flux (immersion) parameter

$$K = \frac{B_c^2 r_c^4}{B_{rms}^2 r_o^4} = \frac{\psi_c^2}{\psi_{rms}^2} \quad (35)$$

Axial force parameter

$$\gamma = (kr_o)^2 \quad (36)$$

where

$$k = \frac{2\pi}{L}$$

L = magnetic period and

$$\omega = k u_o$$

The first three parameters are similar to those used in the literature with the exception that with complex field shapes it is more meaningful to define the magnetic focusing field in terms of rms rather than peak values of field. Thus,  $\omega_L$  becomes the rms Larmor frequency and  $\psi_{rms}$  the rms value of flux linkages. The parameters  $r_o$  and  $u_o$  can be considered to be completely arbitrary normalization factors, however, to avoid ambiguities resulting from complex forms of velocity variation and beam ripple it is best to choose them, respectively, to be the equilibrium radius and axial velocity that one would normally assign to a DC solenoid focused beam having the same rms focusing field and cathode flux linkages as the PPM beam being analyzed. The actual average radius and velocity may differ slightly from these values when the focusing is finally balanced in a PPM configuration.

It may be of interest to note that with the above definitions

$$\frac{\lambda_p}{L} = \frac{1}{\sqrt{2\beta}} \quad (37)$$

and

$$\frac{\lambda_{sc}}{L} = \frac{1}{\sqrt{4\alpha - 2\beta}} \quad (38)$$

where  $\lambda_p$  is the usual plasma wavelength that would be associated with the charge density of a uniform beam and  $\lambda_{sc}$  is the scallop wavelength associated with the natural oscillation frequency of the beam envelope about its equilibrium position. For these relationships to hold,  $\alpha$  and  $\beta$  must be normalized using the correct velocity and equilibrium radius for  $u_o$  and  $r_o$ .

When Equations (30) and (31) are normalized by means of the above defined parameters they become

$$\ddot{y} = 2\alpha \left[ \frac{K/2}{y^3} - y f^2(x) \right] + \frac{\beta}{yx} \quad (39)$$

$$\ddot{x} = 2\alpha\gamma f'(x) \left[ y^2 f(x) - \sqrt{K/2} \right] + \beta\gamma \frac{\partial \left[ \frac{\ln \left( y \frac{r_o}{a} \right)}{x} \right]}{\partial x} \quad (40)$$

where,

$$\begin{aligned}y &= r/r_o & \tau &= \omega t \\x &= kz & \ddot{y} &= \ddot{y}/\omega^2 \\x' &= z/u_o & \ddot{x} &= k\ddot{z}/\omega^2 \\r_o/a &= \text{beam filling factor}\end{aligned}\tag{41}$$

Note that time derivatives in the normalized expressions are with respect to the normalized time,  $\tau = \omega t$ . The function,  $f(x)$ , describes the variation of the axial magnetic field with normalized distance and  $f'(x)$  is the derivative of this function with respect to the variable,  $x$ . The derivative appears as the result of assuming that in a paraxial ray analysis the radial magnetic field can be accurately expressed in terms of the derivative of the axial magnetic field as follows:

$$B_r = -\frac{r}{2} \frac{dB_z}{dz}\tag{42}$$

In the above expressions the field shape function,  $f(x)$ , is normalized to have an rms value of 0.70711 .... such that for sinusoidal fields it is simply replaced by  $\cos x$  and its derivative by  $\sin x$ .

In arriving at the expression shown in Equation (40), the axial change in potential appearing in Equation (31) was assumed to result from changes in the space charge depressed potential at the beam edge. Thus, when this term is included it is necessary to specify the filling factor of the beam in the beam tunnel. Normally the effect of this term is small in comparison to the magnetic term.

APPENDIX B  
BASELINE EXAMPLES OF HIGH POWER TUBE DESIGNS

The following tubes represent examples of 100 kw and greater designs in the 3 - 10 GHz frequency range. These tubes formed a baseline for the present investigation in terms of typical design parameter ranges and performance levels to associate with modern high power designs. The 559H, 584H, and the 8716H are all PPM focused high power TWT's with power outputs ranging between 120 kw and 350 kw. The 635H is a solenoid focused tube with a power output of 165 kw. None of these tubes are currently focused with rare earth magnets. The 635H solenoid focused tube employs a significant amount of cathode flux for maintaining a high level of beam control.

559H HIGH POWER TWT

The Hughes 559H is a high power, S-Band traveling wave tube, which provides 125 kw peak and 10 kw average power output. It utilizes the coupled cavity interaction circuit with integral periodic permanent magnet focusing.

The 559H uses Alnico 8 magnets. The circuit pole pieces are directly liquid cooled by cross-channels to obtain the high average power with the PPM focusing. The beam is provided by a "shadow grid" modulating electron gun. To obtain the high gain, the circuit is severed into three separate cascaded sections.

A photograph of the completed tube is shown in Figure 64. It uses a WR 284 waveguide output window and a type N coaxial input. The coaxial input leaves more room available for magnetic material at the input focusing lens than waveguide input would. The tube is cooled using

E1144

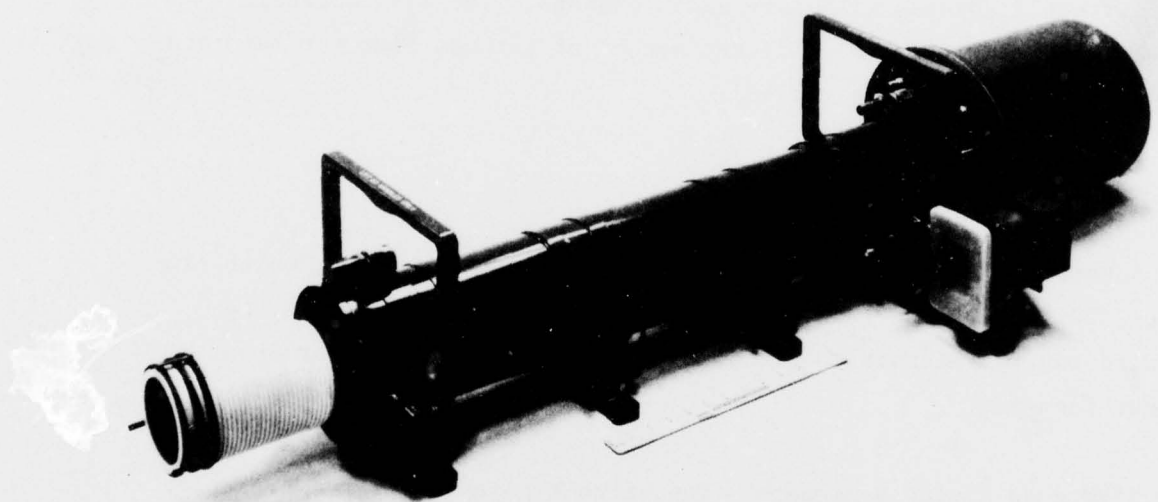


Figure 64 559H traveling wave tube.

demineralized water or an ethylene glycol and water mixture depending upon environmental temperature requirements. It weighs 185 pounds.

Curves of saturated gain and power output for the 559H are shown in Figure 65. A summary of the major characteristics of the tube are as follows:

Frequency Range	3.1 to 3.5 GHz
Bandwidth	400 MHz
Gain at Saturation	50 dB Minimum
Power Output (peak)	125 kw
Power Output (average)	10 kw
Duty Cycle	0.08
Pulse Width	125 Microseconds
Cathode Voltage (dc)	-43 kV
Cathode Current (peak)	17 amperes
Grid Bias Voltage	-800V
Grid Pulse (relative to cathode)	+900V
Body Voltage	Ground
Body Current	2.5 amperes
Collector Voltage	-17 kV
Weight	185 pounds max.
Length	50 inches
Cooling (ethylene glycol/water)	
Body - 4.0 gpm at 20 psi drop	
Collector - 8.0 gpm at 15 psi drop	
RF Connector	
Input - Type N coaxial fitting	
Output - CPR 28HF waveguide flange	
Focusing (PPM)	900 gauss (peak)

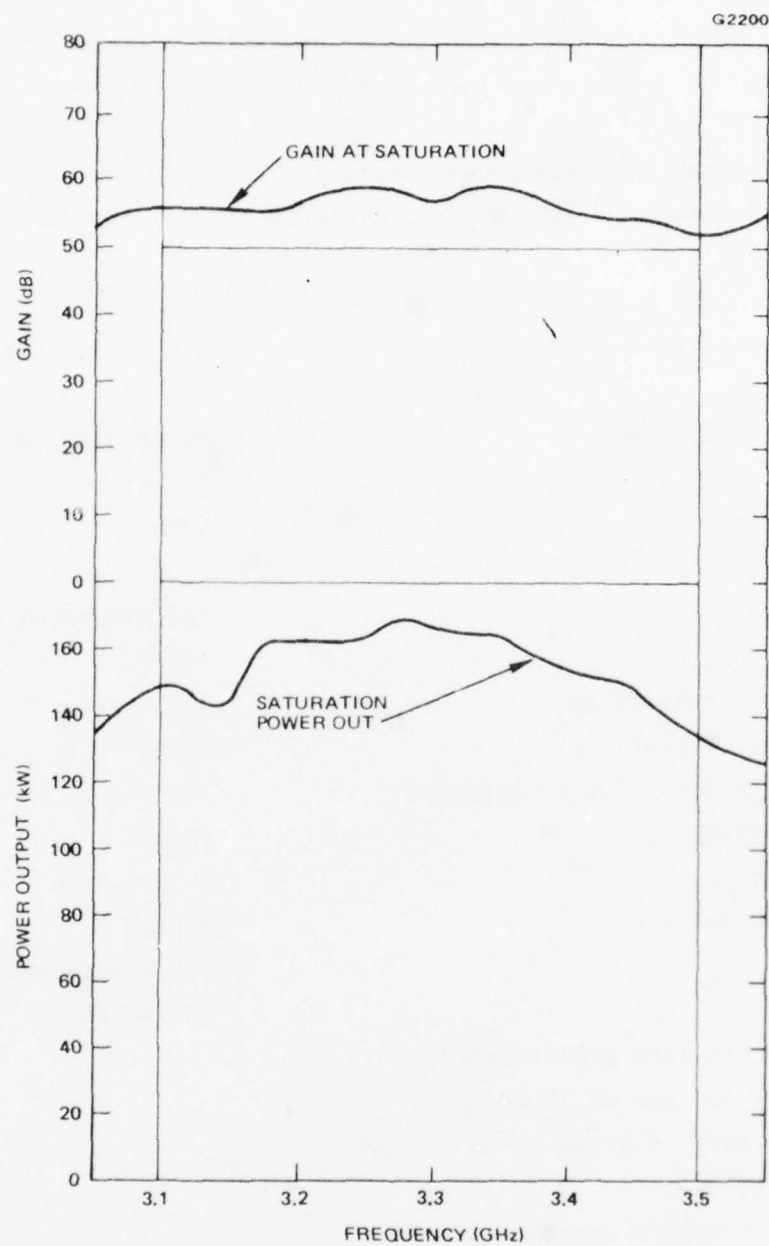


Figure 65 Gain and power output of 559H, Serial No. 6 at a cathode voltage of -43 kV and beam current of 17 amperes.

### 584H HIGH POWER TWT

The 584H is a high power, periodic permanent magnet focused S-Band traveling wave tube. Mechanically it is very similar to the 559H. However, it is designed for higher peak power and lower gain. A photograph of the completed tube is shown in Figure 66. The gridded electron gun is the same as that used on the 559H, but it operates in dielectric oil in this application. Focusing is with Alnico 8 magnets, and cross-channel liquid cooling is used to allow a 3 percent duty cycle corresponding to 10 kilowatts average power output.

A curve of saturated output power for the 584H is shown in Figure 67. Drive power for this data is between 50 and 55 dbm.

A summary of the major operating characteristics of the tube are as follows:

Frequency Range	2.76 to 3.00 GHz
Bandwidth	240 MHz
Gain at Saturation	28 dB
Power Output (peak)	300 kw minimum
Power Output (average)	9 kw
Duty Cycle	0.03
Cathode Voltage (dc)	-59 kV
Cathode Current (peak)	26A
Grid Bias Voltage	-700V
Grid Pulse Voltage (relative to cathode)	1250V
Grid Current (peak)	40 ma
Body Voltage	Ground
Body Current	4.0A
Collector Voltage	-24 kV

E1145

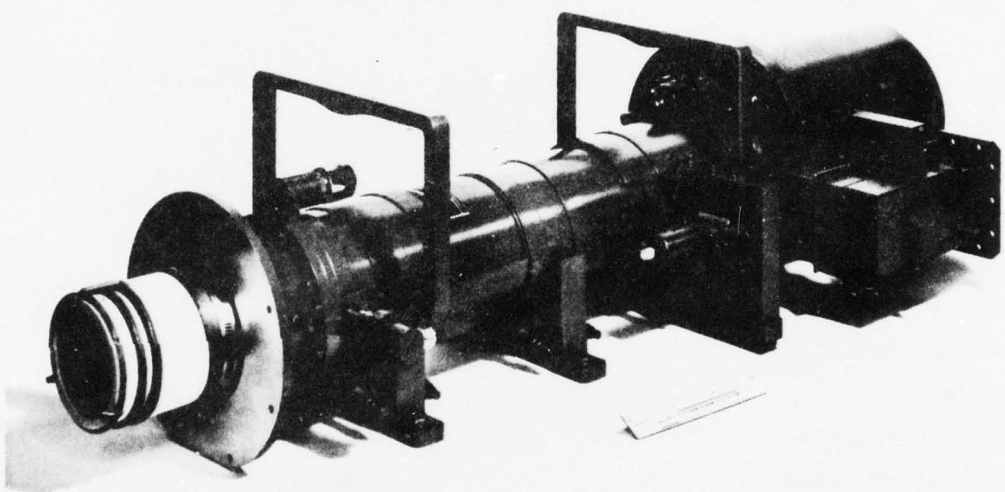


Figure 66 584H traveling wave tube.

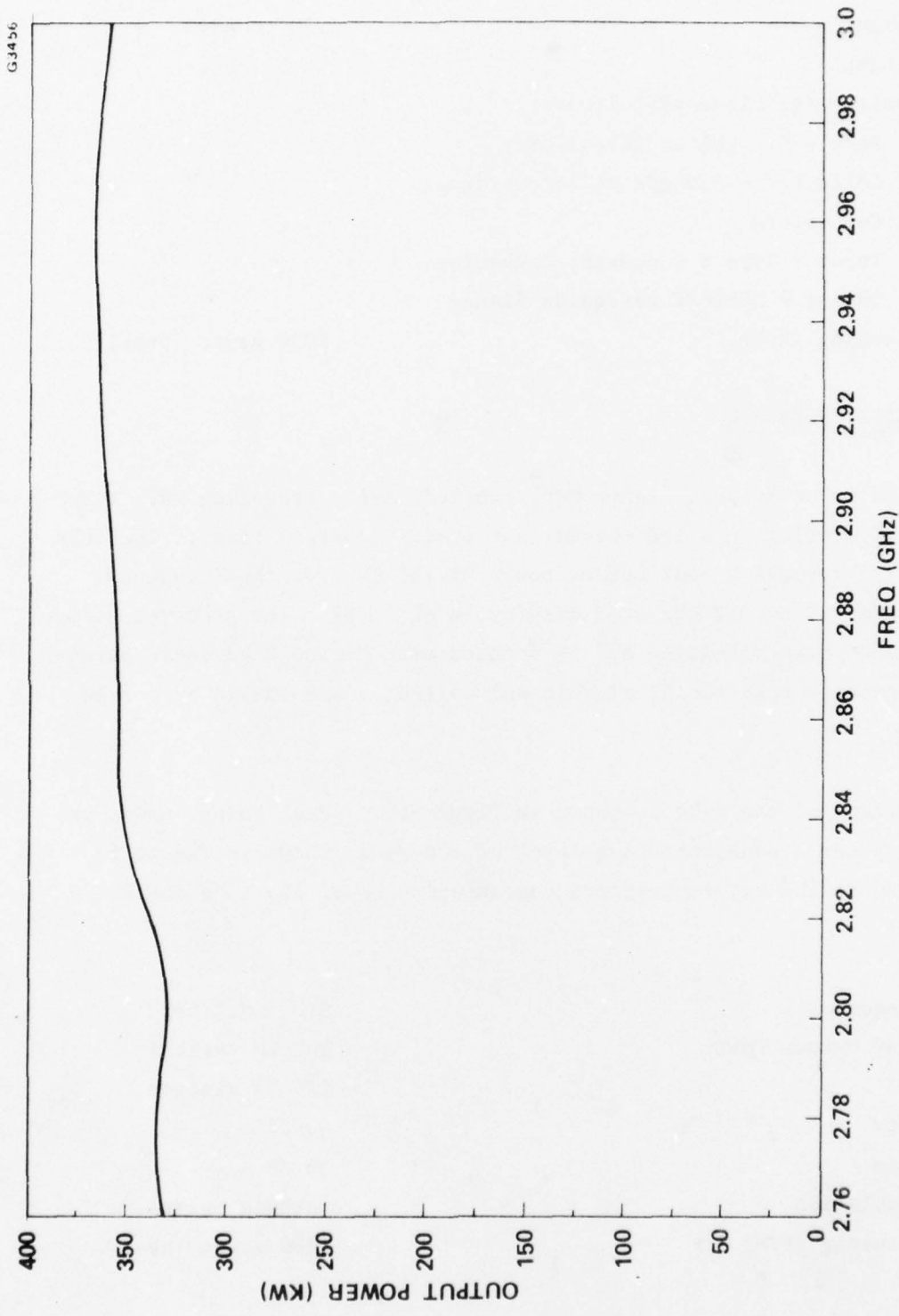


Figure 67 Saturated power output of the 584H TWT.

Weight	150 pounds
Length	40.5 inches
Cooling (ethylene glycol/water)	
Body	- 4.0 gpm at 20 psi drop
Collector	- 8.0 gpm at 15 psi drop
RF Connectors	
Input	- Type S C coaxial connector
Output	- CPR284F waveguide flange
Focusing (PPM)	1050 gauss (peak)

#### 8716H HIGH POWER TWT

The 8716H is an X-band, high-power, coupled-cavity traveling wave tube for incorporation in a land-based, air traffic control radar. The tube typically provides a peak output power of 140 kW over the frequency range from 9.0 to 9.2 GHz at a duty cycle of 0.25%. The electron beam is cathode-pulse modulated and is focused with Alnico 8 periodic permanent magnets. Both the RF circuit and collector are cooled by forced air.

A photograph of the tube is shown in Figure 68. Peak output power vs frequency for a constant drive level of 100 mw is shown in Figure 69. A summary of the major operating characteristics of the tube are as follows:

Frequency	9.0 - 9.2 GHz
Peak Output Power	140 kW typical
	120 kW minimum
Duty	0.0025
Gain	56 dB
Modulation	Cathode pulsed
Focusing (PPM)	1800 gauss (peak)

E1146

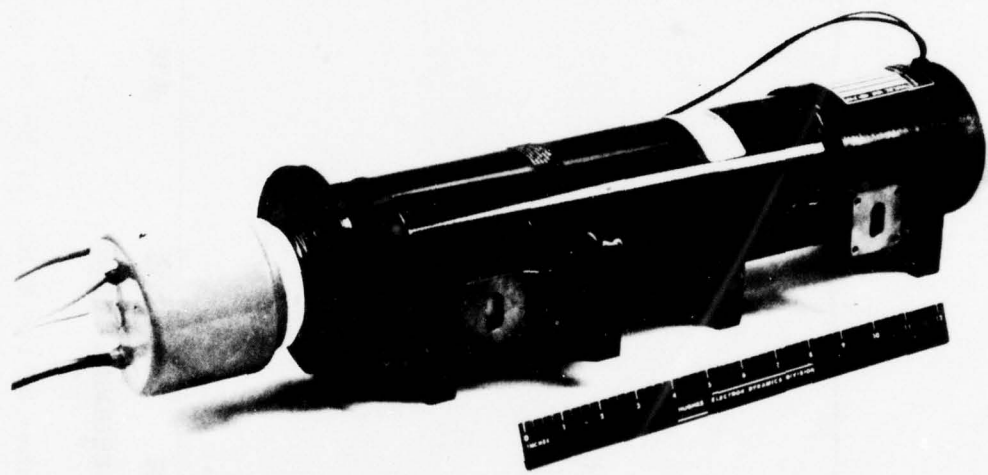


Figure 68 8716H traveling wave tube.

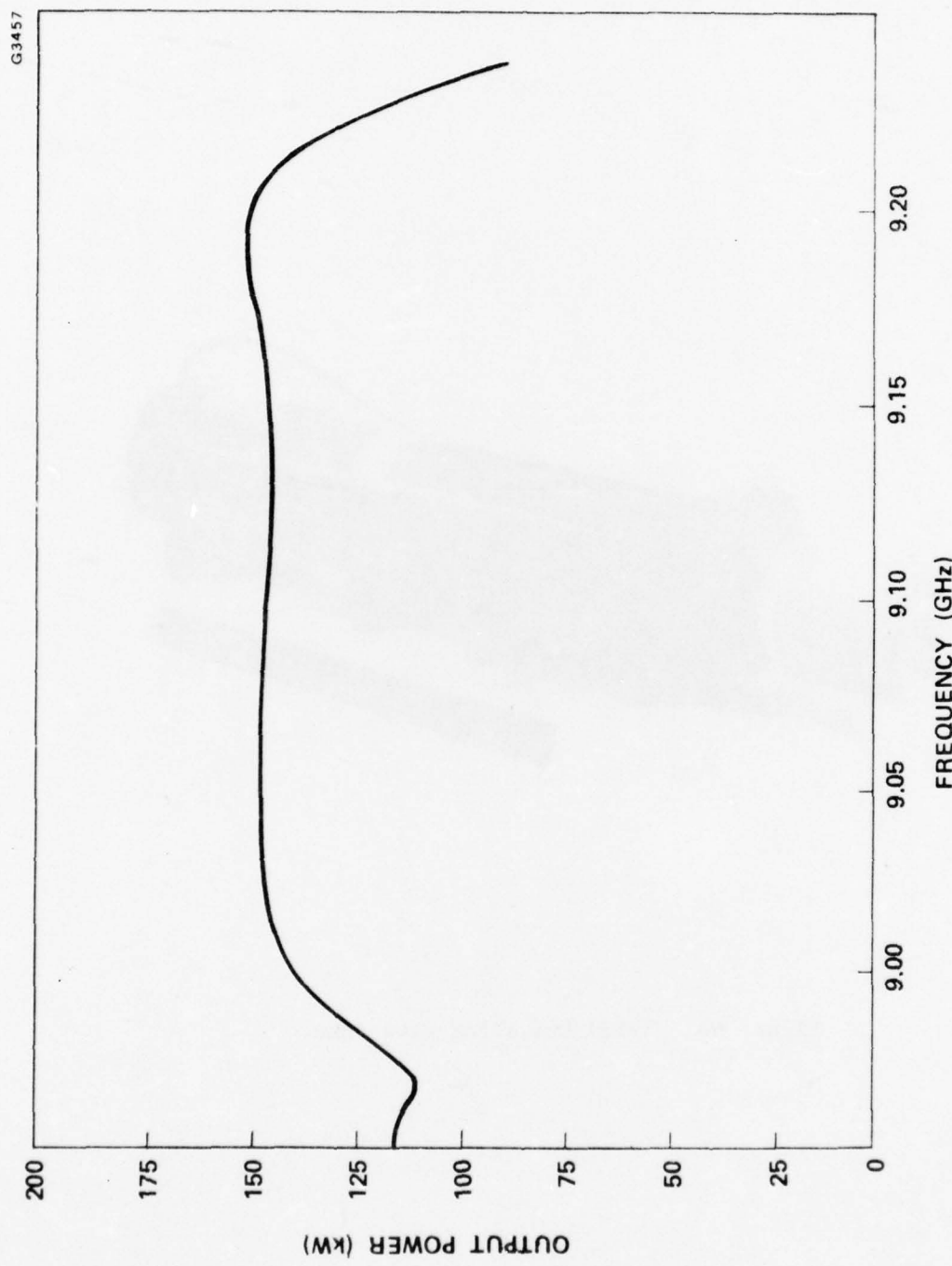


Figure 69 Output power of the 871bH for 100 mW constant drive.

Cooling

Air flow

100 CFM

Pressure drop

5 inches of water

Size

Diameter

5 inches

Length

24 inches

Weight

35 lbs

Cathode Voltage

-43 kV typical

Cathode Current

13.5A typical

635H HIGH POWER TWT

The Hughes 635H is a high power, high gain coupled-cavity C-Band amplifier for a production Navy radar program. It uses a solenoid for beam focusing, has a shadow gridded electron gun, and is water cooled.

A photograph of the 635H in its focusing solenoid is shown in Figure 70. The tube alone weighs 55 pounds. The solenoid weighs 135 pounds and takes 5 kW of solenoid power.

Power output data for the 635H is presented in Figure 71. A summary of the major operating characteristics of the tube is as follows:

Frequency Range

5.4 to 5.85 GHz

Bandwidth

450 MHz

Gain at Saturation

48 dB

Power Output (peak)

175 kW min.

Power Output (average)

7 kW

Duty Cycle

0.04

Cathode Voltage (dc)

-48.5 kV

Cathode Current (peak)

17A

Grid Bias Voltage

-1000V

E1147

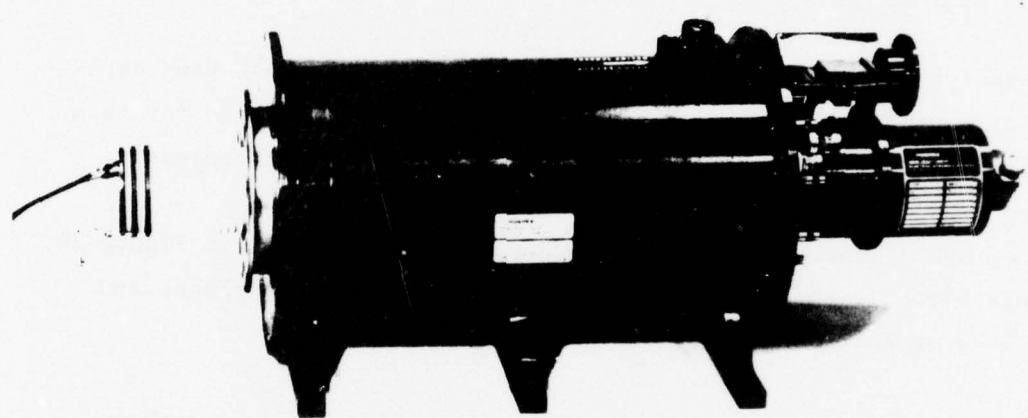


Figure 70 635H solenoid focused traveling wave tube.

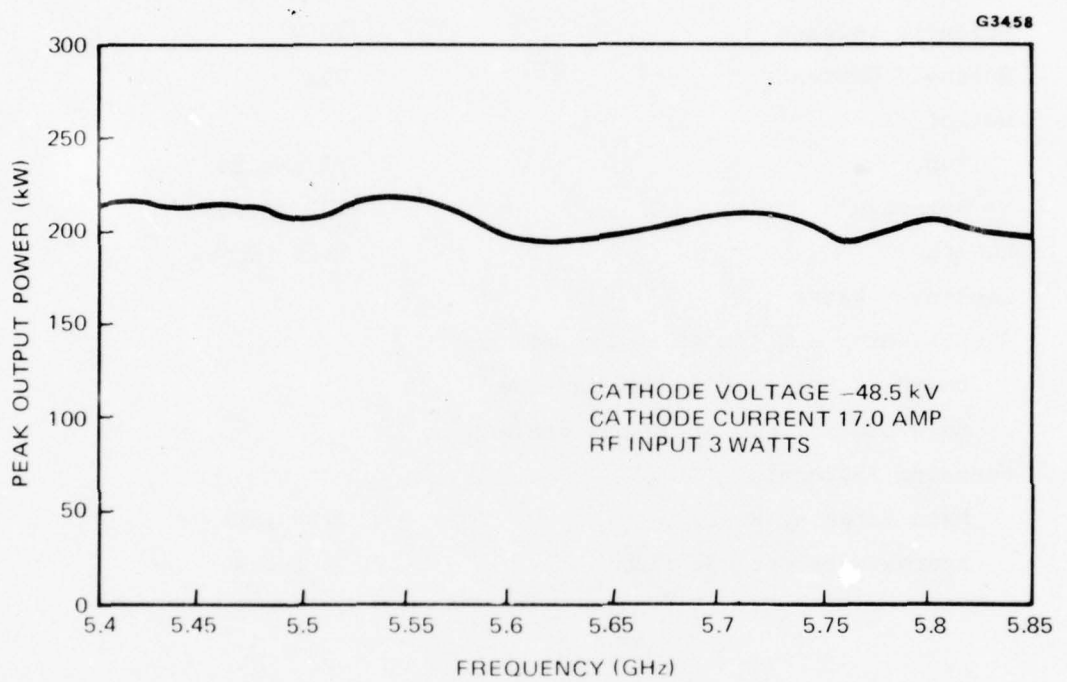


Figure 71 Typical output power characteristic of the 635H.

Grid Pulse Voltage (relative to cathode)	+900V
Grid Current (peak)	30 ma
Body Voltage	Ground
Body Current	0.4A
Collector Voltage	Ground
Solenoid Voltage	200V
Solenoid Current	25a
Weight	
Tube	55 pounds
Solenoid	135 pounds
Length	34.5 inches
Cooling - Water	
Collector - 6 gpm at 45 psi maximum	
Body - 2.5 gpm at 30 psi maximum	
Solenoid - 2 gpm at 30 psi maximum	
Focusing (Solenoid)	
Main Focusing Field	2100 gauss
Approximate Cathode Flux	55 gauss

APPENDIX C  
FORCED CONVECTIVE HEAT TRANSFER COEFFICIENTS  
FOR POLE PIECE COOLANT CHANNELS

The following empirically developed formulations are recommended for defining coolant flow heat transfer coefficients in the pole piece curved rectangular channels. Equations describing turbulent and laminar flow are presented. It is recommended that the currently employed linearization procedure be used in defining heat transfer coefficients in the transition regime. Development of the equations is presented in the Appendix.

Turbulent Flow:

The average peripheral heat transfer coefficient for turbulent flow in the curved channel of the pole pieces is described by<sup>8</sup>

$$h_{avg} = h_s [R_e_{d_H f}]^{(d_H/D_c)^2} 0.05$$

where,

$$h_s = 0.023 \frac{k_f}{d_H f} R_e_{d_H f}^{0.8} p_{r_f}^{0.4} \left(\frac{\mu_b}{\mu_w}\right)^{0.14}$$

$k_f$  = thermal conductivity of the fluid

$R_e_{d_H}$  = Reynolds number based on hydraulic diameter  
 $f$

$P_r_f$  = Prandtl number

$\mu$  = absolute viscosity of the fluid

Subscripts for fluid properties:

$f$  = evaluated at a film temperature

$$T_f = \frac{T_b + T_w}{2}$$

$b$  = bulk temperature of the fluid

$w$  = wall or surface temperature

$d_H$  = channel hydraulic diameter

$D_c$  = diameter of curvature of flow channel

Laminar Flow:

The average laminar flow coefficient for the curved pole piece channel is<sup>8</sup>

$$h_{avg} = 0.26 \frac{k_f}{d_H} P_r_f^{1/3} R_e_{d_H}^{1/3} \left\{ \frac{1}{1 - [(B)]^{2.22}} \right\}^{1/3} \left( \frac{\mu_b}{\mu_w} \right)^{0.14}$$

where,

$$(B) = 1 - \left( \frac{11.6}{Re \frac{d_H}{f} \sqrt{\left( \frac{d_H}{D_c} \right)}} \right)^{0.45}$$

All other terms are as defined previously.

Transition from Laminar to Turbulent Flow:

I. Seban and McLaughlin<sup>8</sup> and Ito<sup>9</sup>:

(a) Tube curvature tends to elevate the  $Re$  at which transition occurs. However, their results were obtained with continuous  $360^\circ$  curved tubes and not with  $64^\circ$  segments having abrupt  $90^\circ$  turns at entrance and exit sections as found in the pole piece coolant channels.

II. Senecal; Rothfus; Lindgren; Mauer; et. al.<sup>13</sup>:

(a) Turbulence in straight tube begins at:

$Re \approx 1500$  Mauer

$Re \approx 2100$  Senecal

and is complete at

$Re \approx 2800$  Senecal

$Re \approx 3300$  Lindgren

Generally, entrance conditions are the determining factor for the onset of turbulent flow in a channel.

(b) For pole piece channels use

End of laminar  $Re \approx 2000$

Fully turbulent  $Re \approx 3000$

Transition  $Re \approx 2000 \rightarrow 3000$ , a linearized evaluation between laminar and turbulent.

#### GENERAL DISCUSSION POLE PIECE CONVECTIVE HEAT TRANSFER

In general for flow in the rectangular channels of the pole pieces the following observations are applicable.

##### Noncircular Flow Cross Sections:

The friction factor for turbulent flow in noncircular ducts has been studied rather extensively. It has been well established, for fully developed turbulent flow in smooth tubes of a large variety of cross section shapes, that the usual Nikuradse equation:

$$\frac{1}{(f)^{1/2}} = 4.0 \log [Re(f)^{1/2}] - 0.40$$

is valid for calculating the pressure drop if the tube diameter,  $D$ , is replaced by the equivalent hydraulic diameter,  $d_H$ , where:

$$d_H = 4 \frac{(\text{cross sectional area for flow})}{(\text{wetted perimeter})}$$

$$Re = \frac{d_H U \rho}{\mu}$$

where  $U$  = average fluid velocity

and:

$$-\frac{\Delta P}{\Delta x} = 4 f \frac{U^2 \rho}{2 g_c d_H}$$

for a rectangular cross section with sides of length  $a$  and  $b$ ,

$$d_H = 4 \frac{ab}{2(a+b)} = \frac{2ab}{a+b}$$

A theoretical method for calculating the velocity profile for non-circular flow passages was developed by Deissler and Taylor.<sup>14</sup> They neglect the secondary flows found by Nikuradse which consist of flow toward the corners of the passage and away from the sides. They assume that the universal velocity for circular tubes applies for lines normal to the duct wall. While the method can give insight into the velocity distribution, it is tedious to apply and its use for calculating the friction factor gives no better accuracy than the use of the much simpler hydraulic diameter.

While reasonable estimates of the friction factor for noncircular ducts can be made, such is not the case with the heat transfer coefficient. Neither the use of the hydraulic diameter nor the theoretical technique of Deissler and Taylor has been wholly satisfactory. The use of the hydraulic diameter has received the most attention. For example, the

McAdams equation gives:

$$N_u_{avg} = 0.023(Re)_b^{0.8} (Pr)_b^{0.4}$$

In general, the experimental data for noncircular ducts (excluding annuli) fall below this equation. Based on,<sup>15</sup> as shown in Figure 72, for square cross sections, the available experimental data give values of the average heat transfer coefficient about 75 to 90 percent of circular tube values from McAdams equation. For rectangular cross sections having aspect ratios of 3 to 40, the data give values of  $h_{ave}$  approximately 55 to 95 percent of circular tube values. In addition, the data of Levy, et. al<sup>16</sup> for large aspect ratios (~25) indicate that the heat transfer coefficient on the short side may be 15 to 30% of that for the long side.

#### Curvature of Channel:

When a fluid passes through a curved tube, the centrifugal force causes the fluid to flow at a higher velocity in the region of the wall corresponding to the outer radius of curvature. The expected result is a peripheral variation of the local heat transfer coefficient such that it is greater for the wall surface at the outside radius of curvature than for the surface at the inside radius of curvature. Data obtained by Seban and McLaughlin<sup>8</sup> for water and by others for hydrogen<sup>17</sup> and N<sub>2</sub>O<sub>4</sub><sup>18</sup> tend to confirm this effect. Only an empirical theory exists for the average peripheral heat transfer coefficient for flow in tubes. For flow in a channel consisting of two concentric surfaces, Kreith<sup>19</sup> has developed a momentum analogy theory which is in agreement with the above qualitative statements. In general, the average peripheral heat transfer coefficient for a curved tube is greater than for a straight tube as cited by McAdams.<sup>11</sup>

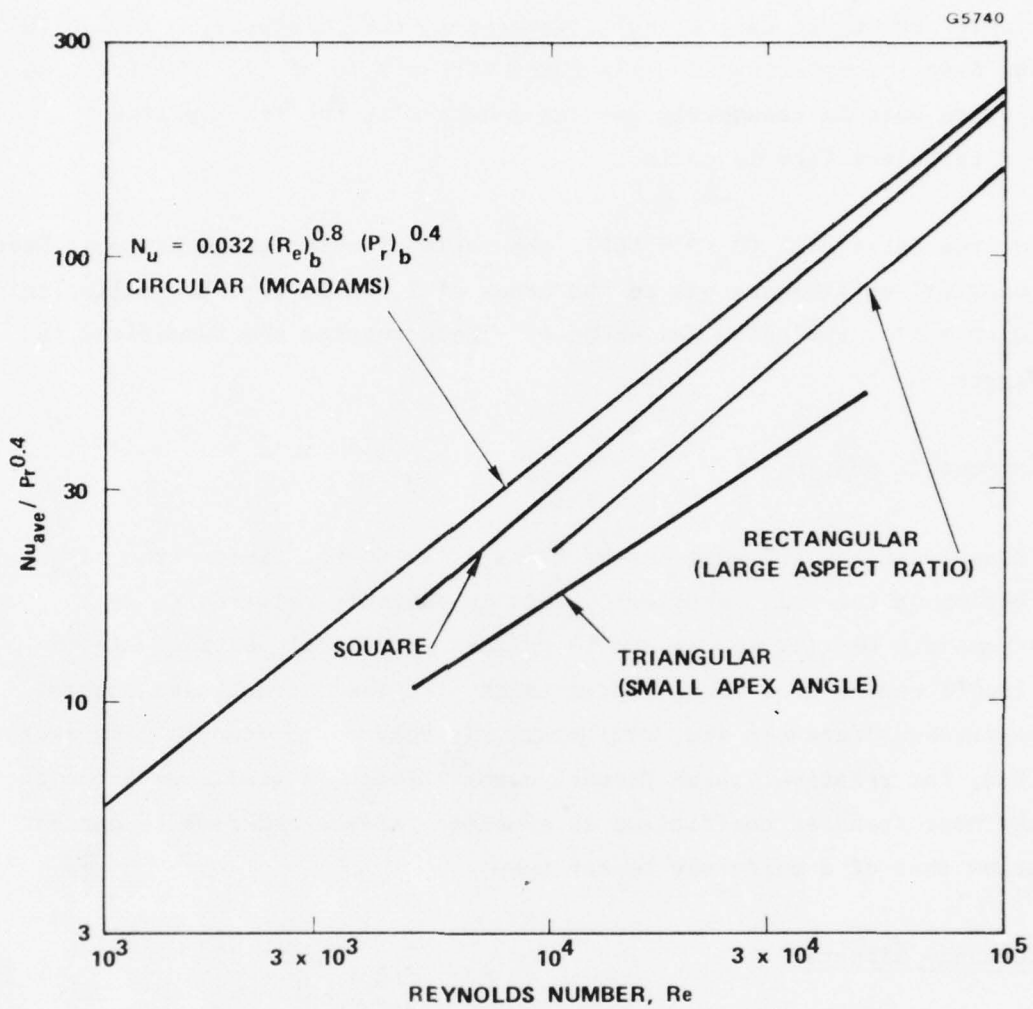


Figure 72 Effect of noncircular flow cross section on heat transfer.

The recent data of Seban and McLaughlin for water were obtained with a single 360-degree coil of coil diameter-to-tube diameter,  $D_c/D$ , of 104 and a coil consisting of 6-1/2 turns with a  $D_c/D$  of 17. The friction factors were in reasonably good agreement with the Ito equation<sup>9</sup> for turbulent flow in coils.

For the large coil ( $D_c/D = 104$ ), the ratio of outer to inner local heat transfer coefficients was on the order of 2, while for the smaller coil ( $D_c/D = 17$ ), the ratio was about 4. These results are summarized in Figure 73.

#### Asymmetric Heating:

In applications the heat may be transferred to the fluid from only a portion of the wall periphery. This is commonly referred to as asymmetric heating as opposed to uniform peripheral heating. As the Prandtl number of a fluid is increased, the laminar sublayer thermal resistance increases and, ultimately, it becomes the controlling factor. Thus, for relatively high Prandtl number fluids, a small reduction in the heat transfer coefficient is expected, of-the-order-of 10 percent below that of a uniformly heated tube.

#### Entrance Effects:

Theoretical approaches to the entrance region effect have been made by Sparrow, et. al.<sup>20</sup> for constant physical properties based on the general energy equation for turbulent flow. If the thermal entrance length is defined as the heated length required to bring the local Nusselt number to within 5 percent of the fully developed value then, as shown in Figure 74, for a Reynolds number of 100,000, the Sparrow analysis gives the following results. The thermal entrance length decreases with increasing Prandtl number from about 13 diameters for

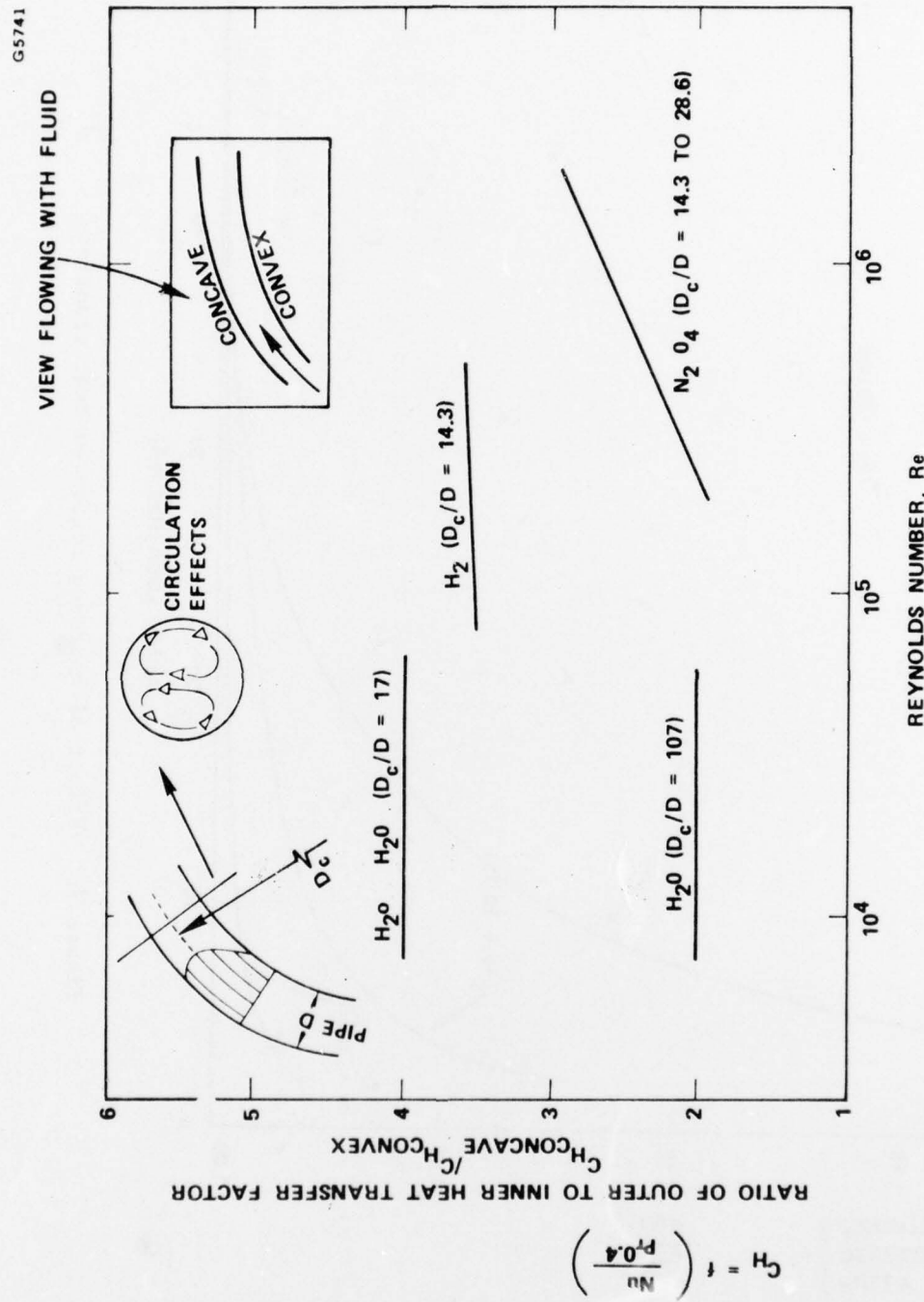


Figure 73 Effect of tube curvature on the peripheral variation of the heat transfer factor.

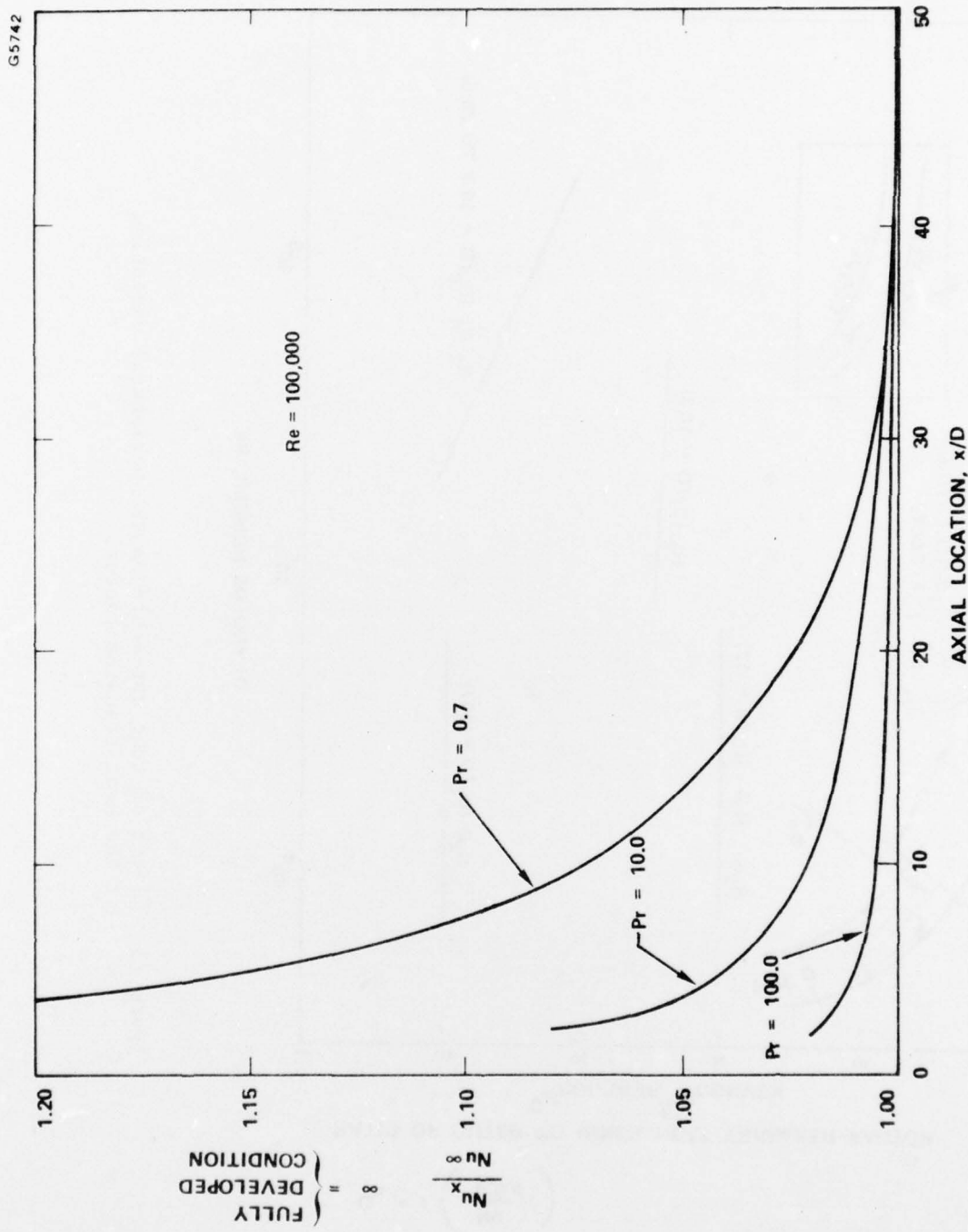


Figure 74 Effect of entrance region on heat transfer.

$Pr = 0.7$  to about 3.5 diameter for  $Pr = 10$ , to less than 1 diameter for  $Pr = 100$ . The effect of Reynolds number is relatively small. Longer entrance lengths may be experienced at high heat-flux conditions or with certain noncircular flow cross sections. The behavior of the local friction factor in the entrance region is analogous to that of the heat transfer coefficient.

Roughness, Channel:

In general, the effect of going from a smooth surface to a rough surface is to increase the friction factor (and, therefore, the pressure drop) by a greater magnitude than the Stanton number (or heat transfer coefficient). For example, from the data of Dipprey and Sabersky <sup>21</sup> for water of  $Pr = 1.20$ , Figure 75 shows the relative increase in the Stanton number compared to the friction factor as the roughness is increased. As seen, with increasing roughness, the relative increase of the Stanton number compared to the friction factor is sharply reduced. At higher Prandtl numbers, however, this reduction becomes less marked with increasing roughness.

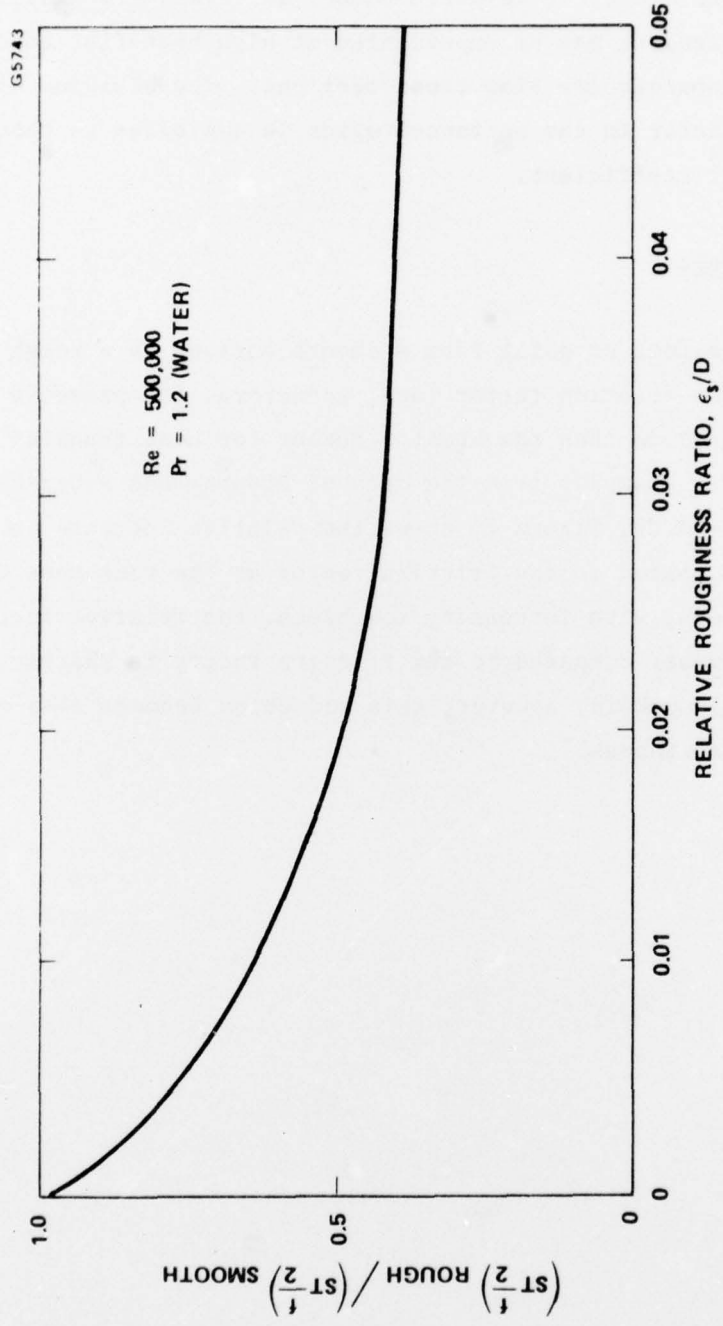


Figure 75 Relative effect of roughness on skin friction and heat transfer.

APPENDIX D  
INITIAL TEMPERATURE ESTIMATES AND MATERIALS DATA

The enclosed estimates of pole piece and spacer temperature profiles were used to obtain the value of thermal conductivity incorporated at the various nodal locations (see Figures 76 through 80).

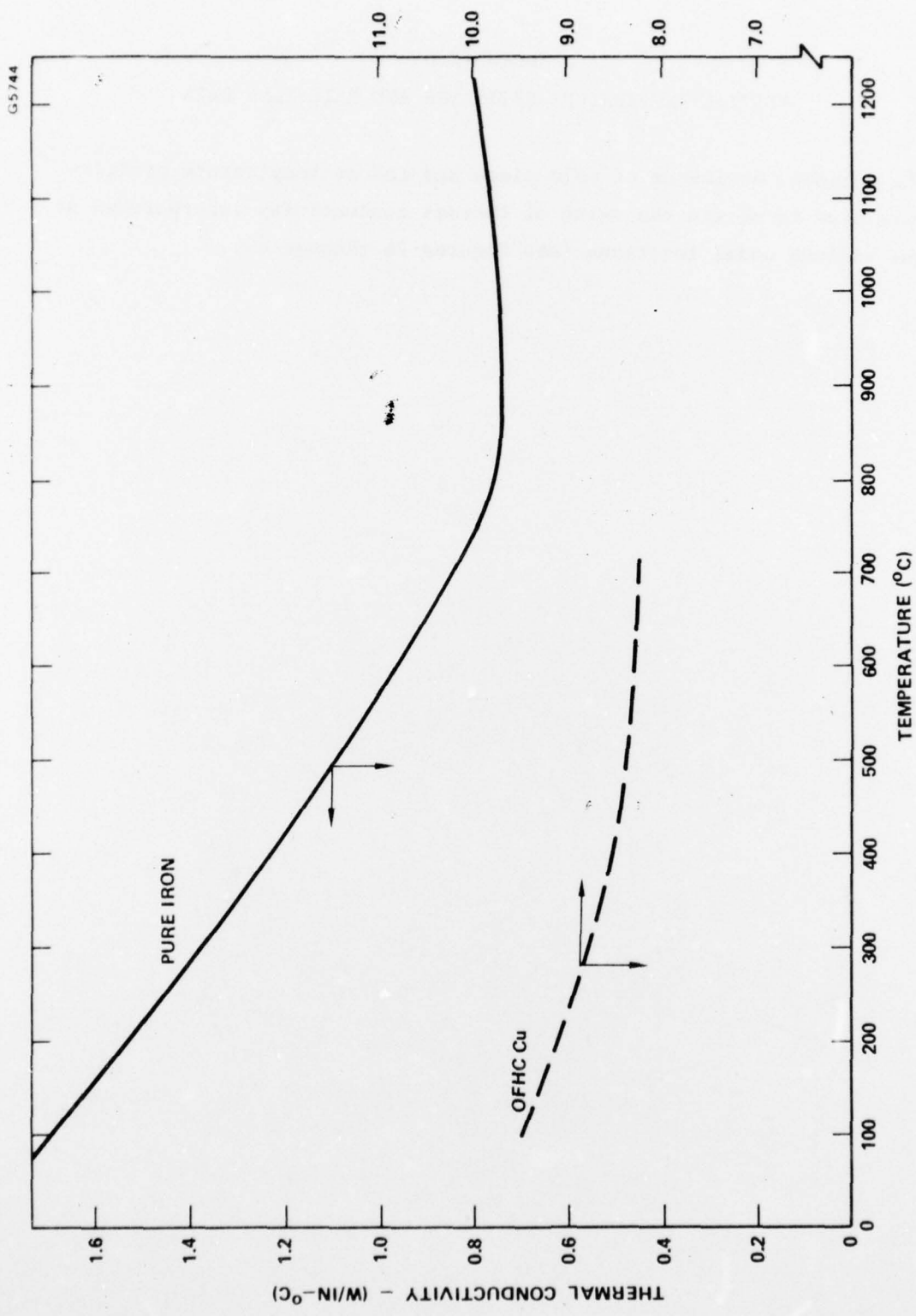


Figure 76 Thermal conductivity vs temperature.

G5745

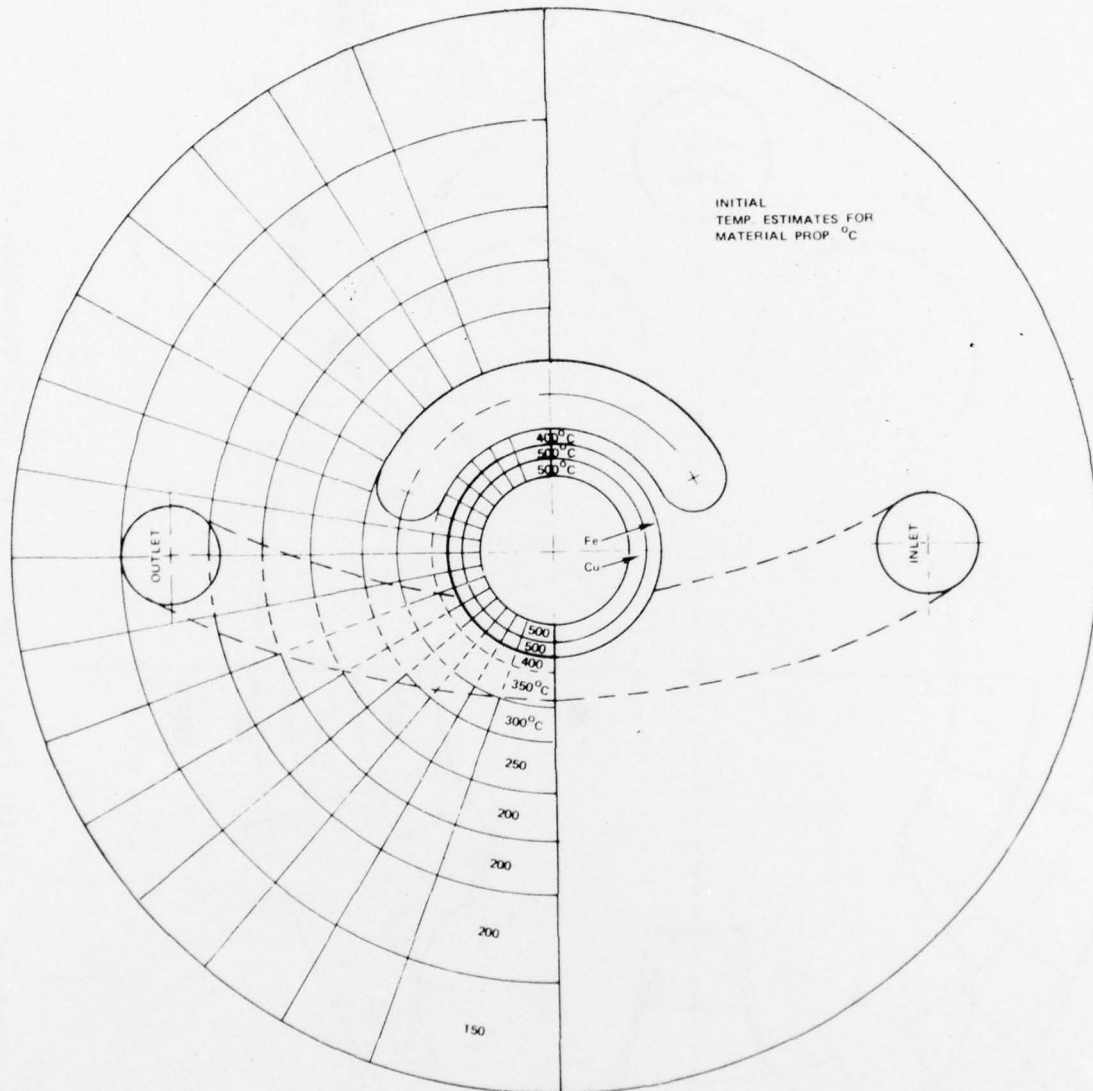


Figure 77 Initial temperature estimates for determining thermal conductances between nodes.

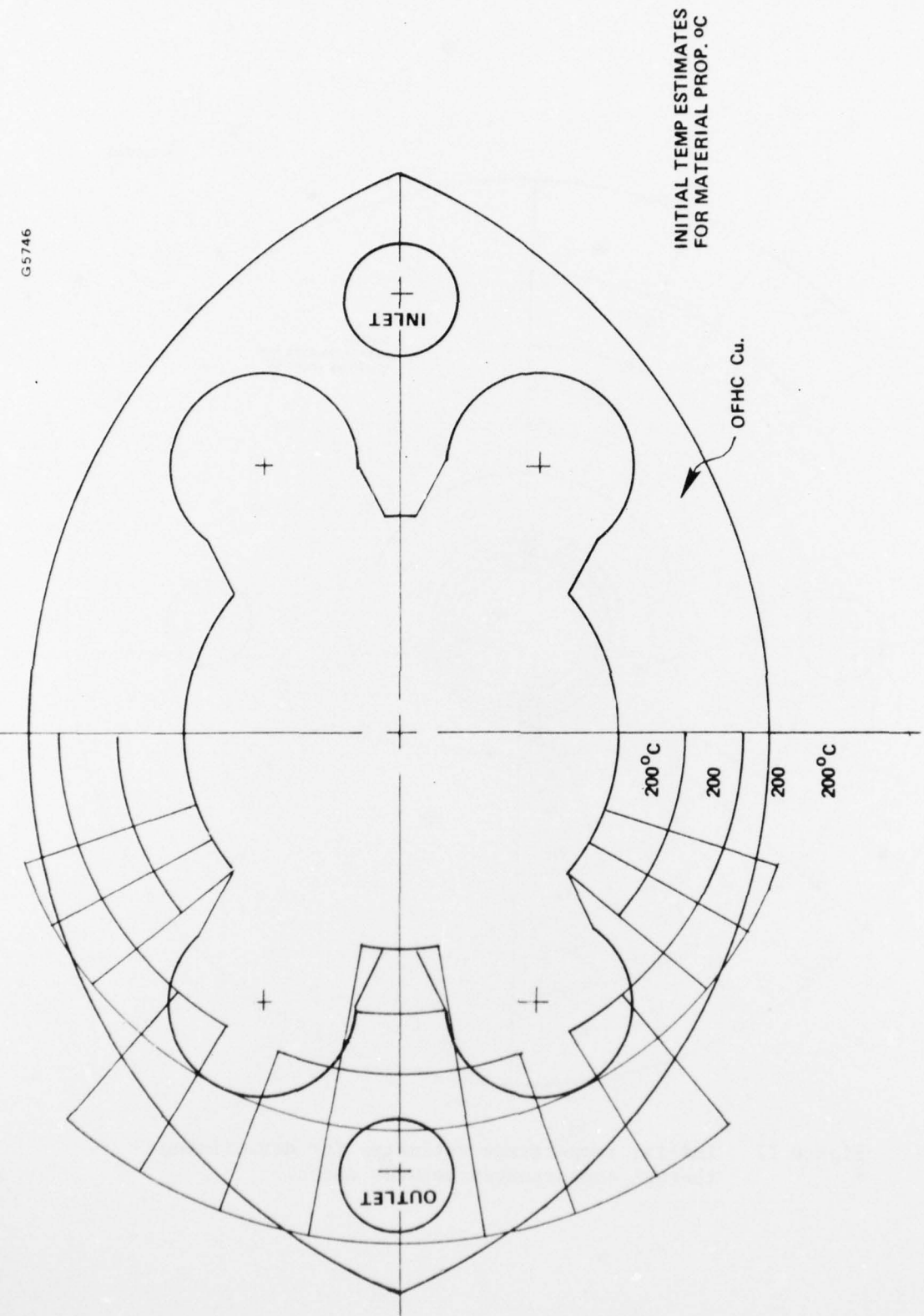


Figure 78 Initial temperature estimates for determining thermal conductance between nodes.

G5747

INITIAL  
TEMP ESTIMATES FOR  
MATL PROP °C

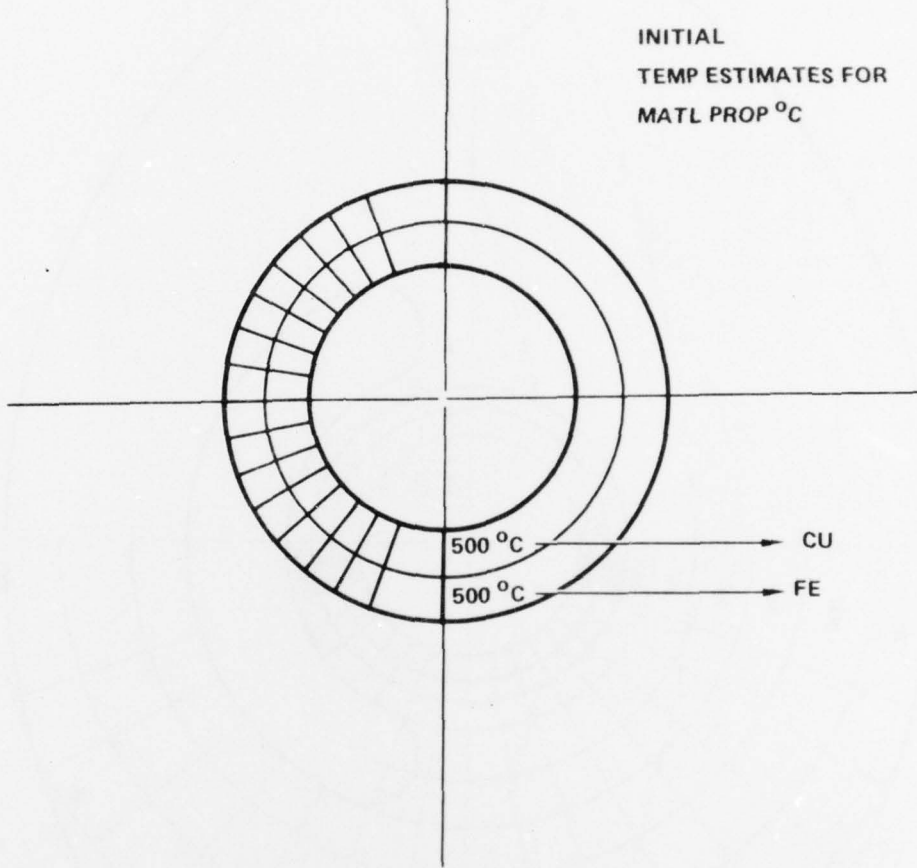


Figure 79 Initial temperature estimates for determining thermal conductance between nodes.

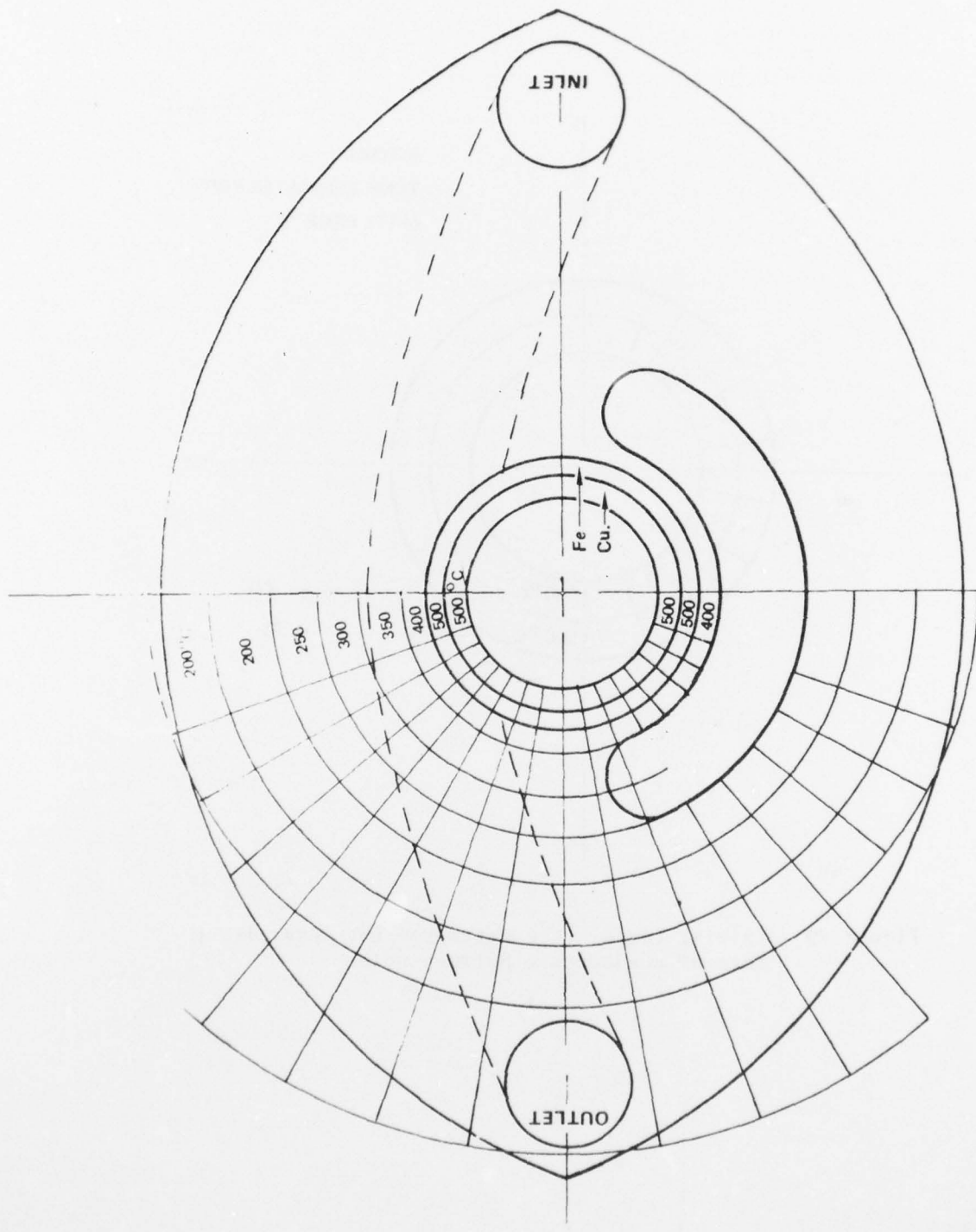


Figure 80 Initial temperature estimates for determining thermal conductances between nodes.

REFERENCES

1. L. Brillouin, "A Theorem of Larmor and Its Importance for Electrons in Magnetic Fields," Phys. Rev., v. 67, pp 260-266, Apr 1945.
2. K. J. Harker, "Periodic Focusing of Beams from Partially Shielded Cathodes," IRE Trans., v. ED-2, pp 13-19, Oct 1955.
3. J. E. Sterrett and H. Heffner, "The Design of Periodic Magnetic Focusing Structures," Trans. on Elec. Dev., v. ED-5, p. 35, Jan 1958.
4. J. T. Mendell, C. F. Quate, and W. H. Yocum, "Electron Beam Focusing with Periodic Permanent Magnetic Fields," Proc. IRE, v. 42, pp 800-80, May 1954.
5. J. T. Mendel, "Magnetic Focusing of Electron Beams," Proc. IRE, v. 43 pp 327-331, March 1955.
6. A. M. Clogston and H. Heffner, "Focusing of an Electron Beam by Periodic Fields," J.A.P., v. 25, No. 4, pp 436-447, April 1954.
7. P. T. Kirstein, G. S. Kino, W. E. Waters, "Space Charge Flow", McGraw Hill, 1967.
8. Seban, R.A., and McLaughlin, E.F., "Heat Transfer in Tube Coils with Laminar and Turbulent Flow", International Journal of Heat Mass Transfer, Volume 6, 387-395, Pergamon Press (1963).
9. Ito, H., "Friction Factors for Turbulent Flow in Curved Pipes", ASME Journal of Basic Engineering, Series D, Volume 81, 123-134, (1959).
10. Irvine, T.F., Jr., "Noncircular Duct Convective Heat Transfer", Modern Developments in Heat Transfer, W. Ibele, ed., Academic Press, N.Y., (1963).

11. McAdams, W.H., Heat Transmission, Third Edition, McGraw-Hill Book Company, Inc., (1954)
12. White, C.M., "Streamline Flow Through Curved Pipes", Proc. Roy. Society., A. 123, 645-663 (1929).
13. Knudsen, J.G. and Katz, D.L., Fluid Dynamics and Heat Transfer, McGraw-Hill Book Co., Inc., (1958).
14. Deissler, R.G., and M.F. Taylor, "Analysis of Turbulent Flow and Heat Transfer in Noncircular Passages", NACA Report TN-4384 (1958).
15. Montgomery, S.R. & Weiss, H.K., "Forced Convection Heat Transfer in Ducts of Noncircular Cross-Section", NEL Report No. 1, (June 1961).
16. Levy, S., R.A. Fuller, and R.O. Niemi, "Heat Transfer to Water in Thin Rectangular Channels", Trans. ASME, J. Heat Transfer, 129-143, (May 1959).
17. Trebes, D.M., J.R. McCarthy, and W.S. Miller, Rocketdyne Memo RM 955-362, 4 September 1963.
18. McCarthy, J.M., "Third Quarterly Progress Report for Product Engineering", Rocketdyne Memo HTUM 64-51, 6 October 1964.
19. Kreith, F., "The Influence of Curvature on Heat Transfer to Incompressible Fluids", Trans, ASME, 1247-1256, (November 1955).
20. Sparrow, E.M., T.M. Hallman, and R. Siegel, "Turbulent Heat Transfer in the Thermal Entrance Region of a Pipe with Uniform Heat Flux", Appl. Sci. Res., Section A, 7, 37-52, (1957).

21 Dipprey, D.F. and R.H. Sabersky, "Heat and Momentum Transfer in Smooth and Round Tubes at Various Prandtl Numbers", Int. J. Heat Mass Transfer, 6, 329-353, (1963).

MISSION  
of  
*Rome Air Development Center*

RADC plans and conducts research, exploratory and advanced development programs in command, control, and communications ( $C^3$ ) activities, and in the  $C^3$  areas of information sciences and intelligence. The principal technical mission areas are communications, electromagnetic guidance and control, surveillance of ground and aerospace objects, intelligence data collection and handling, information system technology, ionospheric propagation, solid state sciences, microwave physics and electronic reliability, maintainability and compatibility.

